CHARACTERIZATION AND VISUALIZATION OF TWO-PHASE FLOW PPROPERTIES OF DIFFUSION GAS LAYERS USED IN

A PEM FUEL CELL

By

Yan Gao

Submitted to the graduate degree program in Chemical and Petroleum engineering and the Graduate Faculty of the University of Kansas in partial fulfillment of the requirements for the degree of Master of Science.

_____

Cairperson Dr. Trung Van Nguyen

_____

Dr. Jenn-Tai Liang

_____

Dr. Jyunsyung Tsau

Date Defended: April 13, 2011

The Thesis Committee for Yan Gao

certifies that this is the approved version of the following thesis:

CHARACTERIZATION AND VISUALIZATION OF TWO-PHASE FLOW PPROPERTIES OF DIFFUSION GAS LAYERS USED IN

A PEM FUEL CELL

_____

Chairperson Dr. Trung Van Nguyen

_____

Dr. Jenn-Tai Liang

_____

Dr. Jyunsyung Tsau

Date approved: April 13, 2011

ABSTRACT

Due to the low-temperature operation of Polymer Electrolyte Membrane fuel cell (PEMFC), liquid water can build up in either flow channels or gas diffusion layers (GDL). Better understanding of the effect of two-phase transport properties on liquid water transport in these porous media is crucial for PEMFC performance improvement. Capillary curves representing two-phase flow properties of porous media are not readily available for the porous media used in a PEMFC because of the minute length scales and complex materials, and no clear relationship between the GDL properties and transport characteristics has been established. This thesis work was designed to address these issues. Volume displacement method was applied to measure the relationships between the capillary pressure and liquid water saturation for two commercial gas diffusion materials, Toray TGP-H-090 and Toray TGP-H-060. The impact of channel-rib structure on capillary properties of GDLs was investigated by two different configurations with different rib-channel designs. The saturation level was found to decrease as the rib-to-channel width ratio increased since less area of the GDL was available for liquid water penetration into the GDL. The effects of perfluorotetrafluoroethylene (PTFE) loadings and compression were also studied. PTFE addition to the GDL above 20wt% had little effect on the capillary curves because the fluoropolymer was not uniformly distributed on the carbon surface but

thickened the existing coat of PTFE. Inhomogeneous compression distributions caused by rib/channel designs created different local physical properties. Furthermore, the capillary pressure properties in GDL were affected by unevenly distributed compression. Consequently, capillary pressure curves using average liquid saturation level and capillary pressure may not accurately describe the transport properties in porous media. Neutron imaging was used to study water distribution in both in-plane and through-plane directions in a GDL. It was shown that the liquid water saturation level in the GDL above the ribs was less than that above the channels, illustrating the role of the flow field elements on the local water distribution in the GDL. The difference in the liquid saturation level proved that higher compression level of the GDL above the ribs led to different morphological properties and, consequently, transport properties. Once liquid water breakthrough was reached, water was observed to flow through a single pathway. These results demonstrated that the assumption of isotropic transport properties of the GDLs in PEM fuel cell models needed to be reconsidered.

ACKNOWLEDGEMENT

I would like to thank my advisor Dr. Trung Van Nguyen for instilling in me the qualities of being a good researcher. Dr. Nguyen has patiently guided and assisted my research, showed me practical issues beyond the textbooks. His enthusiasm and professional ethics have been major driving forces through my graduate study at University of Kansas and will continually inspire me throughout my life.

I would like to thank my committee members Dr. Jenn-Tai Liang and Dr. Jyunsyung Tsau for their advice and patience in reviewing my dissertation. I would like to take this opportunity to thank Dr. Daniel S. Hussey at National Institute of Standard Technology where I worked for a very short duration. I appreciate his help and valuable suggestions for my work on neutron image analysis.

I would like to thank Dr. Xuhai Wang for his helpful discussion throughout my research work in capillary pressure measurements. Thanks also go out to my colleagues, Dr. Berker Facicilar and Venkata Yarlagadda for their help in my experiments.

I would also like to thank my family and friends. They were always supporting me and encouraging me with their best wishes. Finally, I would like to thank my boyfriend, Geng Wang who was always there cheering me up and stood by me through my graduate studies.

TABLE OF CONTENTS

LIST OF FIGURES

LIST OF TABLES

NOMENCLATURE

N_w	Capillary diffusion rate of liquid water, mol/cm^2· s
P_w	Capillary pressure, Pa
K_w	Liquid relative permeability, cm^2
μ_w	Viscosity,g/m· s
ρ_w	Density, g/cm^3
M_w	Molecular weight, g/mol
σ	Surface tension of the liquid water-air interface, N/cm^2
θ	Contact angle of the liquid-air interface
r	Pore radius, cm
ε_0	Porosity of a GDL without PTFE coating
ρ_G	Bulk density of the matrix, g/cm^3
χ	PTFE content, %
ρ_t	Density of Teflon, g/cm^3
P_g	Atmospheric pressure, Pa
P_l	Liquid water pressure, Pa
t_{uncomp}	Thickness of uncompressed GDL sample, cm
t_{comp}	Thickness of compressed GDL sample, cm
$V_{comp.void}$	Void volume of compressed GDL sample, cm^3

V_{total}	Total volume of GDL sample, cm^3
V_{dis}	Displaced water volume, cm^3
ε	Porosity of uncompressed GDL sample
ε'	Porosity of compressed GDL sample
I_{final}	Intensity of attenuated neutron beams through aluminum plates, neutrons/cm^2·s
I_0	Intensity of beam of neutron beams, neutrons/cm^2·s
t_{Al}	Thickness of aluminum plate, cm
t_{water}	Thickness of liquid water contained in porous media, cm
C	Amplified light coefficient emitted by the image intensifier
G_{offset}	Gray level offset value resulting from charge build-up in the CCD
G	Gray level of an attenuated neutron image

CHAPTER 1

Introduction

1.1 Polymer Electrolyte Membrane Fuel Cell History

The first simple H_2-O_2 fuel cell, using sulfuric acid as electrolyte, was invented to produce electricity by William Grove in 1839 [1]. In 1932, Francis Bacon successfully developed the first hydrogen fuel cell. An alkaline electrolyte and nickel electrodes were applied in his experiment. The National Aeronautics and Space Administration (NASA) has tried finding compatible fuel cells for space missions since late 1950's. These programs boosted the development of fuel cell technology. Alkaline fuel cells successfully provided electrical power in Apollo space program which landed humans on the moon. Proton exchange membrane (PEM) fuel cell technology was first invented by General Electric in the early 1960s, "a research program with the U.S. Navy's Bureau of Ships (Electronics Division) and the U.S. Army Signal Corps"[2]. Although the cell had high portability, it was still too expensive to produce. Since then, polymer electrolyte fuel cells have proved their capability in Gemini spacecraft and consective space vehicle programs. In the early 1990s, a Ballard Mark 5 PEM fuel cell stack was developed with 5 kW total power [2].

With the depletion of traditional fossil fuels and environmental problems, hydrogen energy has been considered as the most viable substitute. The PEM fuel cell,

as a hydrogen energy converter, demonstrates its capability of zero emission and high efficiency in power systems, especially for automobile applications[2].

1.2 PEM Fuel Cell Principles

Fuel Cell's principle is based on the chemical reaction from fuel and oxidizer, and the energy efficiency of a fuel cell system is over 40%. While the conversion efficiency for an internal combustion engine may only achieve 26%. [3]

Figure 1.1 shows the basic components and operation of a PEM fuel cell. A proton conducting membrane separates the anode and the cathode side, and each side consists of a flow field, gas diffusion layer and catalyst layer. The flow field acts as a fuel distributor and a current collector to transport electrons.

There are two major electrochemical reactions in the fuel cell:

$$H_2 \leftrightarrow 2H^+ + 2e^-$$

$$\frac{1}{2}O_2 + 2H^+ + 2e^- \leftrightarrow H_2O$$

On the anode side, hydrogen flows into gas flow field, and then diffuses from the gas diffusion layer (GDL) to the anode catalyst layer (CL) where it dissociates into protons and electrons. The protons are conducted through the membrane to the cathode with water by electro-osmosis, and the electrons provide electrical energy in an external circuit. On the cathode side, oxygen molecules transported from GDL to CL react with the electrons and protons to form water. In the process, water, heat and

electrical energy are produced.

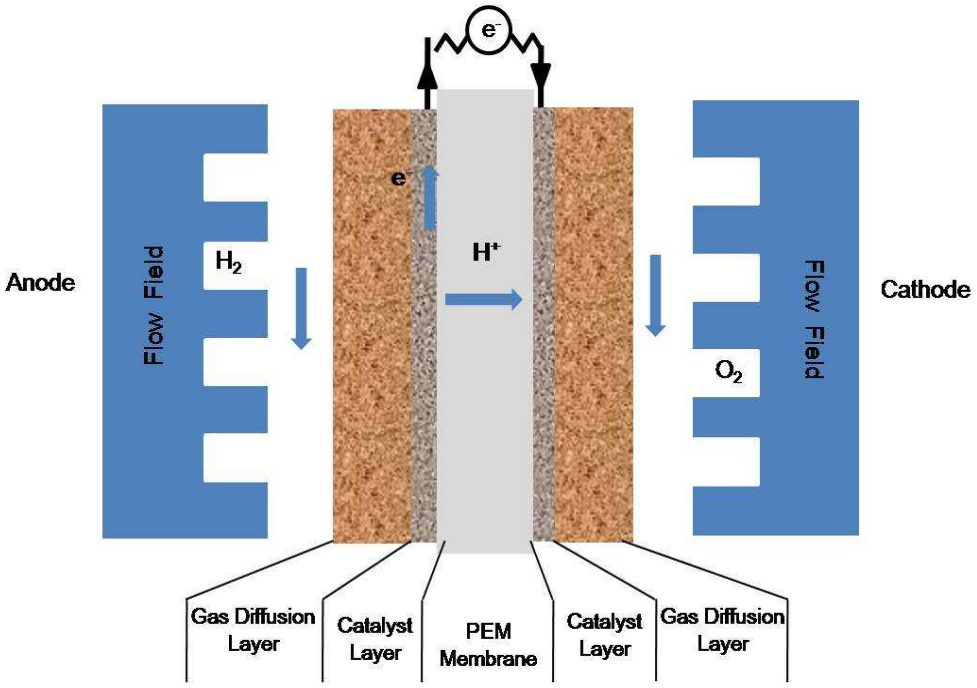

Figure 1.1 Schematic picture of components and operation in a PEM fuel cell

1.3 Fuel Cell Performance

A typical polarization curve, showing the voltage versus current density, gives detailed information of the fuel cell performance. The *i-V* curve for a PEM fuel cell is described in Figure 1.2.

Under an ideal thermodynamic equilibrium condition, the voltage of a fuel cell keeps constant with the increase of current. This can be achieved in an open circuit system. In practice, however, due to unavoidable losses, the cell voltage decreases as the current is drawn from a fuel cell. Each loss is associated with fuel cell operation steps: activation losses due to electrochemical reaction, ohmic losses due to ionic and

electronic conduction, and concentration losses due to mass transport. Among which, poor mass transport leads to significant fuel cell performance loss since the electrochemical reaction occurring in the catalyst layer is affected adversely by liquid water accumulation in the porous electrode. Therefore, in order to improve the performance of the fuel cell, we need to learn how liquid water moves around in the fuel cells.

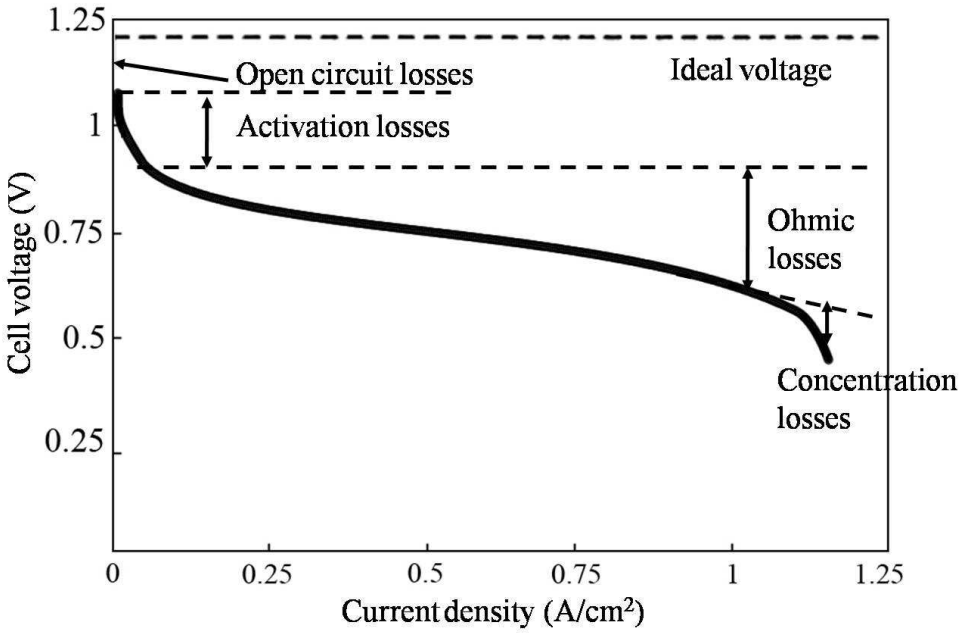

Figure 1.2 Schematic of fuel cell i-V curve

1.4 Fuel Cell Water Management

1.4.1 Water Movements

From Figure 1.3, we can see that water is either brought into the fuel cell by humidified gas streams, or generated from oxygen reduction reaction (ORR) at the

cathode catalyst–membrane interface [4]. Through the proton exchange membrane, water molecule is dragged with protons by electro-osmosis from anode to cathode side, whereas the back-diffusion transport, caused by the concentration gradient across the membrane, drives the water to move back towards anode.

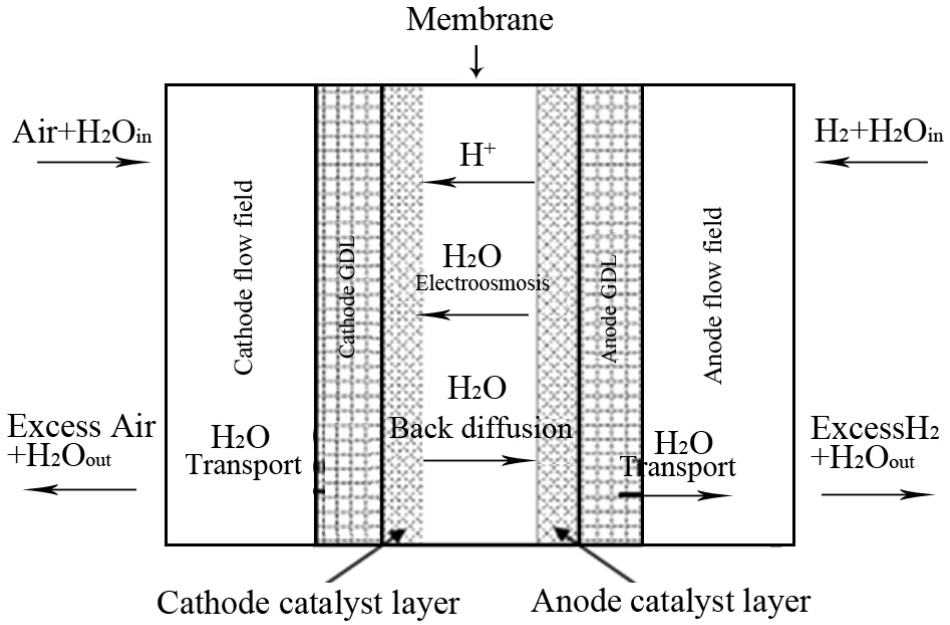

Figure 1.3 Water movements in a PEM fuel cell [5] (Reprint from Ref. [5], copyright 2008, with permission from Elsevier)

1.4.2 Water Management

Water balance has been a big issue in PEM fuel cell performance. High moisture in the proton-conducting membrane is desired to maintain its ionic conductivity. When the water removal rate exceeds the water generation rate, it leads to membrane dryout and can result in accelerated degradation in the ohmic polarization region.

Moreover, the product-liquid water is generated as a by-product on the cathode side. It must pass through the GDL from catalyst layer to the flow channel by evaporation, diffusion and capillary transport. If the water generation rate exceeds the removal rate, the liquid water accumulates in both gas diffusion layer and catalyst layer. The excessive water may block the reactive sites for the reactants and pathway for products to move out of the porous electrodes, resulting in water flooding.

Water flooding can occur in discrete regions in fuel cells, such as anode or cathode catalyst layers, gas diffusion layers, or flow channels, as seen in Figure 1.4 [6]. At low current densities in Figure 1.4 (b), due to low gas-phase velocity, slug formation is observed in anode and cathode side-channel and blocks pathway for the gas phase transport in the channels. At higher current densities, the gas-phase velocity is sufficient to remove the slugs, flooding is more likely to happen in the catalyst layer or gas diffusion layer on the cathode side, as seen in Figure 1.4 (c) and (d) [6].

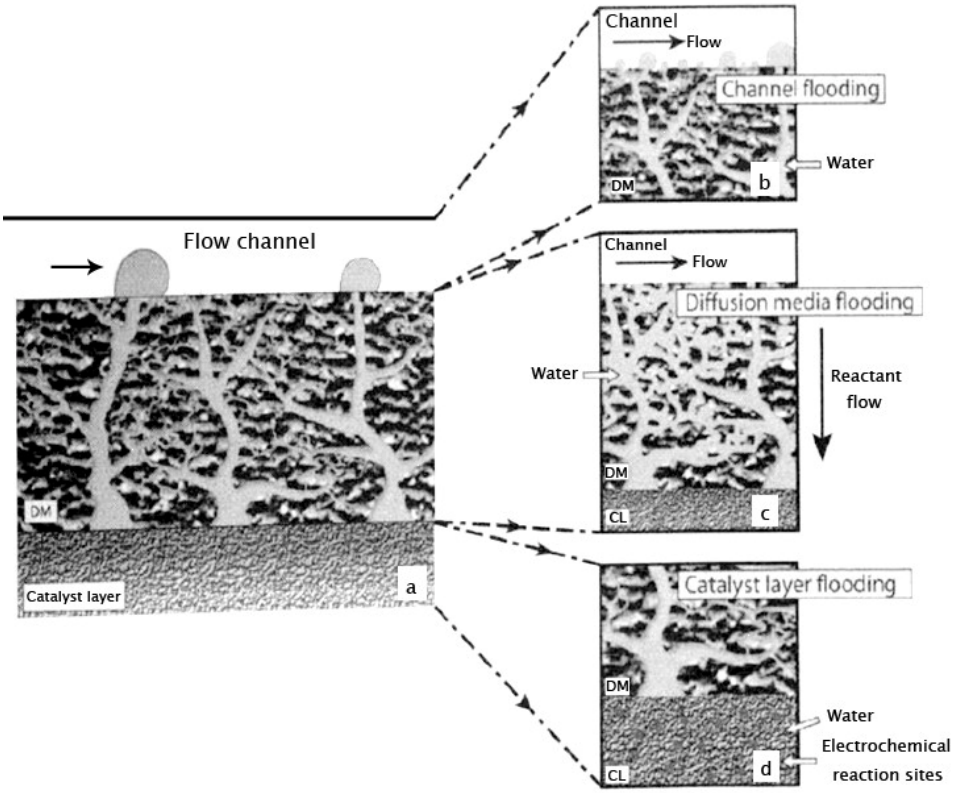

Figure 1.4 Different locations of water flooding in PEM fuel cell [6] (Copyright Wiley-VCH Verlag GmbH & Co. KGaA. Reproduced from Ref [6] with permission)

Water flooding is a result of complex interaction between configuration design, material properties and operating conditions. Figure 1.5 compares the polarization curves with and without flooding. The performance curves separate from each other in concentration overpotential region at different water flooding levels. And the performance loss is greater as the water flooding becomes severe. This is attributed to flooding blockage on the active area and film resistance caused by slug formation [6].

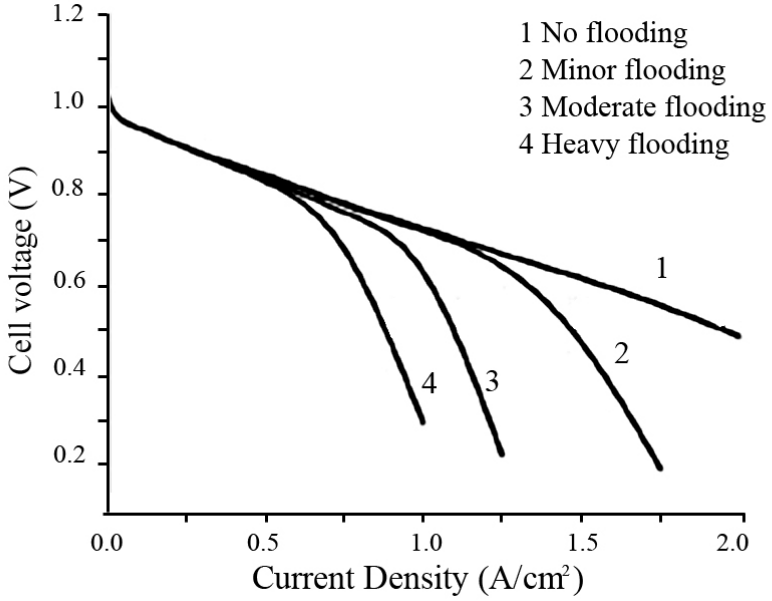

Figure 1.5 Polarization curves of PEM fuel cell with increasing water flooding [5]
(Reprint from Ref. [5], copyright 2008, with permission from Elsevier)

1.5 Role of Gas Diffusion Layer in Water Management

A gas diffusion layer (GDL) consists of carbon fiber or carbon woven materials, as shown in Figure 1.6. The GDL serves multiple functions in a PEM fuel cell. It provides electronic conduction between the catalyst layer and bipolar plate; it provides access for the reactant and product between the flow distribution plate and the catalyst layer; it transfers heat from catalyst layer to the bipolar plate; it is also used as a mechanical support for membrane structure to avoid intrusion into the channels.

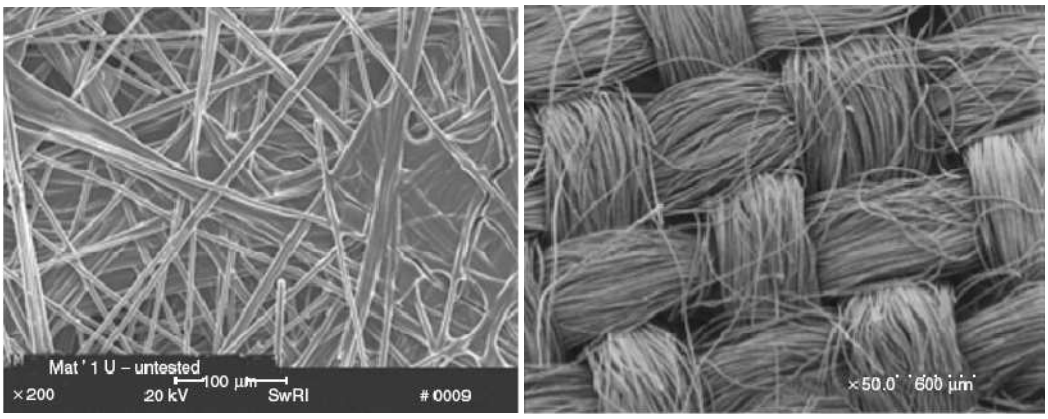

(a) Carbon fiber paper (b)Carbon cloth

Figure 1.6 SEM images of the substrates of gas diffusion media [7] (Copyright Wiley-VCH Verlag GmbH & Co. KGaA. Reproduced from Ref [7] with permission)

Furthermore, the GDL plays an important role in water management. Water management is strongly influenced by interdependent properties of the GDL, such as, wetability (contact angle), wetproof, and pore size distribution. Hydrophobic content is loaded to relieve water retention in the GDL and makes the GDL mixed hydrophilic-hydrophobic structure. The mixed property allows both liquid and gas to pass. These properties of GDLs must be balanced carefully to prevent water flooding but maintain hydration of the membrane.

1.6 Objective and Motives

Liquid water transport in the GDL is dominated by capillary force, Darcy's law is used to describe the liquid water flow in porous media [8],

$$N_w = -\frac{\rho_w K_w}{M_w \mu_w}(-\nabla P_c) \quad (1.1)$$

The capillary diffusion rate of liquid water N_w is a function of ∇P_c, the liquid relative permeability (K_w) and viscosity (μ_w).

Various empirical expressions have been developed by researchers to correlate the capillary pressure with liquid water saturation level, the most widely used approach is the polynomial fitted correlation obtained by Udell [9], which was based on the experimental data of water wetting in a range of unconsolidated soil with uniform wettability [10]. However, this traditional Leverett approach cannot accurately describe the flow through these heterogeneous porous media since heterogeneous property has not been previously considered in soil science. Additionally, the effects of assembly compression, hydrophobic loading on the capillary transport characteristics need to be considered in the measurements. Therefore, relationships representing typical multiphase transport in these porous materials are desired to improve the water management and provide the guidance for fuel cell materials engineering.

The aim of this work was to apply the volume displacement method to measure the relationship between the capillary pressure and liquid water saturation of commercially available gas diffusion materials, and to investigate the effect of wetproof level and compression on the capillary properties of GDLs and enable the designers to optimize the design of flow fields and the properties of GDLs. The neutron imaging method was used to study the water distribution patterns inside a

GDL under nonuniform compression and provide insight for future modeling studies of liquid water transport in PEM fuel cells.

CHAPTER 2

Literature review

Characterization of the liquid water distribution pattern and modeling the effect of liquid water on the fuel cell performance are pivotal to the development of fuel cell. Characterization and modeling studies help us better understand how the transport properties in a gas diffusion layer affect the fuel cell performance and improve the efficiency of fuel cell.

The exact liquid water distribution pattern in the GDL cannot be precisely measured. According to the capillary theory, it is believed that the pathways through which liquid water and gas phase flow are different. Large hydrophobic pores and all the hydrophilic pores provide the routes for liquid water, while the gas phase flows through small hydrophobic pores [6]. Since most GDLs are coated with anisotropic hydrophobic material (PTFE), such coatings yield a complex bimodal (hydrophobic and hydrophilic) pore size distribution. A water droplet shape on two GDL surfaces with different wettability is shown in Figure 2.1. [6]

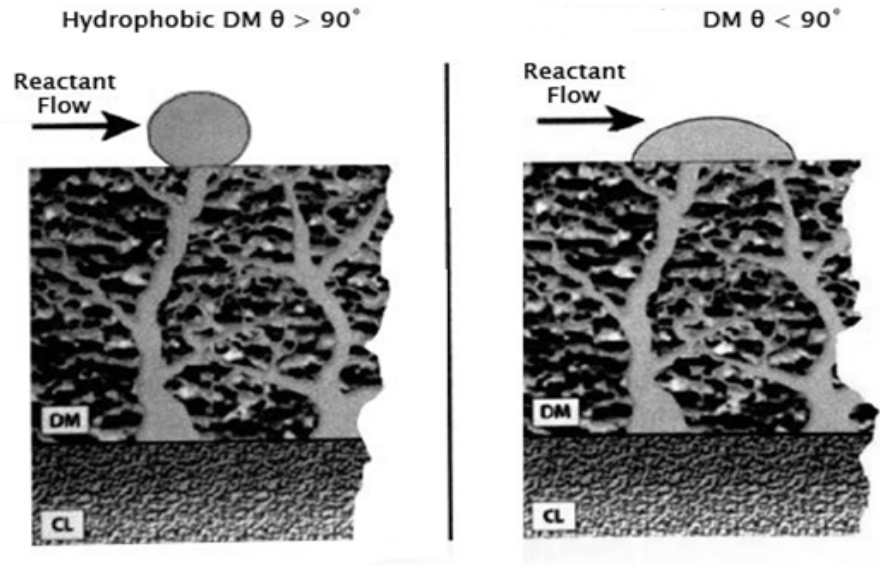

Figure 2.1 Liquid water droplets on hydrophobic and hydrophilic GDL surfaces [6] (Copyright Wiley-VCH Verlag GmbH & Co. KGaA. Reproduced from Ref [6] with permission)

With heterogeneous wetting properties, some regions in the GDL are affinitive to liquid, while other regions will force water away, as shown in Figure 2.2 [11]. Such heterogeneity of structure causes the complex two-phase flow in the gas diffusion layer. Therefore, it is difficult to develop a fundamental and clear knowledge of the transport processes of liquid water through the GDL. Capillary pressure curves, as a reflection of capillary properties of the GDL, help with the understanding of transport properties of liquid water in the GDL.

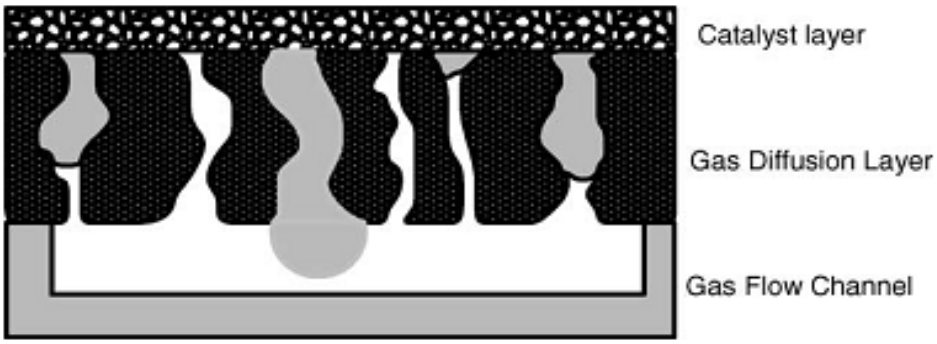

Figure 2.2 Water movements in the gas diffusion layer. Water flows through the large hydrophilic pores. In the smaller hydrophobic pores, no water enters. Water is trapped in pores with mixed wettability, which has radius smaller than the critical radius. [11] (Reprint from Ref. [11], copyright 2005, with permission from Elsevier)

There have been a large number of numerical models that apply equations for multiphase flow in porous media to illustrate the effect of liquid water transport on PEM fuel cell performance. However, the necessary physical parameters and capillary properties used in these equations are usually not known, such as thickness, compression, and pore-space morphology which steer the transport behavior in the gas diffusion layer. Developing methods for testing these properties specifically for the GDLs and their effects on GDL transport properties is necessary.

In this chapter, the knowledge of transport properties in GDL will be reviewed. The discussion will include the role of physical properties of GDL in water transport in PEM fuel cells, capillary pressure curves, and direct visualization of water

distribution in PEM fuel cells.

2.1 GDL Properties

2.1.1 Porosity and PTFE

Porous structure of the GDL provides access for the reactant gases to the catalyst layer and pathway for the product water to evacuate. In water management, the role of PTFE treatment in the GDL is to effectively repel the liquid water and keep the pores for the gaseous reactants to pass through relatively dry.

The three methods used to determine the bulk porosity of GDL are mercury porosimetry, immersion method and method of standard porosimetry (MSP) [12]. Mercury porosimetry is a technique used to characterize the porosity of materials by applying different levels of pressure to the sample immersed in mercury. During the test, the pressure is controlled to introduce the fluid into the pores. For many materials, mercury is nonwetting so that this method can be used to access all the pores in the sample. The increased pressure is related to the increase in the volume of mercury intruded into the sample. The pore size is calculated by this volume of mercury with applied pressure. The pore size distribution of a typical GDL is given in Figure 2.3. It shows meso- and macro-pores with the average diameters of 4.3 and 40.3 μm, respectively [13].

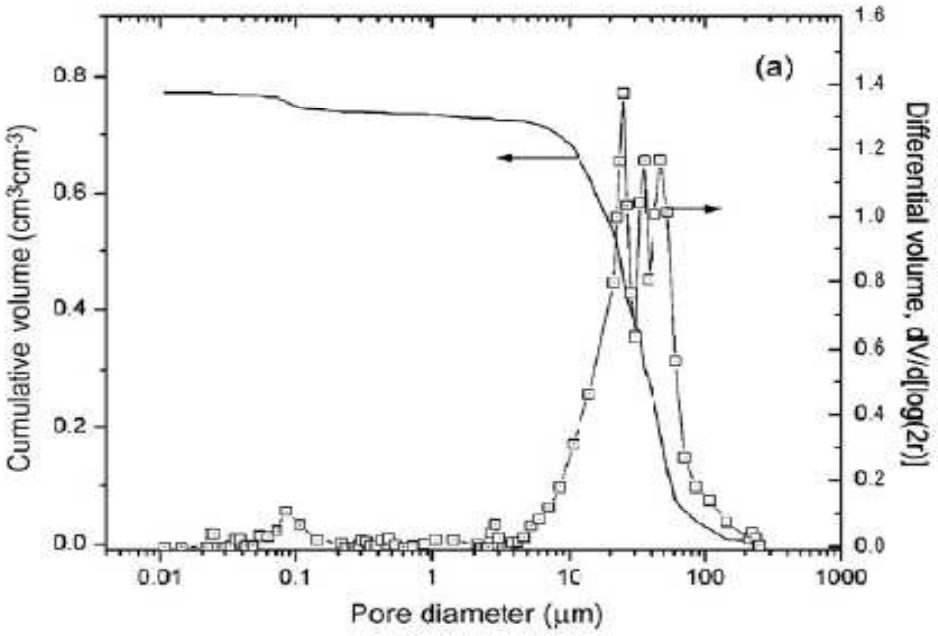

Figure 2.3 Mercury intrusion porosimetry data for Toray TGP-H030 with 20 wt% PTFE [13] (Reprint from Ref. [13], copyright 2008, with permission from Elsevier)

In immersion method, the bulk porosity is determined by weight gain for the sample immersed in a wetting liquid.

Martínez [14] used MSP method, which is developed by Volfkovich et al. [15], to characterize the porosity of materials. When two materials partially saturated are contacted, the system moves toward equilibrium until equal capillary pressure is achieved. The capillary pressure of the test sample is obtained from the volume of liquid in the sample and capillary pressure of the standard sample that is in contact with the testing sample. Each capillary pressure of the test sample corresponds to a definite radius value. Then the pore size distribution is illustrated by cumulative

volume versus radius values [14].

The effects of the porosity distribution of the gas diffusion layer on the transport phenomena have been simulated by Zhan et al. [16]. Based on the assumption of a fixed liquid saturation difference between the interfaces of the catalyst layer/GDL and the GDL/gas channel, the liquid water flux through the GDL increased as the porosity increased. For the GDLs with the equivalent porosity, more liquid water was discharged when the gradient of the porosity distribution between the interfaces became larger.

Chu [17] investigated the influence of the porosity of the GDL on the performance of a PEM fuel cell. In his studies, when the current density was at medium or low values, porosity distribution's change did not take any effect on the polarization level. On the contrary, if the current density reached the limiting value, the polarization level was significantly influenced. This was attributed to the fact that larger porosity in the GDL resulted in a larger oxygen transfer from the gas channel to the catalyst layer and then a larger current density was produced. This result proved that polarization curve in the regime near the limiting current density is controlled by mass transfer in the GDL and the catalyst layer.

The effects of PTFE content on the surface morphology of the GDL and the performance of the PEM fuel cell was studied by Lim and Wang [18]. The study

suggested that hydrophobicity created by 10wt.% PTFE loading in GDL was sufficient to produce gas transport pathway through the GDL. Park et al. [19] indicated that 20% PTFE content in the microporous layer was the optimal amount for effective water management and improved oxygen diffusion kinetics in the membrane-electrode assembly.

2.1.2 Compression

GDL properties, such as its porosity, wettability and thickness, have direct impact on water movement in the fuel cell. When the cell is assembled with compression, some of these parameters change subsequently. For example, compression can reduce the GDL thickness, break fibrous structure and change porous structure in the GDL and eventually influence the performance of the PEM fuel cell.

A number of experimental researches have identified the effect of compression on property changes of a gas diffusion layer and its subsequent effects on the fuel cell performance. Bazylak et al. [20] visualized the ex-situ water movement (preferential pathway of liquid water) through the gas diffusion layer using fluorescence microscopy under various compression. Combined with scanning electron microscope, they related the water movement trend to the observed change of hydrophilic and hydrophobic regions which was caused by the breakage of fibers under various compressions. Chang et al. [21] found the compression pressure changed

the porosity of GDL. The porosity decreased dramatically at small compression pressure values. Beyond that range, the porosity is inversely proportional to the compression force. Furthermore, low compression resulted in a high interfacial resistance between the bipolar plate and the gas diffusion layer and caused a significant loss in the performance of the PEM fuel cell. In contrast, high compression pressure limited the pathway for mass transfer but reduced the contact resistance between graphite carbon and gas diffusion layer. Lee et al. [22] tested effects of compression on the performance of fuel cells by using different types of gas diffusion layers. An optimal compression and GDL material were found in terms of the changes in the porosity and the electrical contact resistance.

Numerous mathematical models were also developed to describe the transport phenomena in the GDL and to predict the cell performance. Nitta et al.[23] reported that the inhomogeneous compression of GDL led to significant local variation of mass transport properties and current density in the GDL. Zhou et al. [24] found that the optimal compression ratio would depend on the combined effects of GDL deformation and porosity change on the ohmic resistance and mass transfer.

2.2 Capillary Pressure Curves

A capillary pressure curve is used as a constitutive relationship between the capillary pressure and saturation. The expression and shape of the curve depend on many

properties, including pore size distribution, porosity, breakthrough pressure, and fluid-solid wettability.

A GDL consists of connected and unevenly distributed pores with different radius sizes. The capillary pressure at the interface for each cylindrical pore is described by the Young-Laplace equation:

$$P_c = -\frac{\sigma \cos\theta}{r} \tag{2.1}$$

Where σ is the surface tension of the liquid water-air interface, θ is the contact angle of the liquid-air interface on the porous surface, and r is the effective pore radius.

A range of pressures scanned and the cumulative volume of non-wetting phase injected at each pressure compose one part of a capillary curve. When pressure is reduced in a similar rate, the non-wetting phase begins to withdraw from the sample and another part of the curve is obtained.

Since multiphase flow through mixed hydrophobic/hydrophilic pores in GDL is not well developed, much of the present understanding is based on porous media theory from soil and petroleum engineering studies and several empirical and semiempirical expressions, such as the Leverett's approach, are used to describe the capillary transport behavior of GDLs. However, there are a few differences between the porous media used in PEM fuel cells and that in soil science. Hydrophilic media are widely used in soil science studies, whereas the GDL in PEM fuel cells have a

highly heterogeneous surface. The soil science work deals with the materials in saturated situation, but the work in fuel cell is done with materials partially saturated [6]. The characteristic behavior of the porous media is different from that in soil science. It is the properties of individual GDL that determine the transport behavior. Due to these differences, several researchers realized inaccuracy of Leverett's modeling and have attempted to find alternative methods [25-28].

Mercury intrusion porosimetry (MIP) has been widely applied for measuring capillary pressure curves. There are several disadvantages of MIP, though it's been well established. First, the contact angles of mercury and water on the GDL surfaces need to be known for converting the mercury intrusion pressure to the air-water pressure. It is unrealistic to use a single contact angle for mercury in the GDL since the contact angle for water is not unique and varies on the graphite and PTFE surfaces. Therefore, it is impossible to obtain precise conversion without specific information of PTFE distribution. Furthermore, the Young-Laplace equation required in this conversion is only adapted to cylindrical pores and is not necessarily valid for fibrous GDLs with amorphous pores [27].

The method of standard porosimetry (MSP) [15] is another approach to measure air-water capillary pressure curves and it is originated from Gostick [27]. The limitation of this method is that the experiment has to start with a fully saturated sample and

only drainage curve can be obtained and it can only scan for $P_C < 0$. Gostick et al. compared the result from MIP with that from MSP on capillary curves for hydrophilic pore network. The total porosity distribution obtained with MSP was compared favorably with the MIP technique. The shapes of hydrophilic capillary curves were similar to the overall capillary curves for different GDL materials. Kumbur and his co-workers [28] have used MSP technique to study a wide variety of GDLs coated with MPL and with different PTFE contents, under different compressions. They have further attempted to synthesize a single relationship that could describe the capillary properties of any GDL, with any combination of the above parameters (compression, hydrophobic polymer loading), to replace the traditional Leverett approach.

Gallagher et al. [29] applied water transport plate technology, which was similar to MSP. The GDL sample, which was initially saturated, was placed on top of hydrophilic porous plate with channels. A separate porous plate without channels covered the GDL to prevent evaporation. The capillary pressure of the bottom porous plate was controlled by the pump on the flow line circulating the water between the bottom plate and water reservoir. The water might flow in or out of the GDL whenever the capillary pressure in the GDL was different from that in the porous plate. This method was also limited to $P_C < 0$. The hysteresis between imbibition and

drainage curves was observed and was assumed to be caused by the difference between the advancing and receding angles.

Microfluidic method [26, 30] or porosimetry [25] is a method that adapting MIP concept and using liquid water as the fluid to measure capillary pressure. In such apparatus, a porous hydrophobic membrane is used as a barrier to prevent liquid water from breaking though the top of the sample. A porous hydrophilic membrane between the GDL and liquid water reservoir prevents air from entering the sample during water drainage. Fairweather et al. [30] applied intermittent liquid/gas intrusion to ensure that the complete equilibration was reached during the whole cycles. In their recent work [31], Cheung used a bundle of capillaries model (to interpret the MIP data for pore size distribution), combined with Gaussian contact angle distribution, to compute a realistic capillary pressure curve and revealed that the observed hysteresis in the capillary curves came from different internal surface wetting properties between imbibition and drainage. Such extensive capillary pressure hysteresis was confirmed by the measurements of Harkness et al. [25]. In the following work, based on a bundle of capillaries model, Fairweather et al. [32] reported that effective mean contact angles increased with the initial addition of Teflon, however, no further wetting properties changed when the Teflon loading level was above 5 wt.%.

The volume displacement technique, proposed by Nguyen [33], controls the liquid

pressure instead of the liquid volume. Capillary pressure is controlled by adjusting the hydrostatic pressure of the liquid phase. As the static pressure is altered, the liquid saturation in the GDL can be calculated from the volume change of liquid water in the horizontal tube with known diameter. The capillary pressure data obtained from this technique have been incorporated into continuum fuel cell models.

Figure 2.4 presents the air-water capillary curves obtained using each of the above methods. Fairwheather et al. [31] used Toray TGP-H-090 to show a complete capillary curve including imbibition and drainage. Similar materials Toray TGP-H-060 with different PTFE content were used by other researchers. Gallagher et al. [30] measured the capillary curve of Toray TGP-H-060 limited to $P_c<0$. Both Gostick [28] and Harness [26] scanned the entire range of capillary curves for Toray TGP-H 060. The capillary pressure measured by Nguyen et al. [34] was below breakthrough point of Toray TGP-H-060 and no hysteresis was observed in this capillary curve. This method can be also used to evaluate the capillary pressure beyond breakthrough point.

An ideal method is one that should be pressure controlled since it is difficult to interpret data from volume-controlled experiments. Additionally, the ability to scan the entire range of capillary pressures in both directions is essential for capillary pressure measurement. The volume displacement method, which satisfies these

requirements, will be used in our experiments. This will be described in detail in the experimental section (Section 3.2.3).

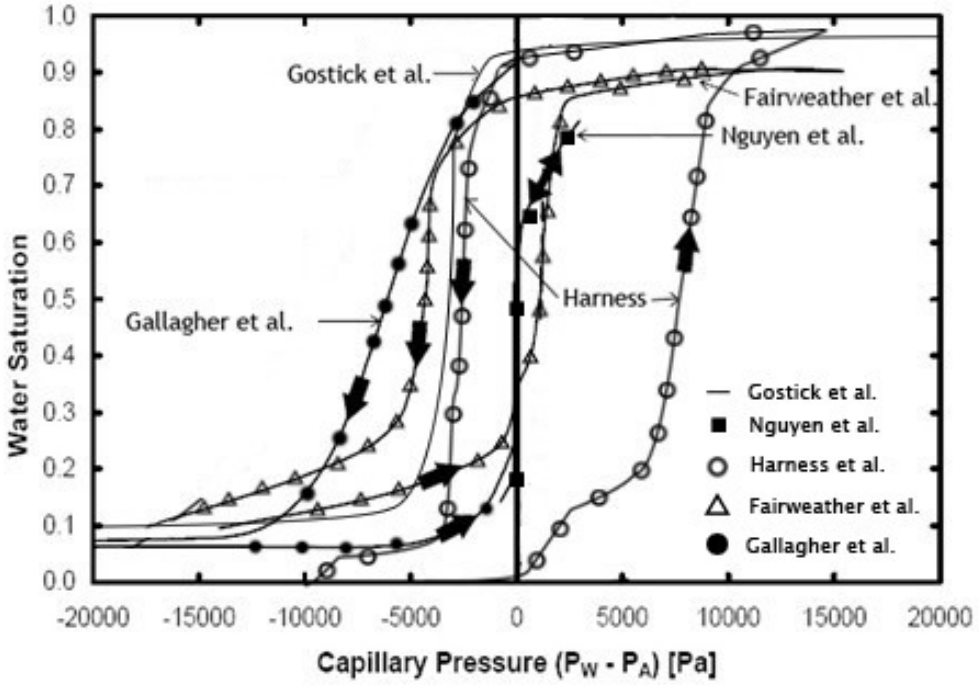

Figure 2.4 Capillary pressure curves for Toray 060 and Toray 090, all curves are for Toray TGP-H-060, except Fairweather et al. (Toray TGP-H-090 with no PTFE). Toray 060 with 20 wt% wetproof in the experiment of Gostick et al, 10 wt% wetproof in the experiment of Harness et al. and Nguyen et al.

2.3 Imaging Techniques for PEM Fuel Cells

Besides the measurement of capillary properties, imaging techniques have been taken as diagnostic tools for monitoring dynamic water movements and detecting water distribution in PEM fuel cells.

Table 2.1 shows a comparison of various imaging approaches for PEMFCs [6, 34].

Magnetic resonance imaging (MRI) with high resolution is used in small operating fuel cells. Magnetic metals cannot be used due to MRI's dependence on magnetic force. X-Ray microtomography, which has been used for soil saturation studies, has been put to use in ex-situ analysis of water distribution in diffusion media of a non-operating PEMFC. Additionally, neutron imaging method has been introduced to visualize the water droplet formation and movement in either flow field or electrode. With the advantage of its potential for use in an operating cell, it has become a preferable diagnostic tool to determine water distribution patterns in fuel cells.

Table 2.1 Summary of various direct visualization techniques used in PEMFCs [6,34]

Method	Spatial resolution	Temporal resolution	Merits	Challenges
Neutron Imaging	10-25 μm	5-30 s	Compatible with operating fuel cell and carbon materials	Only about a dozen institutions can perform it
MRI	25 μm	50 s	Compatible with operating fuel cell	Incompatible with carbon materials; limited spatial and temporal resolutions
X-Ray Tomography	3–7 μm	4.8 s	signal intensity can be correlated to through-plane water content	Not in an operating cell
Optical Photography	10 μm	0.06 s	Compatible with operating fuel cell; high temporal and spatial resolution	Transparent window requires substitution materials for operating fuel cell
Fluorescence Microscopy	5.38μm	0.3s	High spatial and temporal resolutions; signal intensity can be correlated to through-plane water content	Has yet to be demonstrated with an operating fuel cell

Neutron radiography was widely applied to measure water distribution in two-dimensional in-plane direction in a working fuel cell. Pekula et al. [35] reported, as shown in Figure 2.5, that the gas flow channels were occupied by liquid water, and therefore water flooding occurred inside the fuel cell. From the different flow channel geometries (2-channel pass design on anode and 3- channel design on the cathode), it could be concluded that liquid water was on the anode side. The authors attributed this to local pressure variations due to the change in momentum of the gas flow.

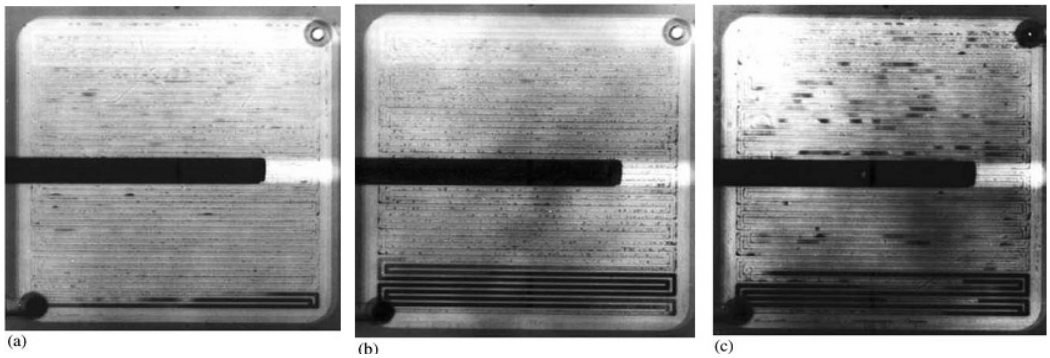

Figure 2.5 Water distribution for different reactants flow rate at same current density [35] (Reprint from Ref. [35], copyright 2005, with permission from Elsevier)

Satija et al. [36] demonstrated the use of neutron radiography in a fuel cell under operating conditions. A four-cell commercial stack was used in their study; the image-masking technique was used to differentiate water formation in the anode channels from that in the cathode channels, and the gas diffusion layer (GDL). In anode-masked image, it was observed that water was not evenly distributed throughout the flow channels. The similarity between the cathode mask and the water

density image implied most of the water was located on the cathode side of the cell.

In-plane water distribution cannot reflect the water content in each component of the fuel cell, besides, it is not evenly distributed in these layers. Thus, through-plane water distribution is more important for us to build up a three dimensional water distribution profile, help us modify the models for fuel cell, moreover, lead us to performance improvement and lifetime enhancement. Hussey [37] made efforts to visualize the in-situ through-plane water distribution in a PEM fuel cell. The spatial resolution was 30 μm. The images demonstrated that the water content in the anode GDL remained almost invariant, while a small amount of water accumulation appeared in the cathode GDL as more current was produced. Additionally, higher current would lead to an increase of the water content of the membrane.

Nowadays it is still difficult to directly visualize liquid water transport in gas diffusion layers in micro-scale, and even harder to make in-situ measurements in operating fuel cells. However, with the improvement of resolution of radiography techniques, there has been some progress to macroscopically visualize water distribution in through-plane direction. Neutron imaging at NIST has the capability of imaging with a spatial resolution of 10 μm. It will be used in this work for directly visualization of the water distribution in a GDL.

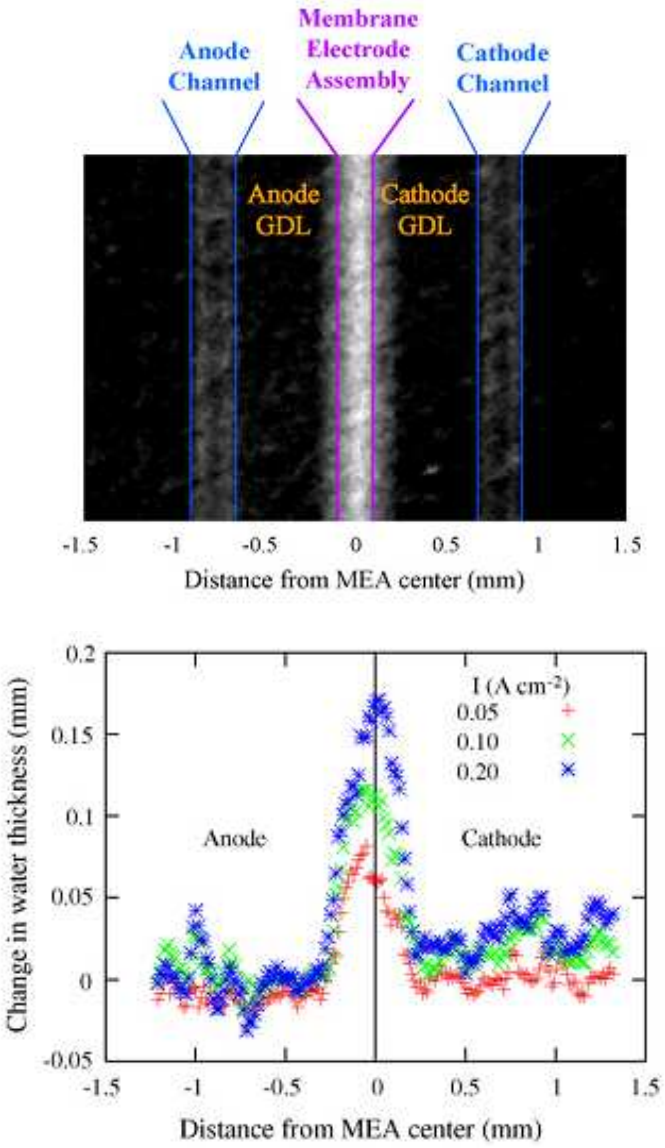

Figure 2.6 Through-plane water distribution in one dimension [37] (Reprint from Ref. [37], copyright 2007, with permission from Elsevier)

CHAPTER 3

Two-phase flow transport properties of gas diffusion layers used in PEM fuel cells

3.1 Introduction

Two-phase transport properties of porous media are crucial for water management strategies in PEM fuel cells. Different GDL treatment methods have been provided for better water management [38-40]. Hydrophobic treatments have been proven to eliminate excessive liquid water accumulation in the micro-scale pores of GDLs, and facilitate gaseous reactants transport. The heterogeneous nature of GDLs, such as the bimodal pore distribution and mixed wettability characteristics, greatly influences the liquid water flow inside the fuel cell system.

Furthermore, the channel-rib structure in PEM fuel cells creates inhomogeneous compression distribution along the GDLs. The GDL under the ribs is mostly compressed to the controlled thickness while the GDL under the channels remains virtually uncompressed and even intrudes into the channels, as shown in Figure 3.1 [23]. The morphological structure of the GDLs can be altered by local stresses and the multiphase transport characteristics would be influenced accordingly. Research study shows that compression for GDLs leads porosity to decrease, and tortuosity to increase [41]. The behavior of multiphase flow, characterized by different

transport patterns between the regions under the channels and ribs are expected to be changed by the non-uniform change of the surface area and the pore size in the discrete regions. Therefore, it is necessary to quantify the alterations in transport properties of a GDL under different compression loadings and channel/rib structures.

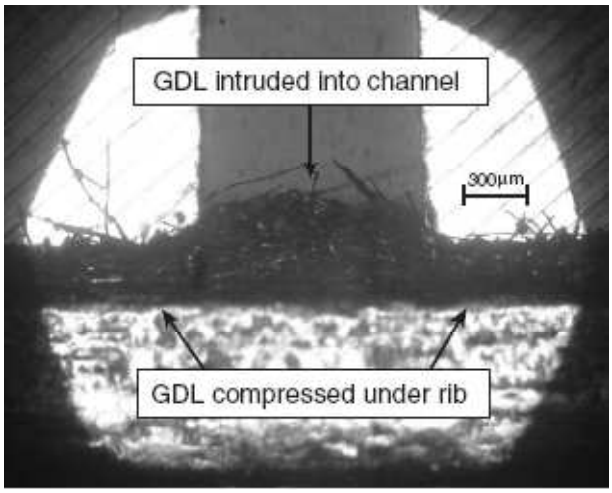

Figure 3.1 Cross-sectional view of the GDL [23] (Copyright Wiley-VCH Verlag GmbH & Co. KGaA. Reproduced from Ref [23] with permission)

Much work has been devoted to examining the morphology, wettability and compression effects on the fuel cell performance based on the polarization curve refined in mass transfer affected regime [21, 40-43]. However, no predictable correlation between fuel cell performance and changes in GDL properties has been established since the electrochemical measurements are governed by complicatedly coupled factors. It is difficult to deconvolute the effect of a single factor on transport properties. Additionally, accurate multiphase transport characterization of GDLs, such as an appropriate capillary pressure and liquid saturation relationship, is required

in PEM fuel cell modeling.

The influence of PTFE content, rib-channel structure, and compression on capillary properties of the commercial GDLs will be discussed in the following section.

3.2 Experimental Section

3.2.1 Experimental Materials

The GDLs used in this work are Toray TGP-H- 060 and Toray TGP-H- 090. Toray TGP-H- 060 is used to investigate the effects of PTFE content, while Toray TGP-H-090 is for compression effects studies. Figure 3.2 displays a scanning electron microscopy (SEM) image of Toray carbon paper. A carbon paper has a complex and anisotropic straight fibrous structure with various pore sizes ranging from few microns to tens of microns and is coated with Teflon® to increase the hydrophobic property in the gas diffusion layer.

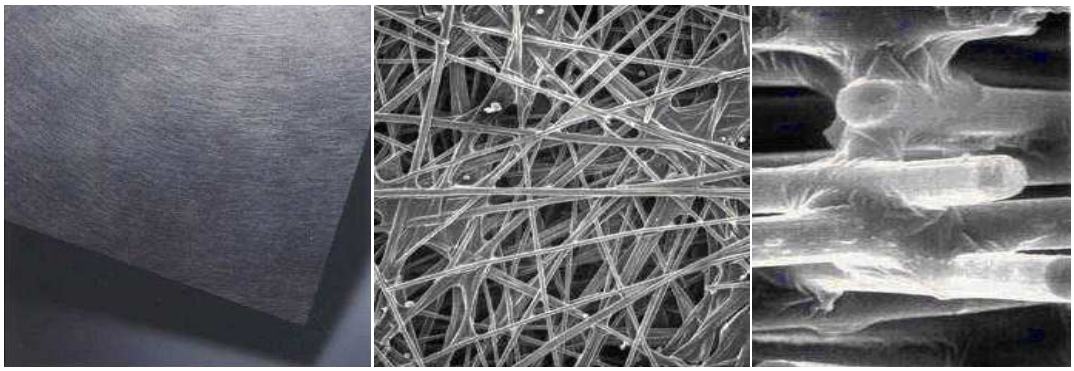

Figure 3.2 Toray carbon paper (left to right): TGP-H carbon paper, SEM surface, SEM cross section) [44](Image courtesy of Toray Composites (America), Inc.)

The porosity of GDLs is determined by the following equation (3.1):

$$\varepsilon = (\varepsilon_0 - \frac{\chi \cdot \rho_G}{\rho_t}) \quad (3.1)$$

Where ε_0 is porosity of the GDL without PTFE coating, ρ_G is the bulk density of the matrix, which is 0.44 g/cm^3 for carbon paper. The PTFE® content χ is given by the manufacturers in %, ρ_t is the density of Teflon, which is 1.2 g/cm^3. Table 3.1 shows the physical properties of Toray-H series.

Table 3.1 Basic data for Toray TGP-H series

Properties	Units	Toray TGP-H-060			Toray TGP-H-090
PTFE content	wt%	10	20	30	20
Thickness	μm	190	200	210	280
Porosity	%	75	71	67	71

3.2.2 Test Cells

A schematic of the test cell is shown in Figure 3.3. In our experiment, the sample is compressed between two end plates. The top plate is made of acrylic plastic and the bottom plate is made of stainless steel. Stainless steel is selected because its hydrophilic property can prevent formation of air pockets between the GDL and the bottom plate. The ribs are evenly distributed within the stainless steel plate to support the GDL. To prevent the sample from being over compressed, constant compression force is usually used by controlling the assembling torque. In this experiment,

constant compression is controlled by the thickness of metal shims placed between the two end plates, as shown in Figure 3.3(b). The two gaskets around the edges of the GDL are made of expanded Teflon® sheet. Gasket 1 is matched to the machined area of the stainless steel plate and gasket 2 is matched to that of a GDL. This arrangement is used to prevent water from flowing over the edges. When the plates are compressed, the edge portion of the sample sitting above gasket 1 is compressed, resulting in sealed edges to prevent water channeling through the edges. The total uncompressed thickness of the two gaskets is approximately 50 micrometers thicker than that of an uncompressed GDL to provide good sealing.

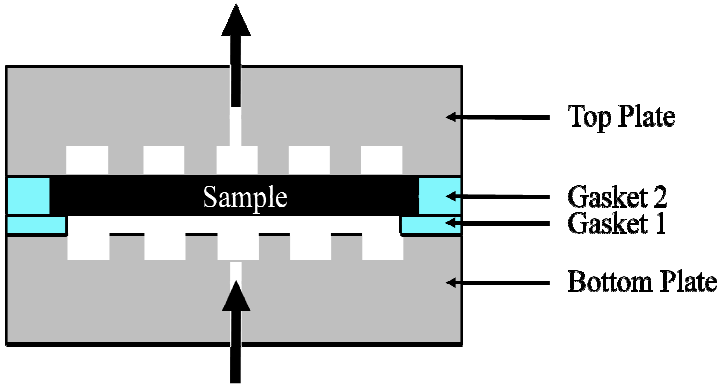

(a) Cross-sectional view of the fixture

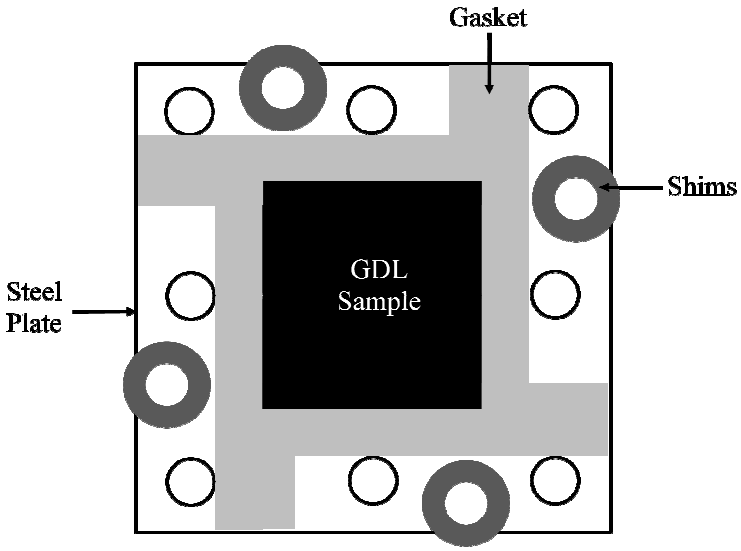

(b) Top view of the fixture

Figure 3.3 Schematic of the test cell

3.2.3 System Setups

A schematic of the volume displacement setup is shown in Figure 3.4 [33]. When liquid water is forced into the sample, it is not expected that all accessible pore volume is filled the moment the pressure is changed. The pressure-controlled approach ensures the system reaches equilibrium as the pressure is adjusted.

First, the horizontal tube is filled with water by the vertical tube as valve 3 is closed and valve 1 and 2 are open. It is important to deionize and degas the water before adding into the vertical tube because air bubbles in liquid piping can interfere with the liquid saturation measurement. Liquid water is intruded into the chamber through the bottom opening. The horizontal tube is aligned with the bottom of the

GDL sample, and valve 1 is closed. Valve 2 and 3 are open to fill the chamber below the GDL sample. The liquid water pressure is measured with a pressure transducer. The height of horizontal tube is raised or lowered to adjust the hydrostatic pressure to produce data for imbibition and drainage. The pressure transducer is located at the same level as the bottom of the sample, so the liquid water pressure is the reading value relative to the atmospheric pressure. By tracking the movement of the meniscus in the horizontal tube liquid saturation in the GDL can be obtained. Two ends of the openings are exposed to saturated air to avoid the evaporation effects [33]. The evaporation rate is determined by measuring the water volume change in the horizontal tube over 24 hours, which is $6.92*10^{-5}$ ml/min on average. This value depends on the temperature and relative humidity of the room and varies slightly from day to day.

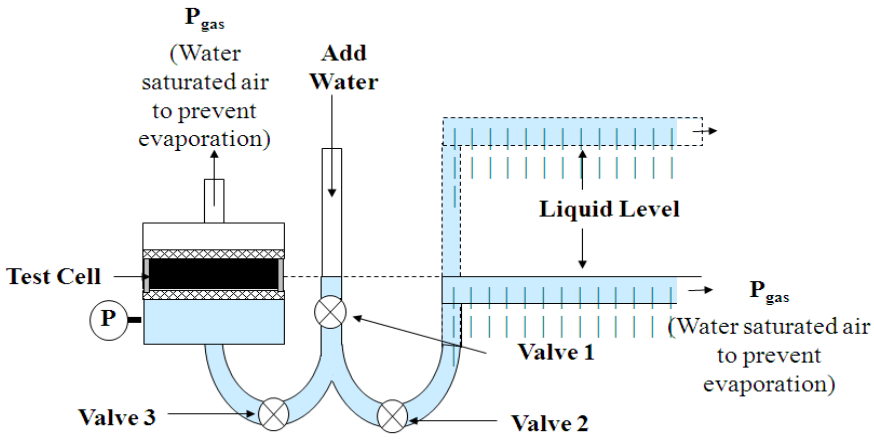

Figure 3.4 Schematics of volume displacement setup [33]

3.3 Data Analysis

Capillary pressure is controlled by adjusting the liquid pressure and calculated by equation 3.2.

$$P_c = P_{nw} - P_w = P_l - P_g \tag{3.2}$$

P_g is the atmospheric pressure. P_l is the liquid water pressure.

A typical liquid pressure versus liquid volume curve is shown in Figure 3.5. Each cycle includes a drainage and imbibition curve. The sample is initially dry and the water uptake is determined by the volume change after the inflection point. The fill-up curve is used to determine the inflection point. The horizontal section of the fill-up curve is the liquid water volume we need to fill the chamber. The inflection point refers to the starting point at which liquid water is assumed to completely fill the chamber below the sample. After this point, the liquid begins to penetrate into the sample. The starting point could be determined from the liquid pressure versus liquid volume curve during the fill-up process.

In general, fluids with contact angle between 55° and 125° are considered intermediate and often exhibit mixed and complex wetting tendencies [33]. Such GDL sample would not spontaneously absorb the liquid water unless the liquid pressure needed for penetration into these carbon materials exceeds the gas pressure. There is a significant liquid pressure change at the liquid water penetration point [33].

Based on the data in Figure 3.5, a typical capillary pressure curve reflecting relationship between capillary pressure and saturation can be derived. The saturation level is given by the equation 3.3 below:

$$\varepsilon' = 1 - \varepsilon \cdot \frac{t_{uncomp}}{t_{comp}} \quad \text{(3.3-a)}$$

$$V_{comp.void} = V_{total} \cdot \varepsilon' \quad \text{(3.3-b)}$$

$$S_w = \frac{V_{dis}}{V_{comp.void}} \quad \text{(3.3-c)}$$

V_{dis} is the displaced water volume, ε is the porosity of uncompressed GDL sample, ε' is the porosity of compressed GDL sample V_{total} is the total volume of GDL sample, $V_{comp.void}$ is the void volume of compressed GDL sample, t_{comp} is the thickness of compressed sample (controlled by thickness of the shims), t_{uncomp} is the thickness of uncompressed sample.

3.4 Results and Discussions

3.4.1 Effects of Channel/Rib Structure

Channel/rib structure, to some extent, causes non-uniform compression along the GDL, and consequently affects the pore geometry. In order to investigate the effects of channel/rib structure on two-phase flow transport, two configurations were designed, as shown in Figure 3.6.

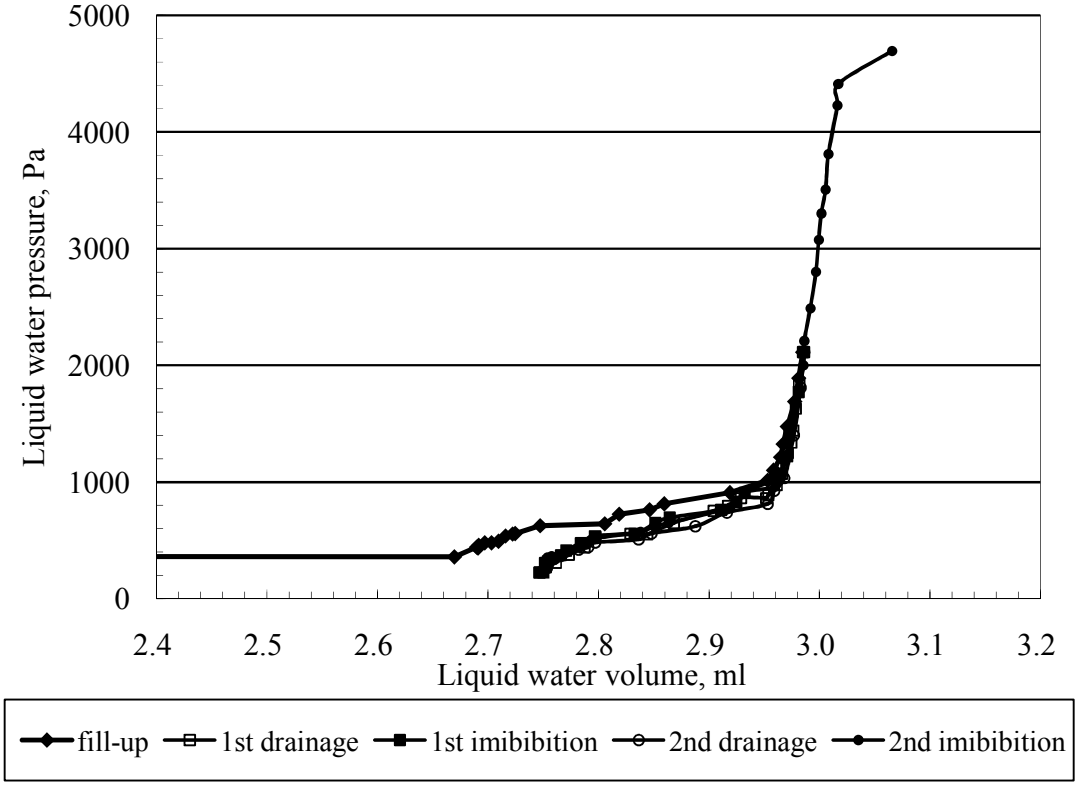

Figure 3.5 Liquid water pressure versus displaced volume curve

3.4.1.1 Experimental Configurations

Configuration 1 is the same test cell described in section 3.2.2. In configuration 2, a hydrophilic porous plate (from Scientific Commodities, Inc) is employed to support the GDL sample at the bottom, while a hydrophobic porous plate is placed at the top of the GDL. The hydrophilic plate remains completely saturated. The hydrophobic porous plate is dry, allowing air to go through freely. The bubble point of this hydrophilic layer is measured at – 4500 Pa and breakthrough point of hydrophobic layer is 8500 Pa, as long as the capillary pressure in the imbibition-drainage cycles is

kept within this range, liquid water will maintain its continuity in the GDL.

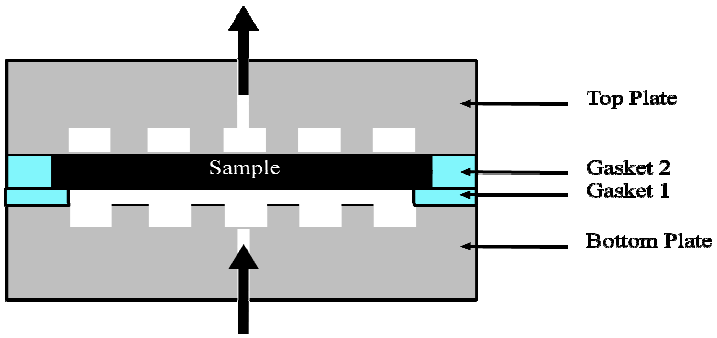

(a) Configuration 1

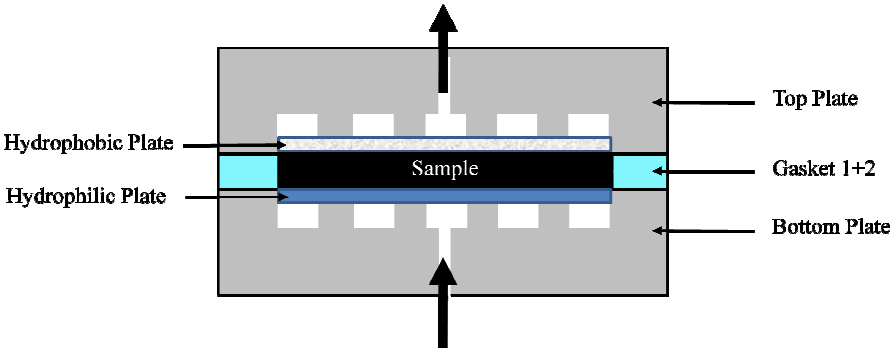

(b) Configuration 2

Figure 3.6 Two different configurations used for capillary pressure curve measurement

3.4.1.2 Comparison of Experimental Results between Different Configurations

In the evaluation of fuel cell performance, the channel/rib structure has been investigated [45-46], including the effects of the number of channels and the ratio of channel/rib widths. Optimized value for the ratio is found to be no greater than 1 [46] so that the ohmic resistance and gas flow rate can be balanced. In our designed

configurations, the ratio between channel and rib width (C/R) is chosen to be 1:1 and 1:1.5.

The capillary curves of Toray TGP-H-060, 10 wt% wetproof for two different configurations were shown in Figure 3.7 and the results were compared with Heebong's data [9]. The test cell used in Heebong's data is the same as that used for curve 2 but without shims on the edges to control the thickness. The discrepancy of the results is apparent. Even though Heebong's data using the same test cell structure as curve 2, the slightly higher injection pressure is found in curve 2. Unlike Heebong's data in which the thickness of GDL in well-sealed cell cannot be clearly determined, the thickness of the GDL in present study is controlled by shims on the edges and is known as 25 μm less than that of the uncompressed GDL. The higher capillary pressure in the large saturation change section in curve 2 is likely to be caused by higher compression of the GDL. While, the saturation level ranges in Heebong's data compared favorably to that in curve 2. This is expected in that same channel/rib structures are applied in curve 2 and Heebong's experiment.

By comparing saturation levels in curve 2 with that in curve 3 at the same capillary pressure, it is found out that with the same configutation, the lower the ratio of channel/rib width is, the less saturation level is shown in the curves. GDL is almost uncompressed between the channels but rigidly compressed between the ribs. This

fact leads to significant local variations in porosity and tortuosity and it therefore has an effect on mass transport through the GDL. C/R ratio of 1:1.5 leads to lower effective porosity in the GDL and lower liquid water saturation level. This effect is further demonstrated by the difference in the shapes of the capillary pressure curves between curve 3 and curve 4. With the same C/R ratio, curve 4 shows the capillary curves for configuration 2, while curve 3 is the capillary curves for configuration 1. Apparently, curve 4 has the least saturation level range. This is because the whole GDL area is compressed between two porous plates in curve 4, no intrusion into the channels occurs. In this study, a single value of porosity ε' in equation 3.3 was assumed in two configurations; non-uniform compression effect on porosity distribution in configuration 1 is not taken into consideration.

The effect of rib/channel structure on saturation level distribution in both through-plane and in-plane directions will be further demonstrated by neutron radiography in Chapter 4.

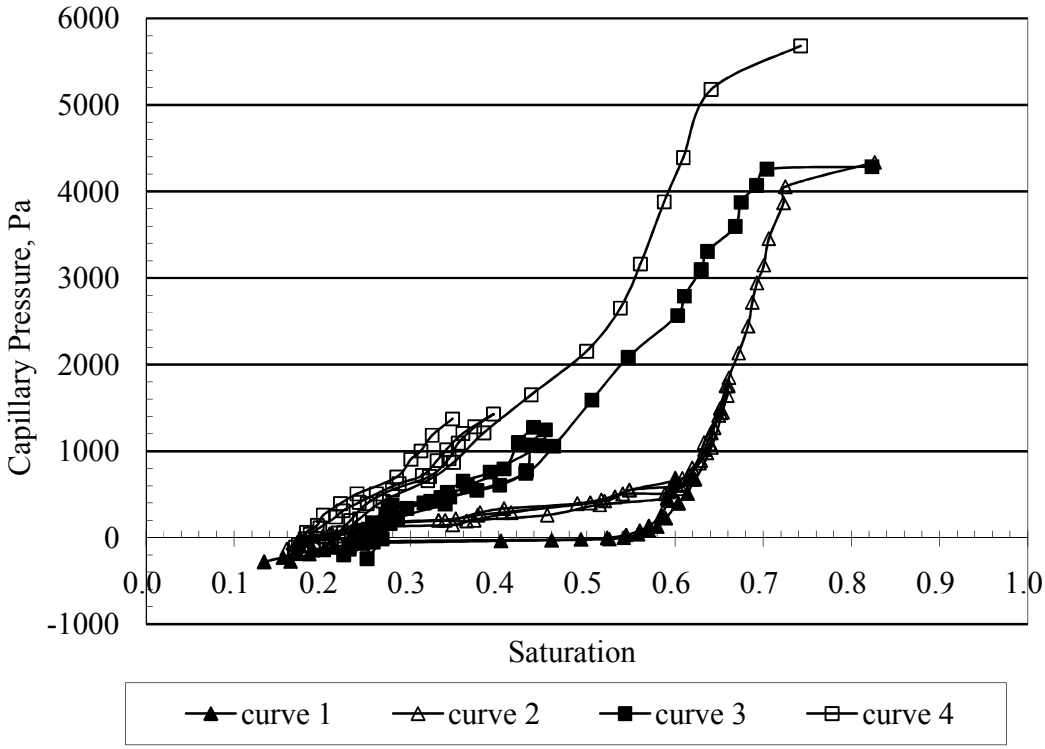

Figure 3.7 A set of capillary curves for Toray TGP-H-060, 10% wetproof. Curve 1 is the data from Heebong (configuration 1 with the ratio of C/R at 1:1), curve 2 is measured by using configuration 1 with the ratio of C/R at 1:1, curve 3 is measured by using configuration 1 with the ratio of C/R at 1:1.5, curve 4 is measured by using configuration 2 with ratio of C/R at 1:1.5.

3.4.2 Effects of PTFE Content

Hydrophobic treatment has been proved to prevent spontaneous wicking of water into GDL pores, and affect fuel cell performance accordingly [47-48]. It is important to connect PTFE treatment steps with quantitative measurements of liquid water inside the GDL. In this section, a series of Toray TGP-H-060 with various PTFE content are tested. The specific details of each material used in the experiment are listed in Table

3.1.

Capillary curves for Toray TGP-H-060 with 10 wt%, 20 wt%, 30 wt% wetproof for configuration 1 are shown in Figure 3.8. The curves follow the similar trend with each other, but exhibit slight qualitative differences. Toray TGP-H-060 treated with 10 wt% wetproof reaches saturation S_w of 0.43 at P_c 1500 Pa, whereas the ones with 20 wt% and 30 wt% wetproof have saturation of 0.38, 0.39 respectively at the same capillary pressure. This phenomenon can be attributed to the fact that more hydrophobic fluoropolymer covers the surface of graphite carbon, accordingly, reduces the hydrophilic connection pathways. It is also observed that increasing Teflon loading, beyond 20 wt% wetproof, has little effect on the capillary property of GDL samples because additional fluoropolymer is not uniformly covering graphite carbon surface, instead, it thickens the existing coating of Teflon [49]. Previous studies showed the similar threshold value of wetproof in carbon paper for the capillary pressure measurement. Kumbur et al [50] found the difference of capillary curve observed between 5 and 10 wt% papers is larger than that between 10 and 20 wt% in SGL paper. Lobato et al [51] observed no obvious change of capillary curve for E-Tek paper from 40 wt% wetproof down to 10 wt%.

Besides, the pressure for the entire saturation range shifts to more positive value with the addition of Teflon. This can be explained by the fact that the surface

becomes hydrophobic as graphitic carbon is covered with the fluoropolymer [32]. Moreover, no apparent hysteresis is observed. According to the literature [52], the hysteresis in typical capillary pressure curves is attributed to the fact that drainage of a wetting phase from a pore is controlled by the size of the throats whereas imbibition of a wetting phase into a pore is controlled by the size of the pore body. Therefore, capillary pressure is lower for water withdrawal than that for water imbibition. It could be deduced that within such low capillary pressure range, the liquid water has no accessibility to the small pores. Both imbibition and drainage happen within the body of relatively large pores. Therefore, hysteresis is hardly observed from our experimental results.

The breakthrough point is determined by the drastic saturation change as liquid water breaks through the sample. Figure 3.8 shows the significant liquid volume uptake as it reaches the breakthrough point. Once water breaks through the sample, the test is terminated. The saturation level for Toray TGP-H-060, 10% wetproof reaches 65% before breakthrough occurs. While, the saturation levels of the sample with 20% and 30% wetproof are up to 55%, 48% respectively at the breakthrough point. Such high saturation levels at the breakthrough point are caused by the fact that full face injection allows numerous dead-end liquid clusters to enter the GDL from the bottom surface. These clusters occupy the porous space without penetrating the

GDL, causing high saturation level before water breakthrough [52]. The saturation levels decrease as the Teflon loading increases from 10wt% to 30wt%. This is because the hydrophobic fluoropolymer decreases the total connected hydrophilic pathways, thus reduces the potential water retention capacity.

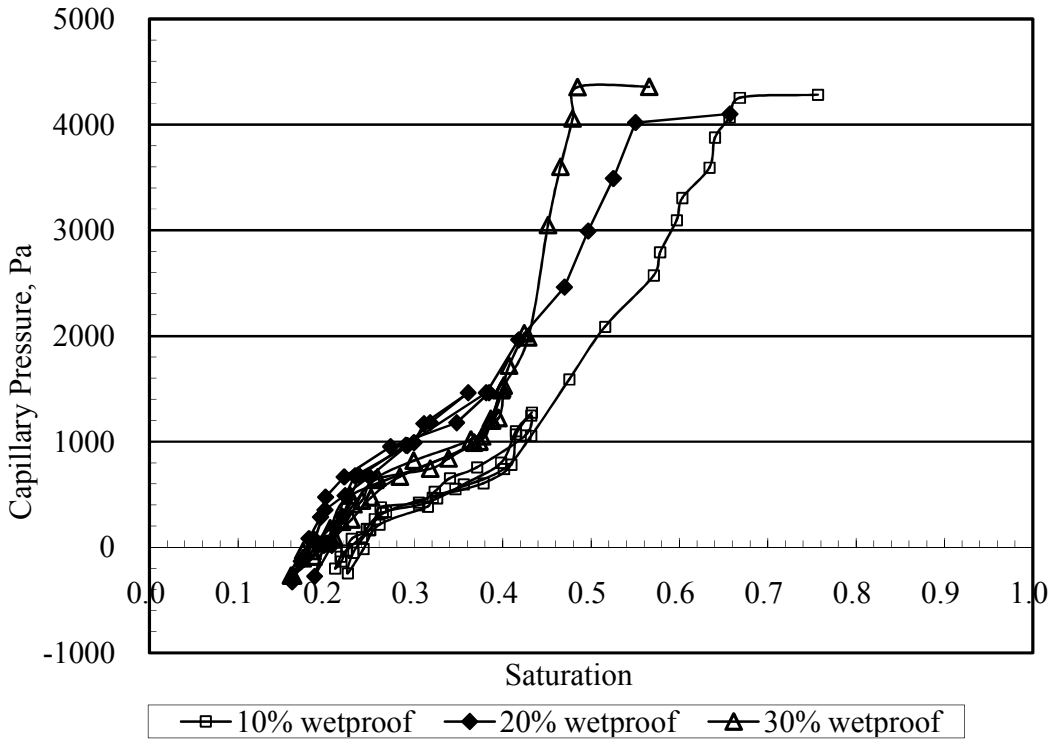

Figure 3.8 Capillary curves for Toray TGP-H-060 carbon papers

3.4.3 Effects of Compression

In a fuel cell stack, an optimum assembly pressure is required to prevent leakage and assure surface contact between different components. Low compression could cause an increase in gas leakage and electrical contact resistance, while excessive

compression could lead to permanent deformation of the GDL due to both morphological changes and possible loss of hydrophobicity [20]. Such changes would not only affect the electrical properties in fuel cells but also capillary transport properties in the GDLs. In this work, the effect of compression on the capillary curves is examined by altering the thickness of shims to illustrate the effect of assembly pressure on the transport characteristics of the GDLs.

In this experiment, Toray TGP-H-090 is applied for compression effect studies because Toray TGP-H-090 is thicker than Toray TGP-H-060 and thicker GDL amplifies the effect of compression on reduction in pore volume so that the changes on capillary pressure curves can be evidently observed [53]. Comparing Toray TGP-H-090 with thickness of 280 μm, TGP-H-060 with the approximate thickness of 200μm shows more compact and rigid structure and appears to be less resistive to deformation. For Toray TGP-H-060, the difference of capillary curves upon different compression may be not distinctive enough to illustrate the effect of compression.

Figure 3.9 shows the capillary pressure curves of Toray TGP-H-090 with 20 wt% wetproof for configuration 1. The extent of compression is controlled by different shim thicknesses, which are 200 μm, 225 μm, 275 μm, respectively. Each curve shares the similar trend in low capillary pressure range, but differentiates from each other quantitatively at higher capillary pressure. Higher capillary pressure is required

to maintain the same saturation level as the compression increases because the compression can cause a decrease in the pore size.

The compression effect on capillary pressure curves is distinctive as the shims thickness changes from 275 μm to 225 μm, whereas there is almost no variation of capillary pressure curve after the thickness reaches as low as 200μm. Referring to stress - strain relationship [545453], the compressive strain governs the degree of the pore size reduction, and the increase of stress corresponds to shims thickness decrease. In this relationship, it shows that the compressive strain is sensitive to changes in compression pressure, and reaches a maximum value after a sharp increase in the slope of the stress - strain curve. The increasing slope can be attributed to increase in stiffness of the GDL with compression. As the GDL is compressed, the available pore space reduces and affects the capillary pressure within the pores. This explains the reason for the substantial increase in capillary pressure as the thickness of shims decreases from 275 μm to 225 μm. While the negligible change of the capillary curve for shim thickness at 200 μm demonstrates that the carbon paper cannot be compressed unlimitedly.

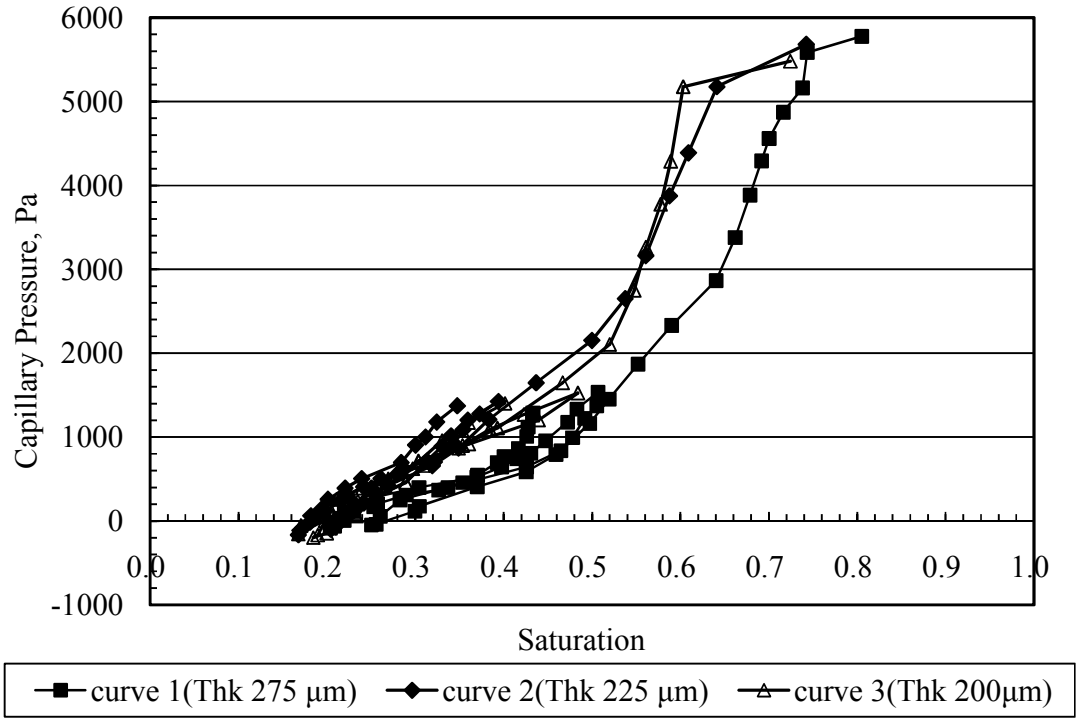

Figure 3.9 Capillary pressure curves for Toray TGP-H-090, 20% wetproof under different compression in configuration 1

For configuration 2, the capillary curves with different thickness of shims were shown in Figure 3.10. Same as configuration 1, higher capillary pressure is required to reach the same saturation level as the compression increases. The breakthrough pressure increases as compression force rises in configuration 2, whereas the breakthrough pressure in configuration 1 does not change with compression. This is due to the fact that the sample is partially compressed in configuration 1 but rigidly compressed in configuration 2. The rigid compression in configuration 2 results in that the effective porosity reduced dramatically. Such reduction eliminates the

pathway for liquid water breakthrough and higher capillary pressure is needed to force water out of the GDL. Comparing the capillary curve in Figure 3.10 with that in Figure 3.9, the capillary pressure curves for configuration 2 have a smaller range of saturation level than those for configuration 1, such phenomenon is attributed to channel/rib structure, which has been explained in detail in section 3.4.2.

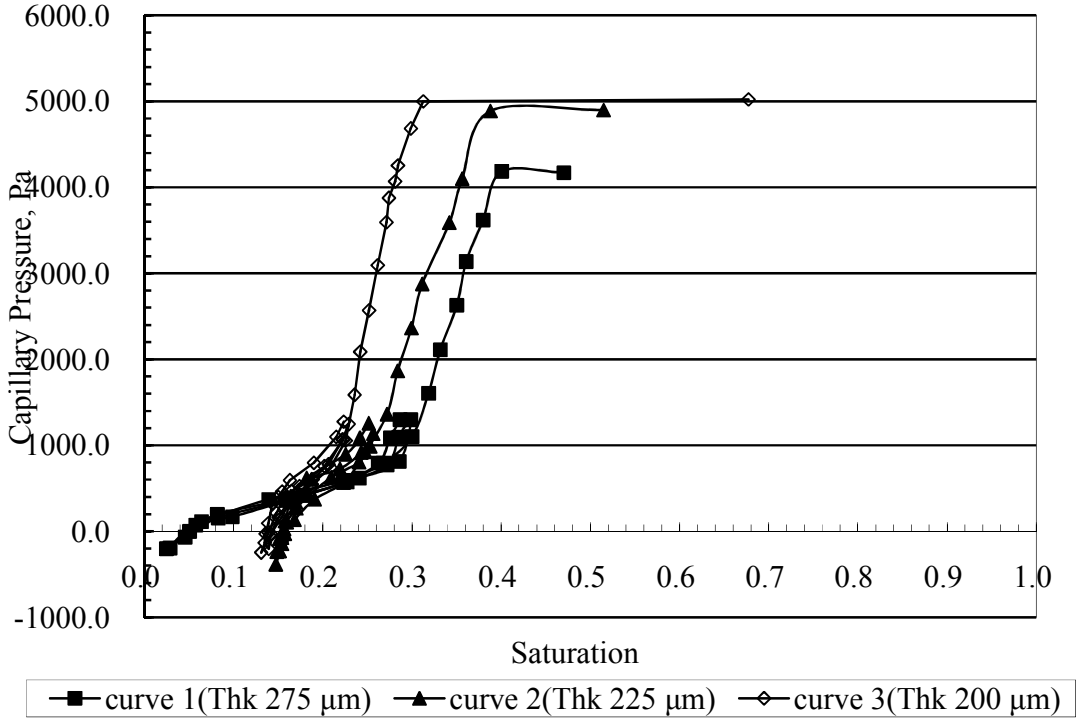

Figure 3.10 Capillary pressure curves for Toray TGP-H-090,20% wetproof under different compression in configuration 2

3.5 Conclusions

The capillary curves for two different configurations have shown indirect evidence of spatial variation in local transport properties. As the channel-rib width ratio reduces, less volume of the pore space is available for liquid water to fill in the GDL, therefore,

the saturation level decreases. The results also show that threshold value of wetproof in carbon paper for the capillary pressure of Toray TGP-H-060 is around 20%, since additional fluoropolymer is not uniformly covering graphite carbon surface, instead, it thickens the existing coat of Teflon. Compression has been proved to lead to different morphological properties and capillary characteristics.

The discontinuity of the surface contact area at the channel/rib interface creates inhomogeneous compression distributions, yielding changes in local physical properties of the GDL. The portion of the GDL in contact with the ribs suffers higher compression, whereas the portion under the channel experiences less compression and tends to intrude into flow channels. This may yield discrete regions with different characteristic pore radii, thus resulting in different transport properties, such as non-uniform saturation level distribution. Therefore, the capillary transport in porous media cannot be sufficiently characterized through the concept of an average saturation vs capillary pressure, since each region in GDL exhibits distinct capillary behaviors. Instead, an improved approach to analyze the transport would be to construct a finite number of discrete zones that represent the measured morphology (*i.e.*, pore size and wettability) and corresponding capillarity characteristics. A conceptual schematic is shown in Figure 3.11.

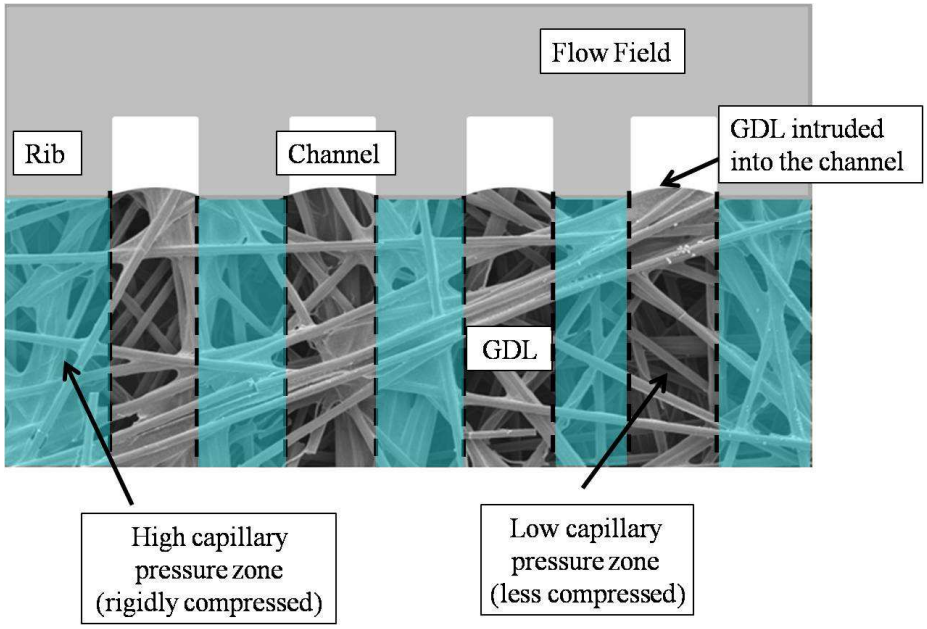

Figure 3.11 A conceptual schematic of discrete zones representing spatial variation of capillarity characteristics

CHAPTER 4

Neutron radiography of water distribution in a gas diffusion layer

4.1 Introduction

Over past decades, a variety of novel inspection techniques has been introduced for visualizing water distribution inside the fuel cell. This can be done either through transparent cell based on optical diagnostics, such as fluorescence spectroscopy or a graphite/metal cell visualized by neutron transmission radiography, X-ray tomography [54].

For fluorescence spectroscopy, a probe molecule sensitive to water content is added to the objects. The probe molecule is first triggered by the light emitted from a xenon source and the emitted light is collected through an optic window inserted in the membrane. However, only qualitative information about water content in porous media can be obtained by fluorescence spectroscopy method because depth perception from the top of the transparent window is limited [55].

X-ray and neutron radiographic methods share several similarities. For example, the intensity of an initial radiation source used in both techniques is attenuated as it passes through an object. The attenuation is measured and creates an image, or radiograph. Figure 4.1 shows the comparison of the attenuation coefficients between

both techniques. An atom's orbital electrons attenuate X rays. Thus, X-ray attenuation steadily increases with increasing atomic number due to the increasing orbital electron count. However, the difference of attenuation between carbon and water is not evident enough to differentiate these two molecules because they have very close atomic numbers. Besides, because of the highly reflective nature of GDLs, it is hard to differ carbon materials from water, making it almost impossible to quantitatively evaluate the volume of water [56].

Comparing with X-ray radiography, neutron attenuation occurs through interaction with the nuclei in a material. Hydrogenous materials, such as water, significantly attenuate neutrons. Compared to water, metal materials used in fuel cells, such as aluminum or stainless steel, are transparent to neutrons. This characteristic of high sensitivity to hydrogen and relatively low attenuation of neutrons of metals are suitable for imaging distribution of water content in PEMFC which consists of copper, aluminum and carbon.

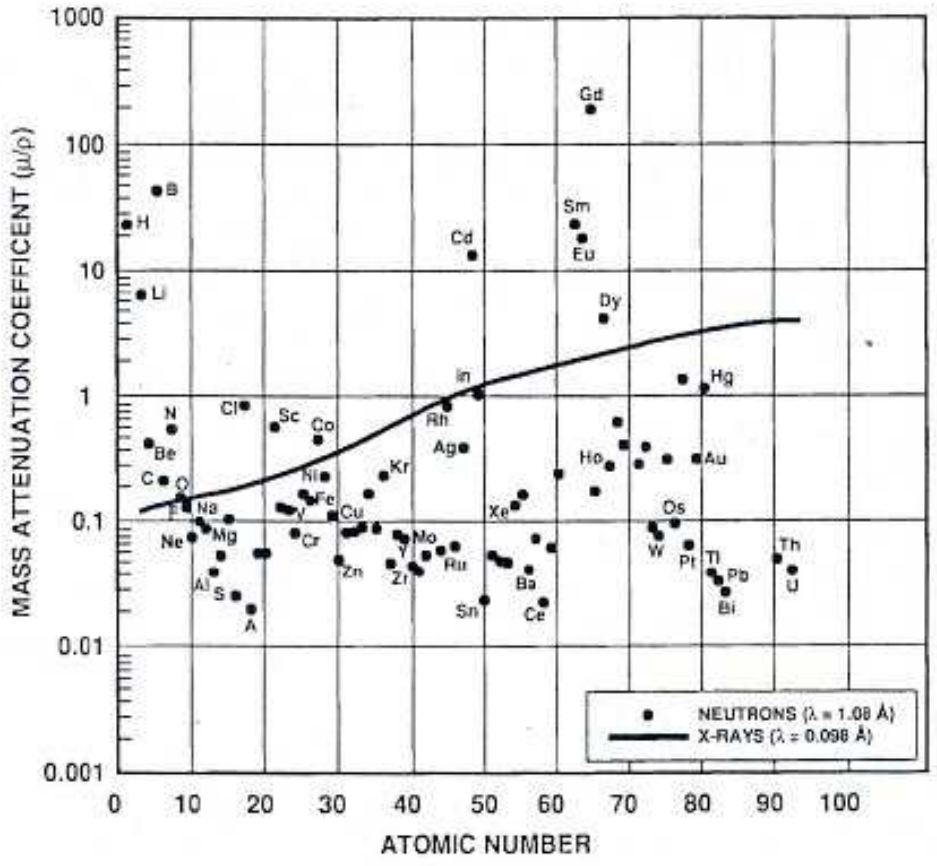

Figure 4.1 Neutron and X-ray attenuation coefficients versus atomic number [56]

4.2 Neutron Imaging Mechanism

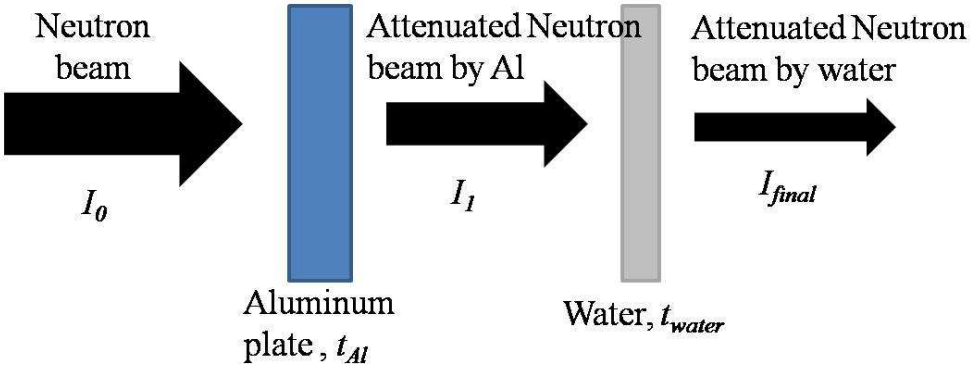

Figure 4.2 Diagram that represents the neutron imaging mechanism

As shown in Figure 4.2, if a beam of neutrons with an intensity of I_0 passes through an aluminum plate with a thickness of t_{Al} and porous media which contain liquid water with a thickness of t_{water}, then the intensity of attenuated neutrons I_{final} is calculated with the following equation:

$$I_{final} = I_0 \cdot e^{-\Sigma_{Al} \cdot t_{Al}} \cdot e^{-\Sigma_{water} \cdot t_{water}} \quad (4.1)$$

High energy neutrons (MeV) are created by fission reaction. The high energy neutron beam is filtered out by a single crystal bismuth filter which is transmissive to thermal neutrons when cooled down to 77K. The filtered beam is then collimated with a thermal neutron pinhole. The neutron beam is then attenuated by the elements within the cell, I_{final}, as described by Eq.(4.1). A scintillation screen contacted with the detector converts the intensity I_{final} to visible light. This visible light is converted into photoelectrons which are intensified by the image intensifier. Then the photoelectrons are focused onto an output phosphor. The visible light with greater intensity is converted by the output phosphor. The resulting light is captured by the CCD camera and converted to a digital gray scale image [57]. Figure 4.3 shows the schematic diagram of neutron imaging.

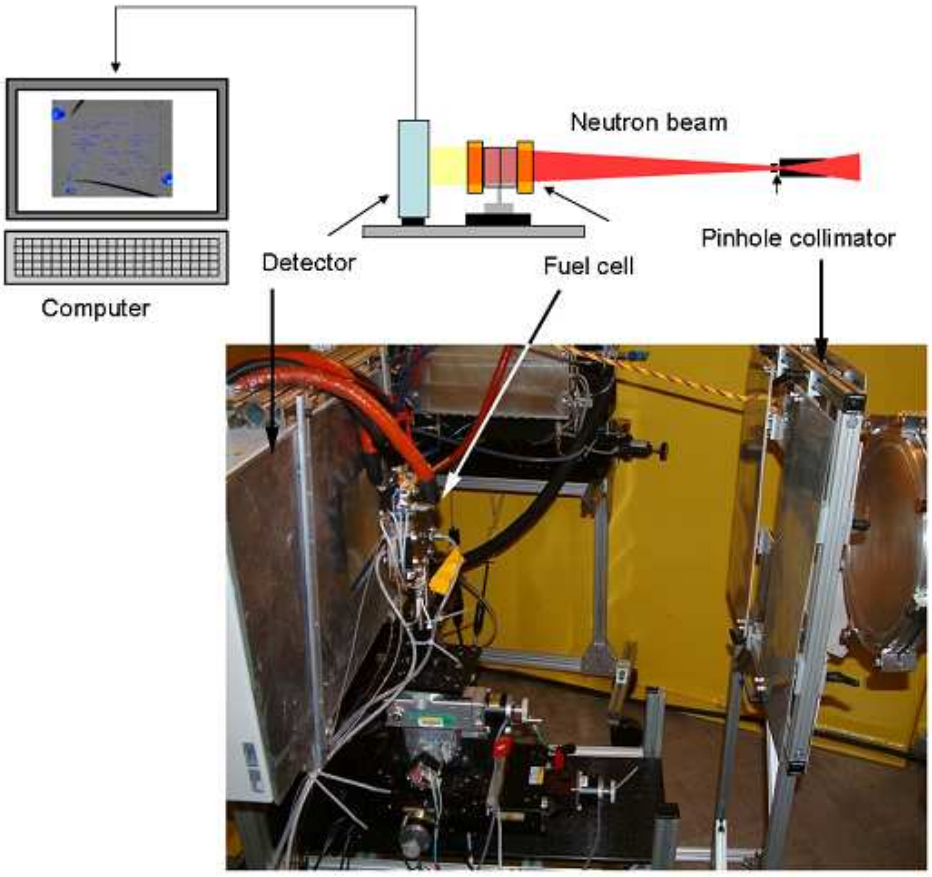

Figure 4.3 Experimental setup of neutron radiography at NIST [57] (Reprint from Ref. [57], copyright 2007, with permission from Elsevier).

4.3 Experimental Section

4.3.1 Experimental Setups and Procedure

Experiments were conducted at Beam Tube 2 (BT-2) of the Center for Neutron Research (NCNR), a research center of the National Institute of Standards and Technology (NIST). Details on neutron imaging were described in Figure 4.3. A schematic of the fixture used in this neutron imaging study is shown in Figure 4.4.

The GDL sample was aligned between two end aluminum plates. The edges of the sample were sealed with Teflon gasket. The dimensions of the aluminum end plates are shown in Figure 4.5. The GDL sample used in this study was Toray TGP-H-120 with 10 wt% wetproof, which has an uncompressed thickness of 370 μm. Sample size was 2 cm * 1 cm. In the measurement, the sample thickness was controlled by the thickness of the metal shims placed between the two end plates.

The sample was exposed to a neutron beam in the *z* direction. Images were collected by a detector on the other side. Liquid water was introduced from the bottom of the sample, and pressure was recorded by a pressure transducer below the sample. The capillary pressure was controlled within the range of liquid water breakthrough point by a microfluidic pump. The pump rate was 0.01 ml/hr.

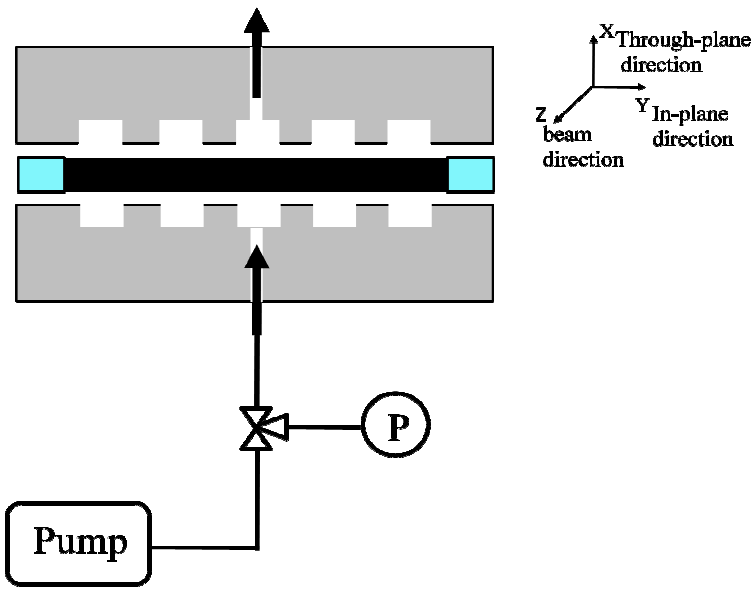

Figure 4.4 Micro-pump system setup

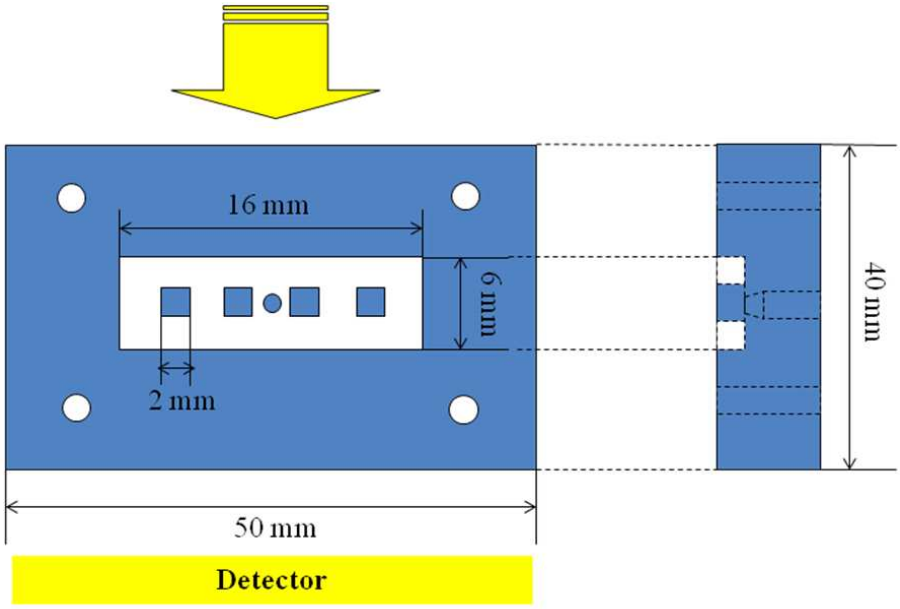

Figure 4.5 Dimensions of the aluminum end plates

4.3.2 Image Analysis

The relationship between gray value within the digital image and neutron beam intensity can be described as below:

$$G = CI_{final} + G_{offset} \tag{4.2}$$

C is amplified light coefficient emitted by the image intensifier output phosphor, G_{offset} is gray level offset value resulting from charge build-up in the CCD. This can be obtained by taking the dark image, which is also regarded as background image.

The background images were acquired while the neutron beam was not active. Because of the additive and constant nature of this offset to a pixel's gray level, G_{offset} can be effectively removed from any captured image by simply subtracting the dark image. Once the background image was obtained, this data was averaged and

subtracted from image data.

After gaining the background images, neutron beam was tuned on; two sets of data were taken: dry images and wet images. Before the wet images were acquired, a series of the dry sample ware taken and averaged as the reference image. The water content in the sample was then calculated based on the difference between the wet image and the reference image.

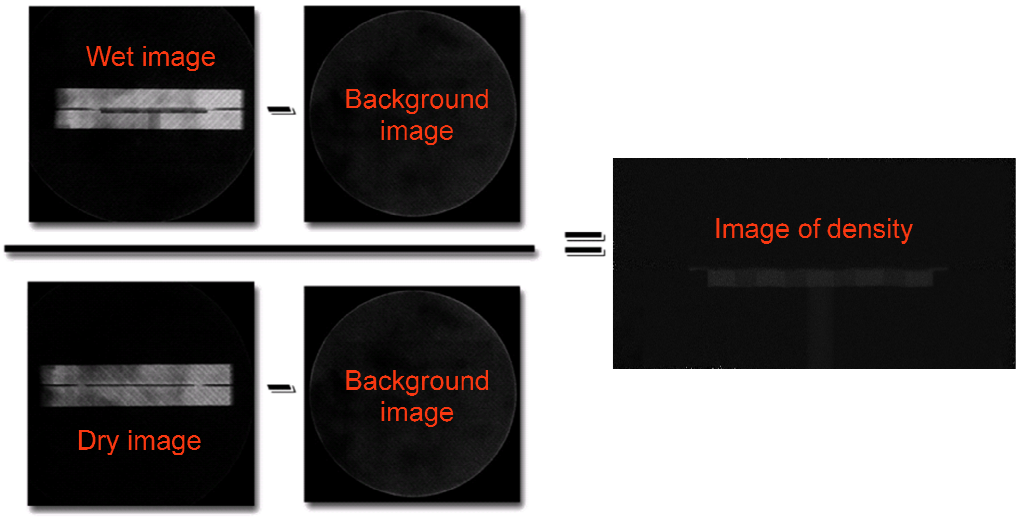

Figure 4.6 Transmission image

4.4 Results and Discussion

The wet image is shown in Figure 4.7(a), in the bottom end plate, liquid water was introduced into the water reservoir by the inlet below the channel in the middle of the fixture. The dark area is channel, which is filled with liquid water. The gray area is the region with 2 mm*2 mm rib, and filled with less amount of water. The contrast in

grayness level in these two regions is due to the water thickness difference between the regions in the channels and ribs. A line profile that plots pixel gray level value versus the distance in the in-plane direction is shown in Figure 4.7 (b). The gray block above the bottom plate is gas diffusion layer.

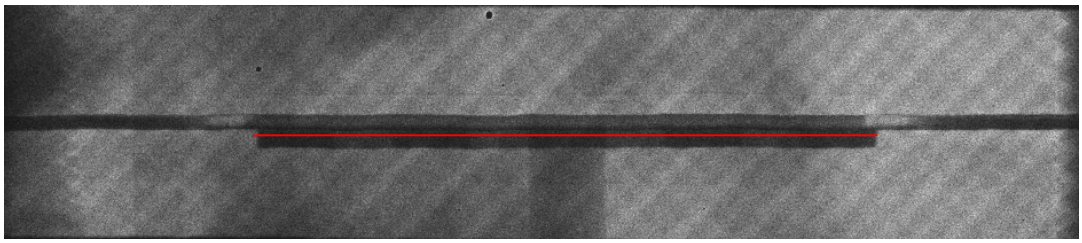

Figure 4.7 (a) Wet image of neutron imaging

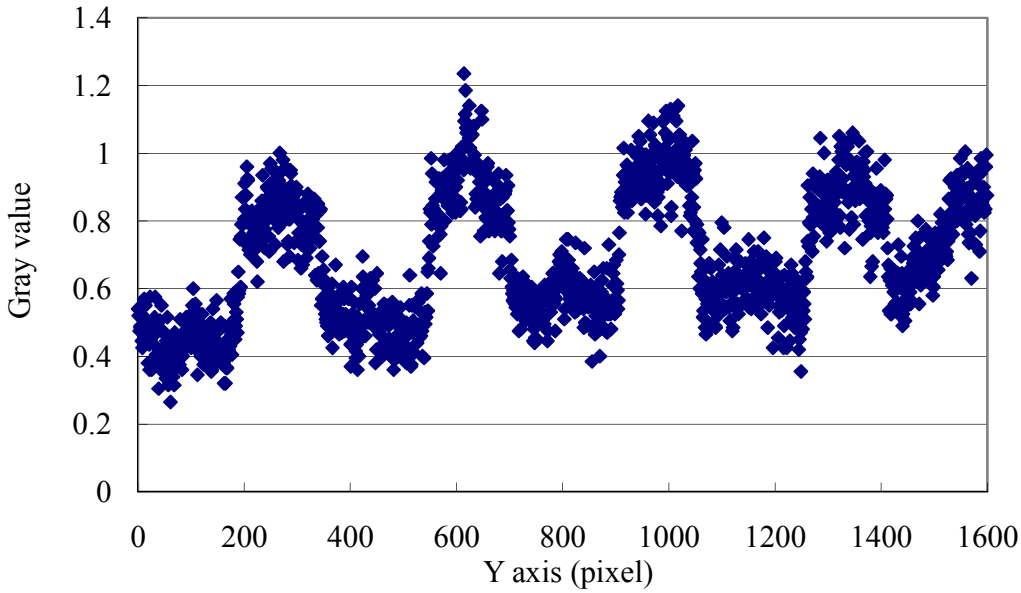

Figure 4.7 (b) Line profiles of pixel gray level values along the red line in the wet image

The density image in Figure 4.8 (a) is converted to water thickness by an image

analysis software. Since the water thickness in both channel and rib regions are known, which are 6 mm and 4 mm respectively, a line profile of water thickness along the in-plane direction can be used as a secondary calibration for the neutron images. The profile of water thickness is shown in Figure 4.8 (b).

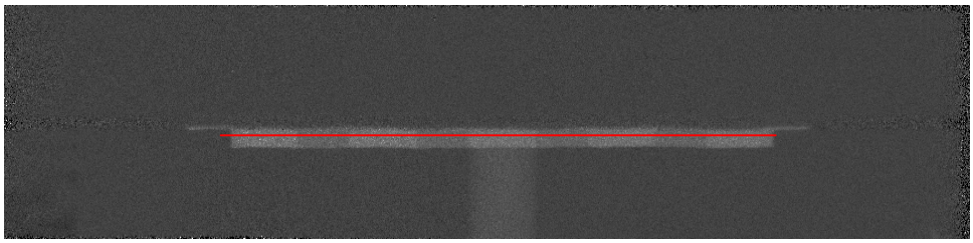

Figure 4.8 (a) Image of density in wet sample

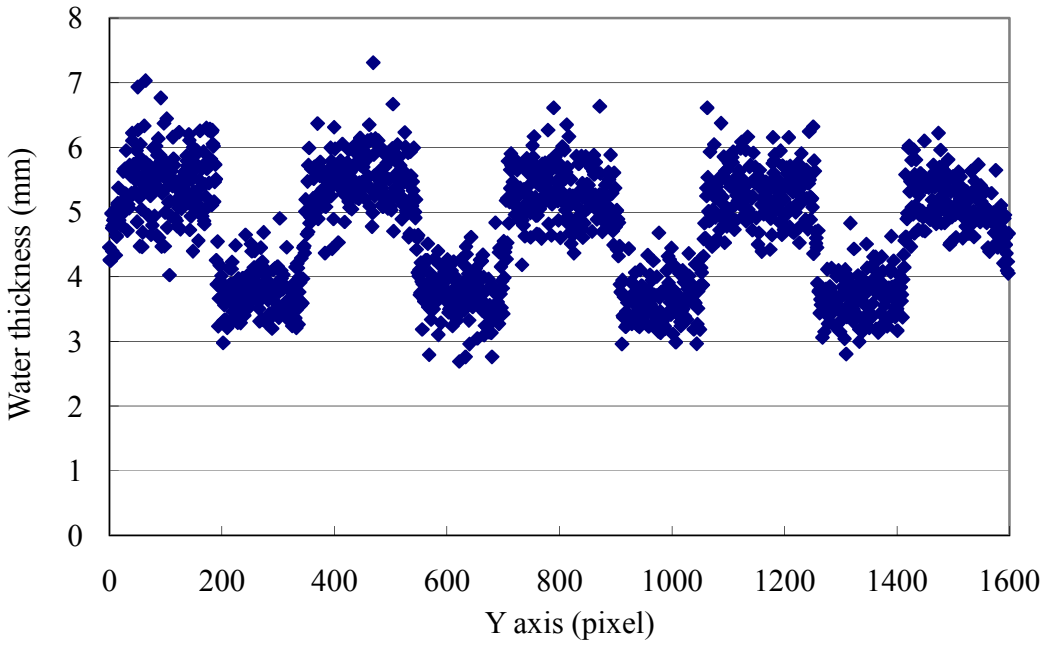

Figure 4.8 (b) Line profile of water thickness along the red line in Figure 4.8(a)

The rib-channel structure creates an inhomogeneous compression distribution because the GDL region between the ribs was compressed to the metal shim thickness

while the GDL region between the channels was less constrained. In order to investigate the effect of compression on the water distribution in GDL sample, the water thickness distribution in two different positions ('a' and 'b') along the through-plane direction was compared, as shown in Figure 4.9. The water thickness distribution along these two positions before breakthrough point is shown in Figure 4.10.

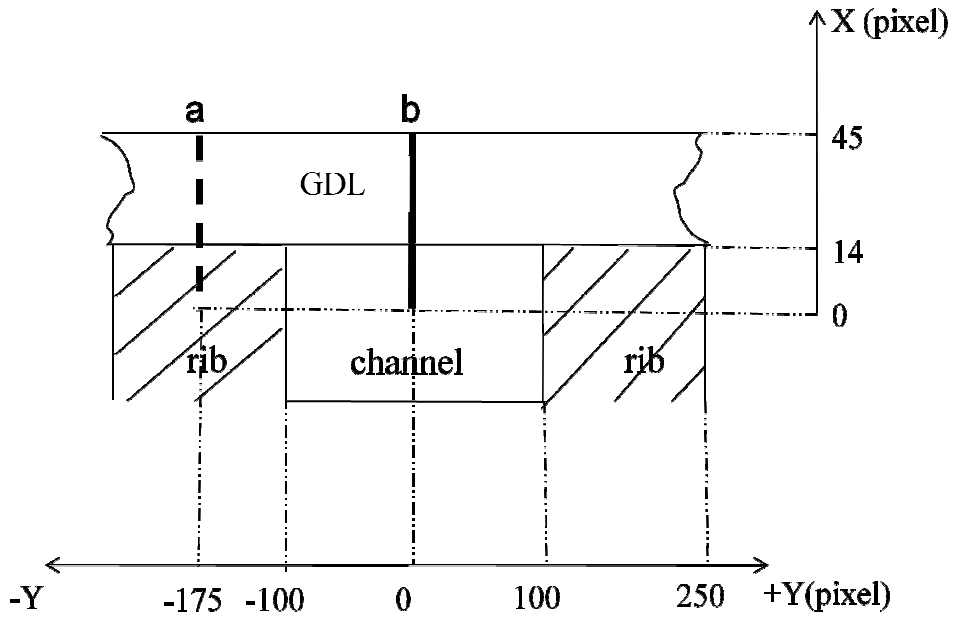

Figure 4.9 A representive diagram of two positions (a and b) for investigation of the effect of compression on the GDL (position a: the dash line from midway of the channel containing the rib at X=0, through the GDL to pixel location X=45; position b: the solid line from midway of the channel without the rib at X=0, through the GDL to pixel location X=45)

As shown in Figure 4.9, position 'a' represents the region from midway of the channel containing 2 mm width of a rib through GDL. While the line representing

position ‘b’ stretches from midway of the channel without rib through GDL. In Figure 4.10, water thickness below the GDL at position ‘a’ is 4 mm, which is 2 mm less than that below GDL at position ‘b’. This is because the rib below the GDL at position ‘a’ takes up 2 mm thickness in the channel. One also sees that the liquid water thickness profile in the GDL at position ‘a’ is less than that at position ‘b’, illustrating the role of the flow field elements on the local water distribution in the GDL. The region above the ribs is more compressed leading to different morphologic properties and different capillary pressure properties. The region above the channels is less compressed, because the GDL is allowed to protrude into the channels. The protrusion of the GDL into the liquid channel causes the water thickness to drop below 6 mm before the rib/GDL interface. One could determine the depth of the GDL protrusion into the channel by the position at which the water thickness starts to drop below 6 mm. In this study it is roughly 30 μm. The effect of GDL protrusion into the channel was also observed in the reference [58]. From the rib/GDL interface, the water thickness drops gradually to zero half way through the GDL. Similar water distribution trend in the GDL during imbibition was also observed by Büchi [59].

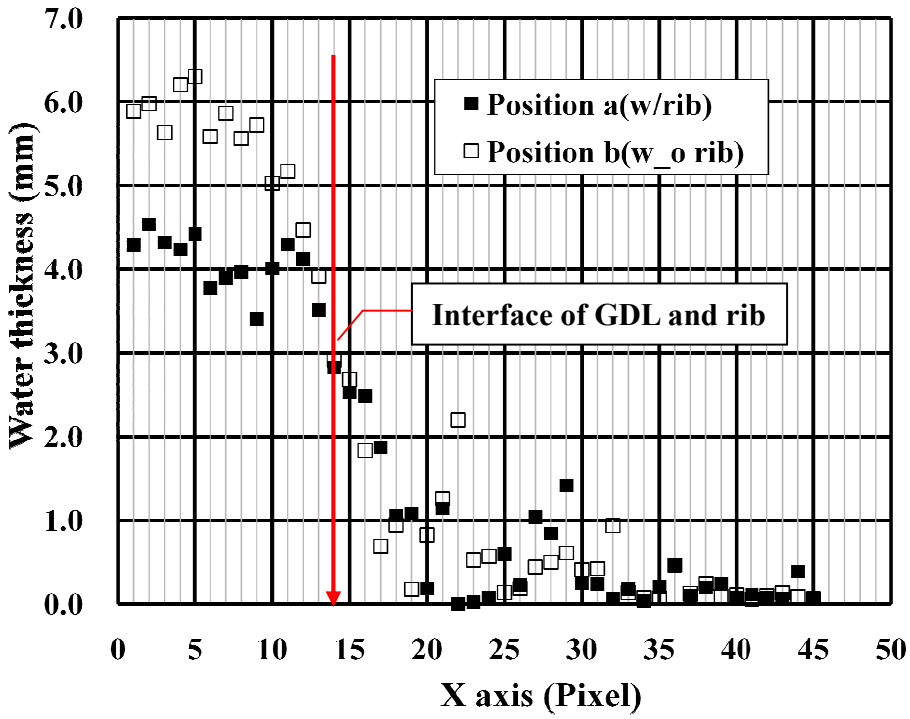

Figure 4.10 Water thickness distribution along through-plane direction for positions 'a' and 'b' before breakthrough at capillary pressure (Position a and b conrresponding to the description shown in Figure 4.9)

After breakthrough point, liquid water thickness all through the GDL through-plane direction increases in both positions comparing with that before breakthrough. At lower capillary pressure, the water retains on one side near the water reservoir. As pressure increases, the liquid water moves to the center of GDL and then out of the opposite side of GDL after the breakthrough point. When reaching the breakthrough point, liquid water tends to retain on both sides of GDL, this can be attributed to the non-uniform porosity distribution along the through-plane direction observed by Büchi [59]. As shown in Figure 4.11, the water thickness in position b on the opposite side reaches as high as 3 mm, corresponding to the saturation level of

60%.

The rib-channel structure does not only cause the pertrusion of GDL into channels, but also have effects on the in-plane water distribution pattern. Since the water distribution decreases gradually along the through-plane direction, when investigating the water distribution along in-plane direction, two different positions ('top' and 'bottom') are chosen, as shown in Figure 4.12.

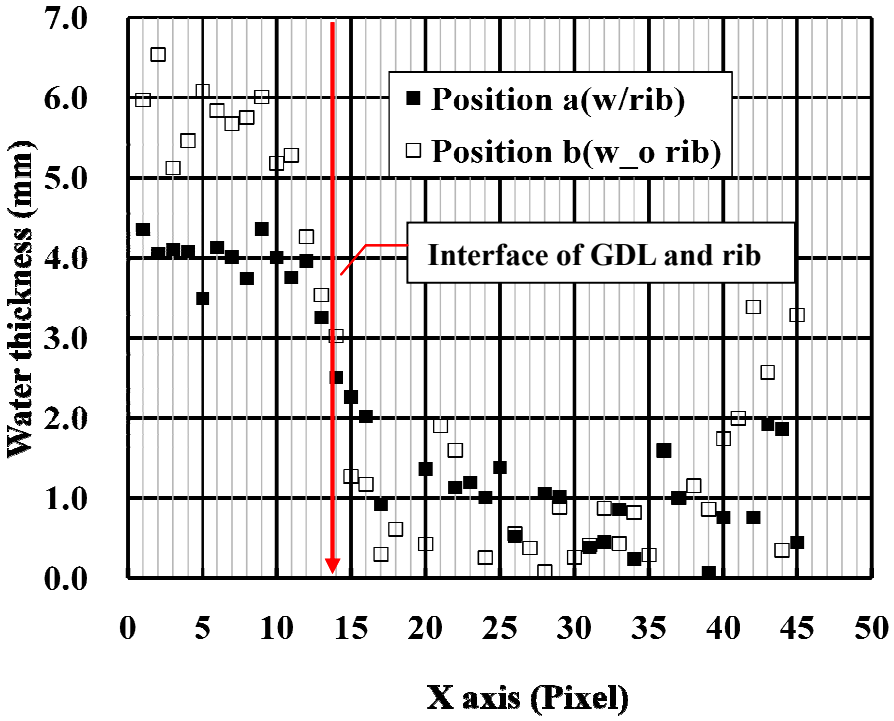

Figure 4.11 Water thickness distribution along through-plane direction for positions 'a' and 'b' after breakthrough

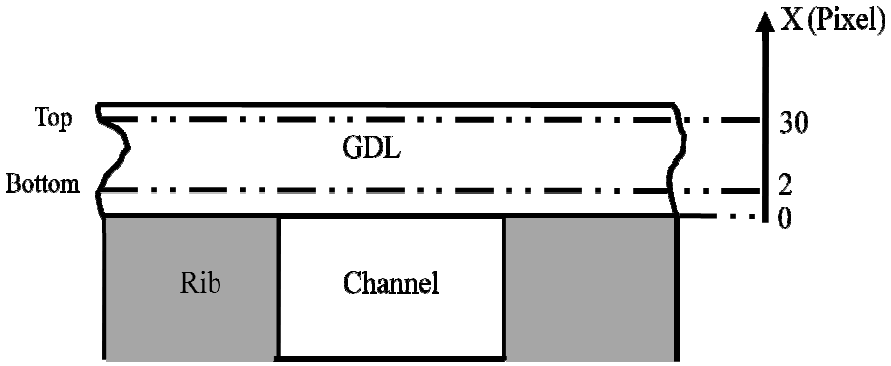

Figure 4.12 A representive diagram of two positions (top and bottom) for investigation of in-plane water distribution pattern in the GDL (top: the dash line across the whole GDL at X=30; bottom: the dash line across the GDL at X=2)

The water thickness along in-plane direction, at capillary pressure 4300 Pa, is shown in Figure 4.13 (a). By comparing the water thickness in two positions, it can be seen that the average value of the bottom position is 4 times larger than that of the top position, this can be used as a validation for the water distribution pattern in the through-plane direction shown in Figure 4.10. It is evident that the water thickness inside the GDL above the ribs is thinner than that above the channels in the bottom position. The average water thickness above the rib is 1.05 mm, and the average value above the channel is 1.66 mm. Such water distribution trend disappears in the top position. It can be deduced that liquid water has not reached the upper region of the GDL at this pressure level.

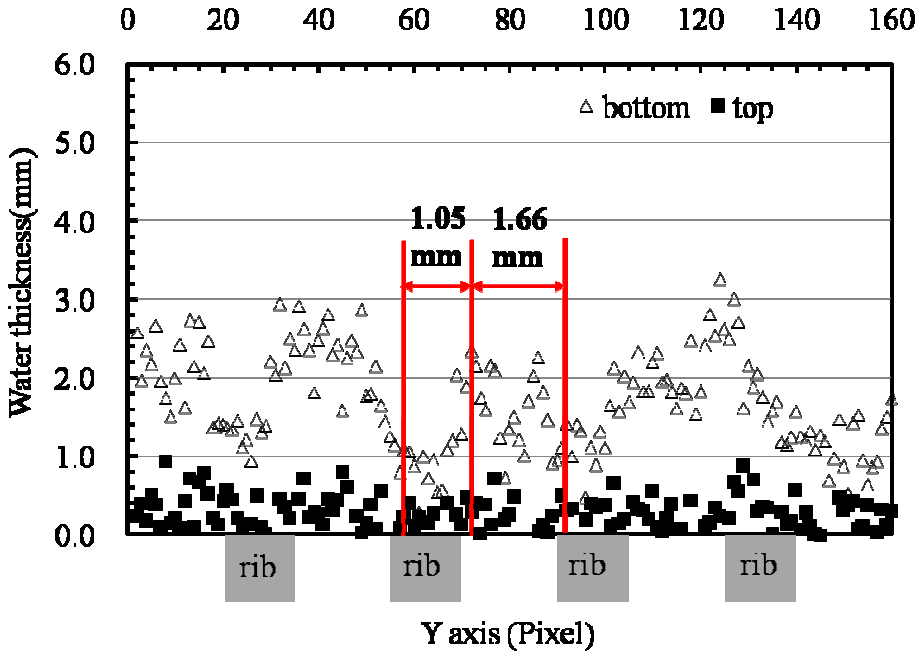

Figure 4.13 (a) water thickness distribution along in-plane direction (before breakthrough, Pc=4300 Pa)

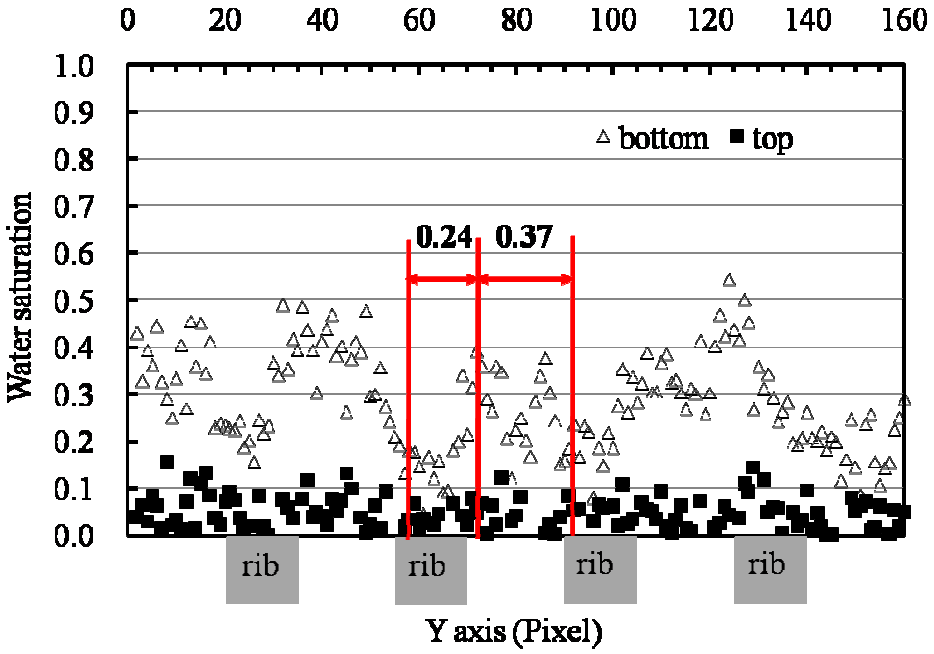

Figure 4.13 (b) water saturation along in-plane direction (before breakthrough, Pc=4300 Pa)

Eq. (4.3) illustrates the relationship between water thickness and liquid water saturation. The water thickness in Figure 4.13 (a) can be converted to water saturation in Figure 4.13 (b).

$$S_w = \frac{t_{water}}{t_{comp} * \varepsilon} \tag{4.3}$$

Where t_{water} is the thickness of water, t_{comp} is the thickness of the compressed GDL sample under the ribs and ε is the porosity. In reality, due to non-uniform compression effects caused by the rib/channel structure, the porosity and the thickness above the rib should be smaller than from that above the channel. Accordingly, the void volume above the channel is larger than that above the rib. In our studies, however, ε and t_{comp} are assumed to be uniform since no data for local porosity and thickness are available. The calculated saturation level above the rib is 0.24, while, the saturation level above the channel is 0.37. The saturation level in channel-channel region is likely to be less than 0.37 in practical condition.

As the capillary pressure increases, the water thickness in both positions increases accordingly. After breakthrough point, in Figure 4.14(a), the water thickness above the channel reaches 2.03 mm at the bottom postion, the value above the rib is as high as 1.65 mm. The avarage liquid water saturation levels in two different positions are 0.46, 0.37 respectively, as shown in Figure 4.14(b). In practical situation, the saturation level between the channels should be lower than the calculated value since the void volume between the channels is larger than that between the ribs.

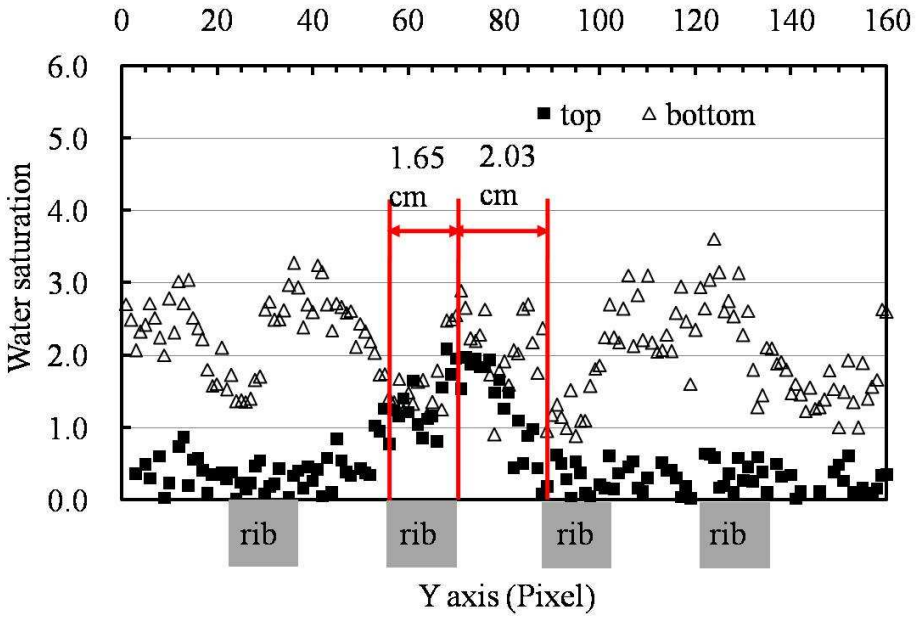

Figure 4.14 (a) water thickness distribution along in-plane direction (after breakthrough, Pc=5400 Pa)

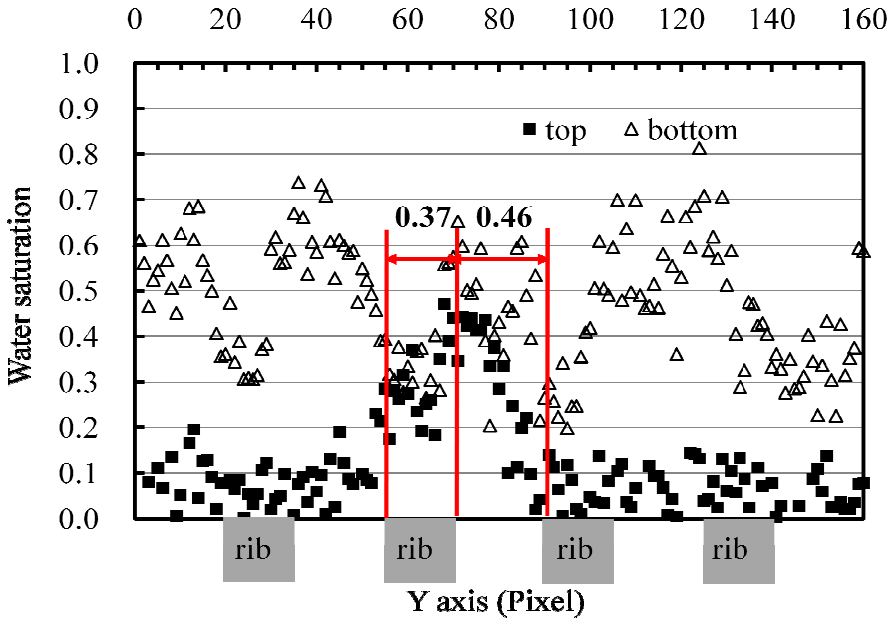

Figure 4.14 (b) water saturation level distribution along in-plane direction (after breakthrough, Pc=5400 Pa)

As seen from the top position in Figure 4.14(b), liquid water breakthrough appears to occur through a pathway above the liquid channel at which the liquid inlet is located. The fact that the breakthrough point occurs above the liquid inlet is not surprising because the region above the liquid inlet experiences the highest pressure exerted by the microfluidic pump. Once a liquid pathway through the GDL is created, the liquid water saturation level in the GDL above this liquid channel drops slightly as the liquid pressure in the GDL is reduced.

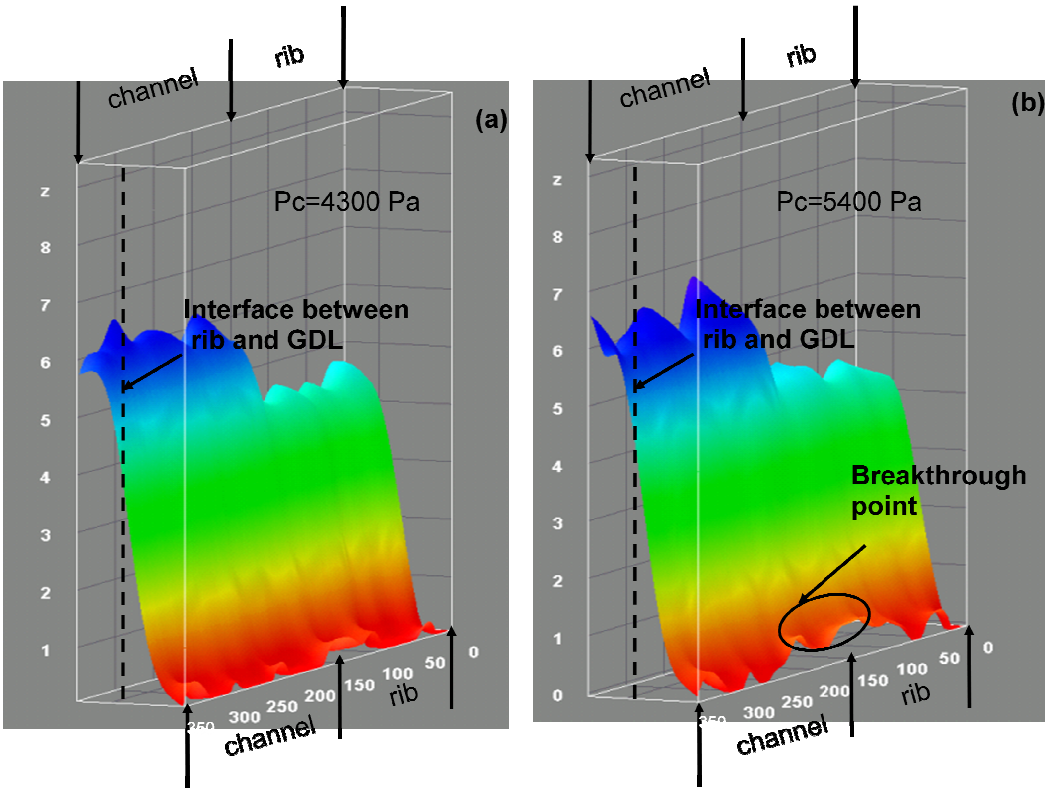

Figure 4.15 Two-dimensional water distributions in the GDL before and after liquid breakthrough (z-axes and color bars are water thickness in mm)

Figure 4.15 shows the 2D liquid water distribution in the region shown in Figure 4.16 right before and after liquid breakthrough from the GDL. By comparing

the water distribution in 2D pattern, the breakthrough point is obvious at capillary pressure 5400 Pa, the position correspond to the right position shown in Figure 4.14. From the interface between GDL and ribs, the water thickness on the interface increases as pressure rises. The gradually decreasing trend is also shown in 2D water thickness distribution.

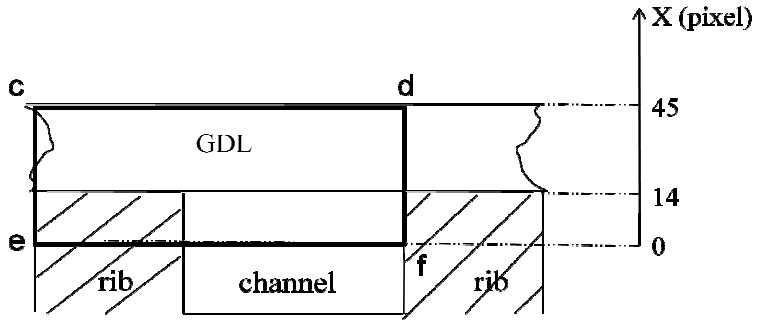

Figure 4.16 Schematic of the region (rectangle c-d-f-e) of the 2D plots in Figure 4.15

4.5 Conclusions

Liquid water distributions in a gas diffusion layer during imbibition and drainage were investigated using neutron imaging. Higher compression between the ribs led to different morphological properties (lower void volume and smaller pore sizes) and, consequently, different transport (capillary pressure and permeability) properties of the GDL in these regions. The results showed that the liquid water level distributions in the GDL in the regions above the ribs were different from those in the regions above the liquid channels. The difference in the liquid saturation level is attributed to the difference in compression of the GDL due to the channel-rib structure of the flow field. In our studies, the void volume based on compressed thickness and porosity was assumed to be the same in both rib-rib and channel-channel regions, the

non-uniform thickness and porosity were not taken into account. Therefore, the liquid saturation level in the channel-channel regions needs to be further confirmed. The results also showed that liquid water breakthrough occurred at a location in the GDL above the liquid channel where liquid water was introduced. Once breakthrough occurred, the liquid pressure dropped, the saturation level in the GDL in the region below the breakthrough point dropped, and liquid water flow through this established pathway was maintained. The effect of non-uniform compression on the GDL morphological and transport properties needs to be taken into consideration in future modeling studies of transport in PEM fuel cells.

CHPATER 5

Future work and recommendations

5.1 Capillary Pressure Measurements for Micro-porous Layer (MPL) in PEM Fuel Cells

Two approaches have been taken to solve water flooding problems in PEM fuel cells. In the first approach, GDLs were treated with hydrophobic fluoropolymer to expel excessive water inside the cell. In the second approach, the MPL was placed between GDL and catalyst layer to improve mass transfer. It helps prevent water generated in catalyst layer from moving through the GDL to the gas channel in cathode side, and creates higher liquid pressure for water to permeate back from the cathode to the anode. Evidently, the addition of MPL will change the two-phase flow pattern in a PEM fuel cell. It is therefore necessary to identify the capillary properties of the MPLs.

Comparing with macro-porous materials used for GDLs, a MPL has a larger amount of PTFE content and smaller pore size. These properties make an MPL more hydrophobic than a GDL. Some researchers have measured the capillary curves for macro-porous media with MPLs by using MSP method [51] or Microfluidic method [60]. No similar work has been done or published using the volume displacement method. Therefore, it is recommended that the volume displacement method be used to

measure the capillary pressure curves for MPLs.

5.2 Expressions of Capillary Curves for Modeling in PEM Fuel Cells

Various curve fittings have been developed from experimental data for capillary pressure measurements. However, none of the fitting curves have been generalized to describe all the GDLs with specific pore size distribution and wettability. Once the generalized expression of capillary curves for GDLs is known, the capillary pressure versus water saturation relationship can be obtained for all porous media with substitution of physical properties of these materials. And the expression can be substituted into simulation models without testing all GDL samples.

Moreover, the results from neutron imaging tell us non-uniform saturation and capillary pressure distributions exist in the porous media because of non-uniform compression created by the geometry of the flow field distributor. This must be taken into consideration when developing the expressions for capillary pressure curves for fuel cell applications.

REFRENCES

1. R. O'Hayre, S. W. Cha, F. B. Prinz. Fuel cell fundamentals. New Jersey: John Wiley & Sons; 2005.
2. G. Crawley. Proton exchange membrane (PEM) fuel cells. Fuel Cell Today, 2006.
3. A. R. George. Status of tubular SOFC field unit demonstrations. J. Power Sources. 2000;86(1-2):134-139.
4. D. L. Wood, J. S. Yi, T. V. Nguyen. Effect of direct liquid water injection and interdigitated flow field on the performance of proton exchange membrane fuel cells. Electrochimica Acta. 1998;43(24): 3795-3809.
5. H. Li, Y. Tang, Z. Wang, Z. Shi, S. Wu, D. Song, J. Zhang. A review of water flooding issues in the proton exchange membrane fuel cell. Journal of Power Sources. 2008;178(1):103-117.
6. M. M. Mench. Fuel Cell Engines. New Jersy: John Wiley and Sons; 2008.
7. M. Mathias, J. Roth, J. Fleming, W. Lehnert. Diffusion media materials and characterisation. In: W. Vielstich, A. Lamm, ed. Handbook of Fuel Cells–Fundamentals, Technology and Applications. Vol 3. New Jersy: John Wiley & Sons; 2003.
8. G. Lin, W.He, T. V. Nguyen. Modeling liquid water effects in gas diffusion and catalyst layers of a PEM fuel cell electrode. Journal of the Electrochemical Society. 2004;151(12):A1999-A2006.
9. H. Ohn. Measurement of capillary pressure properties of gas diffusion materials used in proton exchange membrane fuel cells. Lawrence: Chemical & Petroleum Engineering, University of Kansas; 2007.
10. E. C. Kumbur, K. V. Sharp, M. M. Mench. Validated leverett approach for multiphase flow in PEFC diffusion media. II. compression effect. Journal of the Electrochemical Society. 2007;154(12):B1305-B1314.
11. J. Benziger, J. Nehlsen, D. Blackwell, T. Brennan, J. Itescu. Water flow in the gas diffusion layer of PEM fuel cells. Journal of Membrane Science. 2005;261(1-2):98-106.
12. L. Cindrella, A.M. Kannana, J.F. Lina, K. Saminathana, Y. Hoc, C.W. Lind, J. Wertze. Gas diffusion layer for proton exchange membrane fuel cells-A review. Journal of Power Sources. 2009;194(1):146-160.
13. M. Han, J.H. Xua, S.H. Chan, S.P. Jiang. Characterization of gas diffusion layers for PEMFC. Electrochimica Acta. 2008;53(16): 5361- 5367.
14. M. J. Martínez, S. Shimpalee, J. W. Van Zee, A. V. Sakars. Assessing methods and data for pore-size distribution of PEMFC gas-diffusion media. Journal of The Electrochemical Society. 2009;156(5): B558- B564.

15. Y. M. Volfkovich, V.S. Bagotzky, V.E. Sosenkin, I.A. Blinov. The standard contact porosimetry. Colloids and Surfaces A: Physicochemical and Engineering Aspects. 2001; 187-188:349-365.
16. Z. Zhan, J. Xiao, D. Li, M. Pana, R. Yuan. Effects of porosity distribution variation on the liquid water flux through gas diffusion layers of PEM fuel cells. Journal of Power Sources. 2006;160(2):1041-1048.
17. H. Chu, C. Yeh, F. Chen. Effects of porosity change of gas diffuser on performance of proton exchange membrane fuel cell. Journal of Power Sources. 2003;123(1):1-9.
18. C. Lim, C.Y. Wang. Effects of hydrophobic polymer content in GDL on power performance of a PEM fuel cell. Electrochimica Acta. 2004; 49 (24):4149-4156.
19. S. Park, J. Lee, B. N. Popov. Effect of PTFE content in microporous layer on water management in PEM fuel cells. Journal of Power Sources. 2008; 177(2):457-463.
20. A. Bazylak, D.Sinton, Z. Liu, N. Djilali. Effect of compression on liquid water transport and microstructure of PEMFC gas diffusion layers. Journal of Power Sources. 2007;163:784-792.
21. W.R. Chang, J.J. Hwang, F.B. Weng, S.H. Chan. Effect of clamping pressure on the performance of a PEM fuel cell. Journal of Power Sources. 2007; 166(1):149-154.
22. W. Lee, C. Ho, J.W. Van Zee, M. Murthy. The Effects of compression and gas diffusion layers on the performance of a PEM fuel cell. Journal of Power Sources 1999;84(1):45-51.
23. I. Nitta, S. Karvonen,O. Himanen, M. Mikkola. Modelling the effect of inhomogeneous compression of GDL on local transport phenomena in a PEM fuel cell. Fuel Cells. 2006;8(6):410-421.
24. P. Zhou, C.W. Wu. Numerical study on the compression effect of gas diffusion layer on PEMFC performance. Journal of Power Sources 2007; 170(1):93-100.
25. I.R. Harkness, N. Hussain, L. Smitha, J.D.B. Sharman. The use of a novel water porosimeter to predict the water handling behaviour of gas diffusion media used in polymer electrolyte fuel cells. Journal of Power Sources. 2009;193(1):122-129..
26. J. T. Gostick, M. A. Ioannidis, M. W. Fowler, M. D. Pritzker. Direct measurement of the capillary pressure characteristics of water-air-gas diffusion layer systems for PEM fuel cells. Electrochemistry Communications. 2008;10(10):1520-1523.
27. J. T. Gostick, M. W. Fowler, M. A. Ioannidis, M. D. Pritzker, Y.M.

Volfkovich, A. Sakars. Capillary pressure and hydrophilic porosity in gas diffusion layers for polymer electrolyte fuel cells. Journal of Power Sources. 2006;156(2):375-387.
28. E.C. Kumbur, K.V. Sharp, M.M. Mench. On the effectiveness of leverett approach for describing the water transport in fuel cell diffusion media. Journal of Power Sources. 2007;168(2):356-368.
29. K. G. Gallagher, R. M. Darling, T. W. Patterson, M. L. Perry. Capillary pressure saturation relations for PEM fuel cell gas diffusion layers. Journal of The Electrochemical Society. 2008;155(11):B1225-B1231.
30. J. D. Fairweather, P. Cheung, J. St-Pierreb, D. T. Schwartz. A microfluidic approach for measuring capillary pressure in PEMFC gas diffusion layers. Electrochemistry Communications. 2007;9(9): 2340-2345.
31. P. Cheung, J. D. Fairweather, D. T. Schwartz. Characterization of internal wetting in polymer electrolyte membrane gas diffusion layers. Journal of Power Sources. 2009;187(2):487-492.
32. J. D. Fairweather, P. Cheung, J. St-Pierreb, D. T. Schwartz. The effects of wetproofing on the capillary properties of proton exchange membrane fuel cell gas diffusion layers. Journal of Power Sources. 2010;195(3):787-793.
33. T. V. Nguyen, G. Lin, H. Ohn, X. Wang. Measurement of capillary pressure property of gas diffusion media used in proton exchange membrane fuel cells. Electrochemical Solid-State Letters. 2008; 11(8): B127-B131.
34. A. Bazylak. Liquid water visualization in PEM fuel cells: A review. International Journal of Hydrogen Energy. 2009;34(9):3845-3857.
35. N. Pekula, K. Heller, P. Chuang. Study of water distribution and transport in a polymer electrolyte fuel cell using neutron imaging. Nuclear Instruments and Methods in Physics Research A. 2005;542(1): 134-141.
36. R. Satija, D.L. Jacobson, M. Arif, S.A. Werner. In situ neutron imaging technique for evaluation of water management systems in operating PEM fuel cells. Journal of Power Sources. 2004;129(2):238-245.
37. D.S.Hussey, D.L.Jacobson. Neutron images of the through-plane water distribution of an operating PEM fuel cell. Journal of Power Sources. 2007;172(1):225-228.
38. Z. Zhan, J. Xiao, Y. Zhang, M. Pan, R. Yuan. Gas diffusion through differently structured gas diffusion layers of PEM fuel cells. International Journal of Hydrogen Energy. 2007;32(17):4443-4451.
39. S. Park, B. Popov. Effect of hydrophobicity and pore geometry in cathode GDL on PEM fuel cell performance. Electrochimica Acta. 2009;54(12): 3473-3479.
40. J. Lobato, P. Canizares, M. A. Rodrigo, C. Ruiz-López , J. J. Linares.

Influence of the Teflon loading in the gas diffusion layer of PBI-based PEM fuel cells. Journal of Applied Electrochemistry. 2008;38(6): 793-802.
41. S.Y. Lee, K. Lee, S. Um. The structural variation of the gas diffusion layer and a performance evaluation of polymer electrolyte fuel cells as a function of clamping pressure. Journal of Mechanical Science and Technology 2008; 22:565-574.
42. A. Pozio, A. Cemmi, M. Carewska, C. Paoletti, F. Zaza. Characterization of gas diffusion electrodes for polymer electrolyte fuel cells. Journal of Fuel Cell Science and Technology. 2010;7(4):1-7.
43. M. V. Williams, E. Begg, L. Bonville, H. R. Kunz, J. M. Fentona. Characterization of gas diffusion layers for PEMFC. Journal of The Electrochemical Society. 2004;151(8):A1173-A1180.
44. Toray Composites (America), Inc. 2010< http://www.toray-auto.us/products/ carbon_papers_fuel_cells.html>.
45. W. He, J. S. Yi, T. V. Nguyen. Two-phase flow model of the cathode of PEM fuel cells using interdigitated flow fields. AIChE Journal. 2000;46(10): 2053–2064.
46. Z. Liu, H. Zhang, C. Wang, Z. Mao. Numerical simulation for rib and channel position effect on PEMFC performances. International Journal of Hydrogen Energy. 2010;35(7):2802-2806.
47. K.Tüber, D. Pócza, C. Hebling. Visualization of water buildup in the cathode of a transparent PEM fuel cell. Journal of Power Sources. 2003;124(2): 403-414.
48. S. Ge, C. Wang. Liquid water formation and transport in the PEFC anode. Journal of The Electrochemical Society. 2007;154(10):B998-B1005.
49. J. T. Gostick, M. A. Ioannidis, M. W. Fowler, M. D. Pritzker. Wettability and capillary behavior of fibrous gas diffusion media for polymer electrolyte membrane fuel cells. Journal of Power Sources. 2009;194(1):433–444.
50. E. C. Kumbur, K. V. Sharp, M. M. Mench. Validated leverett approach for multiphase flow in PEFC diffusion media I. Hydrophobicity effect. Journal of The Electrochemical Society. 2007;154(12):B1295-B1304.
51. J. Lobato, P. Cañizares, M. A. Rodrigo, J. J. Linares. Testing a vapour-fed PBI-based direct ethanol fuel cell. Fuel Cells. 2009;9(5): 597–604.
52. J. T.Gostick. Multiphase Mass Transfer and Capillary Properties of Gas Diffusion Layers for Polymer Electrolyte Membrane Fuel Cells. Waterloo: Chemical Engineering, University of Waterloo; 2008.
53. R. Fluckiger, S.A. Freunberger, D.Kramer, A. Wokaun, , G.G. Scherer, F.N. Buchi. Anisotropic, effective diffusivity of porous gas diffusion layer materials for PEFC. Electrochimica Acta. 2008;54(2):551-559.

54. C. Wang. Fundamental models for fuel cell engineering. Chemical Reviews. 2004;104(10):4727-4766.
55. J. St-Pierre. PEMFC In situ liquid-water-content monitoring status. Journal of Electrochemical Society. 2007;154(7):B724-B731.
56. A. K. Heller. A neutron radioscopic water quantification technique for PEM fuel cell water distribution studies. Philadelphia Nuclear Engineering, The Pennsylvania State University; 2007.
57. Y. Chen, H. Peng, D. S. Hussey, D. L. Jacobson, D. T. Tran. Water distribution measurement for a PEMFC through neutron radiography. Journal of Power Sources. 2007;170(2):376-386.
58. I. Nitta, T. Hottinen, O. Himanen, M. Mikkola. Inhomogeneous compression of PEMFC gas diffusion layer: Part I. Experimental. Journal of Power Sources. 2007;171(1):26-36.
59. F. N. Büchi, R. Flückiger, D. Tehlar. Determination of Liquid Water Distribution in Porous Transport Layers. ECS Transaction. 2008;16(2): 587-592.
60. J. T. Gostick, M. A. Ioannidis, M. W. Fowler, M. D. Pritzker. On the Role of the Microporous Layer in PEMFC Operation. Electrochemistry Communications. 2009; 11(3): 576-579.

Appendix A

Raw Data of Volume Displacement Measurements for Toray TGP-H-060 and Toray TGP-H-090

Table A.1 Raw data for Toray TGP-H-060 used in configuration 1 (H: height of horizontal tube; time: duration time for each scan (min); P: pressure (cmH2O); V: volume (corrected with evaporation rate)(cm3); S: saturation)

Toray TGP-H-060, 10 wt % wetproof				Toray TGP-H-060, 20 wt % wetproof				Toray TGP-H-060, 30 wt % wetproof			
H	T	P	V	H	T	P	V	H	T	P	V
57.0	15	2.19	0.693	58.0	10	-0.23	0.462	57.5	0	-1.73	0.238
57.5	11	2.56	0.726	59.0	15	0.45	0.467	58.0	13	-0.90	0.243
58.0	11	3.30	0.874	59.5	11	1.05	0.632	58.5	10	-0.70	0.281
58.5	76	3.30	1.182	60.0	20	1.20	0.693	59.0	15	-0.07	0.322
59.1	35	4.34	1.540	60.5	20	1.50	0.862	59.5	10	0.22	0.346
59.5	14	4.57	1.548	61.0	10	2.17	0.864	60.0	103	0.75	0.662
60.0	11	5.23	1.549	62.0	16	3.15	0.867	60.5	11	1.20	0.664
61.0	13	5.90	1.555	63.0	10	4.19	0.874	61.0	10	1.65	0.665
62.0	15	7.09	1.564	64.0	10	5.09	0.876	62.0	10	2.85	0.670
63.0	12	7.90	1.568	65.0	10	6.14	0.884	63.0	18	3.76	0.671
64.0	11	9.02	1.573	67.0	11	8.17	0.890	65.0	10	5.69	0.676
65.0	10	10.80	1.581	70.0	10	11.17	0.896	67.0	10	7.72	0.684
66.0	10	11.17	1.584	72.0	10	13.25	0.899	68.0	13	8.77	0.690
67.0	10	12.29	1.592	74.0	14	15.14	0.900	70.0	15	10.64	0.696
70.0	10	15.33	1.596	75.0	10	16.12	0.904	72.0	12	12.74	0.701
72.0	12	17.34	1.599	72.0	10	13.27	0.900	74.0	10	14.69	0.703
70.0	10	15.55	1.597	70.0	8	11.02	0.892	75.0	10	15.70	0.703
67.0	8	12.54	1.595	67.0	10	8.15	0.886	80.0	22	20.99	0.705
65.0	10	10.51	1.590	65.0	10	6.24	0.884	77.0	15	17.92	0.703
64.0	10	9.17	1.587	63.0	10	4.34	0.883	75.0	10	16.04	0.703
63.0	14	8.57	1.585	61.0	10	2.32	0.882	72.0	10	12.97	0.702
62.0	8	7.83	1.580	59.0	10	0.37	0.881	70.0	10	10.94	0.699
61.0	10	6.32	1.578	57.0	10	-1.80	0.880	68.0	10	8.92	0.693
60.0	10	5.53	1.577	59.0	10	0.15	0.881	66.0	12	7.34	0.688
59.0	8	4.27	1.576	61.0	15	2.21	0.882	64.0	17	4.79	0.686
58.0	10	3.23	1.575	64.0	7	5.02	0.884	61.0	10	1.80	0.683

57.0	12	2.56	1.574	67.0	8	8.17	0.889	59.0	10	-0.15	0.681
58.0	10	3.67	1.575	70.0	7	11.12	0.894	57.0	10	-1.95	0.679
59.0	10	4.27	1.576	72.0	10	13.27	0.897	59.0	10	-0.30	0.680
60.0	10	5.39	1.577	75.0	7	16.12	0.901	60.0	10	0.37	0.681
61.0	7	6.20	1.579	72.0	6	13.19	0.896	61.0	6	1.47	0.683
62.0	11	7.24	1.580	70.0	6	11.39	0.895	63.0	5	3.37	0.685
63.0	10	8.35	1.581	67.0	8	8.24	0.887	65.0	5	5.45	0.688
64.0	10	8.80	1.586	65.0	6	6.37	0.886	67.0	30	7.44	0.691
65.0	10	9.84	1.588	62.0	8	3.37	0.885	70.0	5	10.72	0.700
66.0	13	11.10	1.590	60.0	7	1.65	0.884	72.0	7	12.89	0.701
67.0	10	12.14	1.593	57.0	5	-1.27	0.882	75.0	6	15.74	0.703
70.0	10	15.18	1.600	60.0	7	1.65	0.885	72.0	5	12.74	0.702
72.0	10	17.04	1.601	63.0	7	4.42	0.886	70.0	5	11.24	0.700
70.0	8	15.26	1.599	67.0	7	8.24	0.888	68.0	7	9.14	0.697
67.0	10	12.36	1.598	70.0	4	11.17	0.894	67.0	7	8.17	0.694
65.0	12	10.64	1.595	75.0	5	16.12	0.904	66.0	5	7.13	0.688
64.0	15	9.24	1.588	80.0	5	21.14	0.908	64.0	11	5.17	0.687
63.0	10	8.43	1.587	85.0	5	26.12	0.913	62.0	10	3.15	0.684
61.0	10	6.72	1.581	90.0	8	31.41	0.916	60.0	6	1.12	0.682
59.0	10	4.42	1.579	95.0	5	36.42	0.919	57.0	6	-1.95	0.679
57.0	10	2.11	1.577	100.0	11	41.69	0.922	60.0	5	0.37	0.680
59.0	10	4.05	1.578	102.0	5	42.51	0.934	62.0	5	2.55	0.683
61.0	10	6.20	1.580					65.0	5	5.62	0.685
63.0	10	7.91	1.582					70.0	5	10.64	0.699
65.0	11	10.06	1.592					75.0	5	15.59	0.703
67.0	10	11.99	1.598					80.0	5	20.62	0.706
70.0	10	15.11	1.602					90.0	5	31.24	0.708
75.0	10	20.45	1.607					95.0	5	36.74	0.709
80.0	14	25.43	1.611					100.0	5	41.31	0.711
85.0	10	30.26	1.618					105.0	5	44.29	0.711
87.0	8	32.48	1.619					105.0	5	44.32	0.719
90.0	10	35.53	1.621								
92.0	10	37.61	1.622								
95.0	10	40.50	1.625								
98.0	10	43.33	1.626								
100.0	13	45.26	1.628								
103.0	1	47.12	1.629								

103.0	5	47.41	1.643								

Table A.2 Raw Data for Toray TGP-H-090, 20 wt% wetproof used in configuration 1

Thickness 275 μm				Thickness 225 μm				Thickness 200 μm			
H	T	P	V	H	T	P	V	H	T	P	V
58.0	1	2.26	0.998	58.0	2	2.26	1.474	58.0	5	1.263	0.196
58.5	4	2.04	1.069	58.5	21	2.41	1.567	58.5	10	1.717	0.319
59.0	20	2.41	1.179	59.1	10	2.71	1.658	59.1	5	2.329	0.325
59.3	11	2.93	1.180	59.5	11	3.15	1.659	60.0	10	3.154	0.328
59.5	10	2.93	1.181	60.0	13	3.90	1.661	60.5	11	3.896	0.329
59.9	9	3.30	1.183	60.5	10	4.57	1.662	61.5	8	4.565	0.331
60.3	10	3.67	1.185	61.0	6	4.86	1.664	62.0	15	4.862	0.333
60.6	10	4.12	1.186	61.5	12	5.31	1.665	62.5	10	5.307	0.334
61.0	10	4.79	1.187	62.0	20	5.83	1.668	63.0	10	5.827	0.339
61.3	11	4.79	1.189	63.0	6	6.79	1.670	64.0	10	6.792	0.345
61.5	9	5.16	1.190	63.5	12	7.02	1.673	64.5	10	7.015	0.348
62.1	23	5.75	1.193	64.5	10	8.58	1.676	66.0	12	8.575	0.352
62.5	13	5.90	1.195	65.0	12	8.72	1.678	66.5	10	8.723	0.357
63.0	9	6.49	1.198	65.4	10	9.17	1.680	67.0	10	9.169	0.358
63.5	19	6.94	1.202	66.0	10	9.69	1.683	67.5	10	9.688	0.358
64.0	24	7.54	1.211	67.0	10	11.03	1.688	69.0	10	11.025	0.360
64.3	23	7.83	1.214	68.0	13	11.84	1.690	69.5	10	11.842	0.364
64.5	13	8.06	1.215	69.0	10	12.73	1.693	70.5	11	12.733	0.366
65.0	23	8.87	1.230	70.0	15	13.96	1.695	71.5	13	13.955	0.368
65.3	11	9.02	1.233	72.0	10	16.38	1.700	74.0	10	16.375	0.370
65.5	11	9.32	1.235	72.0	14	16.45	1.703	72.0	10	14.067	0.366
66.0	18	9.61	1.237	70.0	10	14.52	1.700	71.0	10	13.136	0.365
67.0	27	10.73	1.242	68.0	6	12.74	1.699	70.0	8	11.889	0.363
68.0	11	11.92	1.245	67.0	10	11.77	1.697	67.5	8	9.409	0.360
69.5	12	13.18	1.250	65.0	13	9.69	1.695	65.5	10	7.379	0.356
71.0	10	14.22	1.253	63.3	10	7.76	1.689	64.5	11	6.265	0.353
72.0	11	15.33	1.255	62.0	10	6.64	1.687	62.0	6	4.928	0.350
71.0	14	15.03	1.255	61.0	16	5.31	1.684	61.0	10	3.74	0.349
69.5	12	13.62	1.254	59.9	11	4.12	1.683	60.0	8	2.858	0.347
68.0	7	12.51	1.254	59.0	21	3.34	1.682	59.0	10	1.781	0.345
67.0	12	11.10	1.253	58.2	10	2.56	1.681	58.0	11	0.796	0.345
66.0	10	10.13	1.250	57.5	10	1.89	1.680	60.0	10	2.901	0.349
65.0	11	9.39	1.248	57.0	8	1.08	1.680	62.0	10	4.705	0.352
64.0	9	7.91	1.244	58.0	14	1.59	1.680	64.0	12	6.513	0.356

63.0	10	7.02	1.241	59.0	8	3.08	1.682	66.0	8	8.567	0.359
62.0	10	6.12	1.237	59.9	10	3.82	1.683	67.0	10	9.489	0.360
61.0	19	5.53	1.230	61.0	10	5.08	1.686	69.0	10	11.502	0.366
60.0	13	4.49	1.224	62.0	10	5.83	1.687	72.0	10	14.359	0.375
59.5	8	4.12	1.224	63.0	12	6.79	1.689	75.0	10	17.586	0.380
59.0	8	3.53	1.218	64.1	5	7.76	1.692	72.5	10	15.007	0.373
58.5	11	2.78	1.217	65.0	10	8.95	1.695	70.5	13	13.245	0.369
57.5	8	2.04	1.216	66.0	11	9.87	1.699	68.5	9	11.346	0.365
57.0	5	1.59	1.215	67.5	6	11.62	1.701	66.5	11	9.385	0.361
58.0	8	1.82	1.216	69.0	8	12.88	1.702	64.0	8	6.899	0.358
59.0	8	2.49	1.218	71.0	6	14.74	1.705	63.0	10	5.265	0.355
60.0	12	3.60	1.220	73.0	5	16.97	1.709	61.0	11	3.334	0.352
61.0	10	4.42	1.221	71.0	5	15.48	1.707	60.0	11	2.35	0.348
62.0	8	5.31	1.224	69.0	5	13.62	1.704	58.0	10	0.661	0.347
63.0	12	6.42	1.233	67.0	5	11.84	1.703	57.5	7	0.364	0.347
64.0	14	7.68	1.244	65.0	10	9.76	1.700	58.0	10	0.884	0.348
65.0	11	8.87	1.249	63.5	7	8.28	1.694	60.0	8	2.923	0.352
66.0	9	9.84	1.252	62.0	6	6.64	1.691	62.0	6	4.983	0.354
67.0	9	10.51	1.255	60.0	7	4.71	1.688	64.0	8	6.962	0.358
68.0	10	11.99	1.258	59.0	10	3.23	1.686	66.0	5	8.938	0.360
70.0	8	14.22	1.262	58.0	12	2.04	1.685	68.0	10	11.017	0.365
72.0	9	15.78	1.264	57.0	10	1.74	1.685	70.0	5	13.433	0.370
74.0	19	17.78	1.268	58.0	10	2.26	1.685	75.0	5	18.814	0.378
72.0	9	16.15	1.268	59.5	8	3.30	1.687	80.0	5	23.364	0.383
70.0	5	14.66	1.266	61.0	10	4.86	1.689	85.0	8	29.839	0.387
68.0	6	12.36	1.263	63.0	6	6.94	1.693	90.0	15	34.962	0.388
66.0	22	10.36	1.260	65.0	8	9.32	1.700	95.0	5	40.091	0.390
64.0	9	8.28	1.254	67.0	5	11.40	1.704	100.0	10	45.215	0.391
62.0	12	6.50	1.244	71.0	8	14.81	1.708	110.0	7	54.086	0.393
60.0	9	4.19	1.233	75.0	5	19.19	1.715	115.0	5	57.135	0.406
59.0	6	3.60	1.232	80.0	10	24.24	1.723				
58.0	7	2.04	1.224	85.0	5	29.22	1.728				
57.0	6	1.96	1.223	90.0	10	34.34	1.731				
59.0	11	3.01	1.225	97.0	10	41.47	1.735				
61.0	9	4.94	1.229	102.0	8	46.59	1.738				
63.0	14	6.42	1.238	110.0	8	54.47	1.742				
65.0	6	8.87	1.254	115.0	5	59.51	1.755				

67.0	4	10.80	1.261								
70.0	5	14.07	1.267								
73.0	6	16.97	1.271								
77.0	7	21.12	1.276								
82.0	8	25.73	1.283								
87.0	5	31.08	1.292								
92.0	5	36.20	1.296								
97.0	5	41.25	1.299								
101.0	10	45.33	1.301								
104.0	5	48.01	1.303								
107.0	10	51.12	1.306								
110.0	11	54.02	1.309								
112.0	10	58.25	1.310								
114.0	2	60.18	1.321								

Table A.3 Raw Data for Toray TGP-H-090, 20 wt% wetproof used in configuration 2

Thickness 275 μm				Thickness 225 μm				Thickness 200 μm			
H	T	P	V	H	T	P	V	H	T	P	V
58.5	10	2.24	0.117	58.0	10	2.85	0.677	57.5	11	2.56	0.867
59.2	12	2.85	0.126	58.5	5	2.92	0.679	58.0	11	3.30	0.875
59.7	23	3.30	0.130	59.5	10	4.27	0.680	58.5	76	3.30	0.881
60.5	10	4.23	0.132	60.0	10	4.78	0.686	59.1	35	4.34	0.887
61.5	10	5.32	0.134	60.5	15	5.57	0.696	59.5	14	4.57	0.892
62.0	10	5.84	0.138	61.0	10	6.07	0.696	60.0	11	5.23	0.893
63.0	10	6.74	0.143	62.0	10	7.09	0.696	61.0	13	5.90	0.893
65.0	10	8.84	0.151	63.0	18	7.94	0.697	62.0	15	7.09	0.894
67.0	12	10.94	0.156	65.0	12	8.72	0.698	63.0	12	7.90	0.894
70.0	10	14.09	0.159	67.0	30	11.03	0.702	64.0	11	9.02	0.895
72.0	15	16.27	0.161	70.0	13	13.96	0.712	65.0	10	10.80	0.897
70.0	7	14.17	0.160	72.0	10	16.38	0.716	67.0	10	12.29	0.901
67.0	10	11.24	0.158	74.0	10	18.15	0.718	70.0	10	15.33	0.907
65.0	15	8.99	0.154	72.0	15	16.45	0.717	72.0	12	17.34	0.909
63.0	20	7.19	0.148	70.0	10	14.52	0.716	70.0	10	15.55	0.908
61.0	10	5.24	0.139	67.0	10	11.77	0.712	67.0	8	12.54	0.907
59.0	30	3.30	0.136	65.0	13	9.69	0.710	65.0	10	10.51	0.904
57.0	20	1.27	0.133	62.0	10	5.31	0.710	64.0	10	9.17	0.904
59.0	5	2.62	0.135	61.0	5	4.12	0.709	63.0	5	8.57	0.903
61.0	5	4.87	0.139	59.0	5	3.34	0.709	62.0	8	7.83	0.903
63.0	5	6.89	0.147	61.0	10	5.08	0.709	60.0	5	5.53	0.903
65.0	5	9.07	0.155	62.0	10	5.83	0.709	59.0	8	4.27	0.902
67.0	5	11.02	0.159	63.0	12	6.79	0.710	58.0	10	3.23	0.902
70.0	5	14.24	0.161	65.0	10	8.95	0.711	57.0	12	2.56	0.903
72.0	5	16.27	0.162	67.5	16	11.62	0.712	59.0	10	4.27	0.903
67.0	10	11.47	0.161	69.0	8	12.88	0.715	61.0	7	6.20	0.904
65.0	10	9.52	0.156	71.0	6	14.74	0.717	63.0	10	8.35	0.905
63.0	13	7.49	0.149	73.0	8	16.97	0.719	65.0	10	9.84	0.905
60.5	4	5.02	0.141	71.0	5	15.48	0.718	67.0	10	12.14	0.907
60.0	6	4.42	0.137	69.0	5	13.62	0.717	70.0	10	15.18	0.909
57.0	7	1.35	0.133	67.0	5	11.84	0.714	72.0	10	17.04	0.910
60.0	5	4.05	0.136	65.0	10	9.76	0.712	70.0	8	15.26	0.909
63.0	10	7.04	0.145	63.5	7	8.28	0.711	67.0	10	12.36	0.908
65.0	5	9.21	0.154	62.0	8	6.64	0.710	65.0	12	10.64	0.906

67.0	5	11.24	0.159	60.0	7	4.71	0.709	64.0	15	9.24	0.905
70.0	15	14.32	0.162	59.0	10	3.23	0.709	63.0	10	8.43	0.904
75.0	10	19.34	0.164	57.0	10	1.74	0.708	61.0	10	6.72	0.903
80.0	5	24.44	0.166	59.5	8	3.30	0.709	59.0	10	4.42	0.903
85.0	10	29.61	0.168	61.0	10	4.86	0.709	57.0	10	2.11	0.902
90.0	10	34.67	0.169	63.0	7	6.94	0.710	59.0	10	4.05	0.903
95.0	10	39.51	0.171	65.0	8	9.32	0.712	61.0	10	6.20	0.904
100.0	5	45.13	0.173	67.0	5	11.40	0.715	63.0	10	7.91	0.904
100.0	3	45.01	0.181	71.0	8	14.81	0.717	65.0	11	10.06	0.906
				75.0	5	19.19	0.720	67.0	10	11.99	0.908
				80.0	10	24.24	0.721	70.0	10	15.11	0.909
				85.0	5	29.22	0.722	75.0	10	20.45	0.910
				90.0	10	34.34	0.723	80.0	14	25.43	0.910
				97.0	10	41.47	0.726	85.0	10	30.26	0.911
				102.0	7	46.59	0.727	90.0	10	35.53	0.912
				110.0	8	54.47	0.730	95.0	10	40.50	0.913
				115.0	5	54.57	0.742	98.0	10	43.33	0.913
								100.0	13	45.26	0.913
								103.0	5	47.12	0.914
								107.0	5	51.41	0.915
								110.0	5	54.58	0.916
								110.0	3	54.80	0.944

Appendix B

Experimental Data of Capillary Pressure Measurements

Table B.1 Experimental data for Figure 3.7 (Toray TGP-H-060, 10wt% wetproof) (P_c: capillary pressure (Pa); S: saturation)

Curve 1		Curve 2		Curve 3		Curve 4	
Pc	S	Pc	S	Pc	S	Pc	S
676.66	0.600	1752.5	0.657	1277.1	0.440	1373.8	0.348
530.54	0.596	1492.6	0.650	1098.9	0.422	1180.7	0.324
420.71	0.592	1269.8	0.643	797.3	0.406	1002.9	0.312
252.03	0.585	1084.2	0.639	594.0	0.364	906.0	0.300
130.43	0.570	980.2	0.635	460.3	0.335	698.0	0.284
78.45	0.560	891.1	0.628	400.9	0.315	505.0	0.239
30.40	0.545	802.0	0.618	326.7	0.274	393.6	0.221
-1.96	0.523	712.9	0.617	175.5	0.257	259.9	0.201
-18.63	0.493	616.4	0.607	96.5	0.252	141.1	0.194
-46.09	0.248	527.3	0.591	-29.7	0.236	62.9	0.182
-81.40	0.230	505.0	0.588	-133.7	0.230	-14.8	0.181
-106.89	0.213	505.0	0.540	-200.5	0.224	-81.7	0.173
-136.31	0.202	438.1	0.515	-89.1	0.231	-163.3	0.168
-184.37	0.185	393.6	0.487	-29.7	0.238	-111.4	0.170
-269.68	0.164	289.6	0.413	82.2	0.245	37.2	0.186
-269.68	0.164	193.1	0.361	163.3	0.266	111.4	0.197
-163.77	0.182	200.5	0.330	267.3	0.272	237.6	0.215
-121.60	0.193	170.8	0.264	378.7	0.279	311.9	0.223
-72.57	0.218	81.7	0.244	423.2	0.323	408.4	0.242
-24.52	0.256	18.1	0.214	527.2	0.342	505.0	0.261
-12.75	0.310	-51.9	0.190	653.0	0.359	623.8	0.287
1.96	0.402	-89.1	0.171	757.4	0.391	716.0	0.314
67.67	0.547	-133.6	0.159	1061.8	0.446	891.1	0.330
121.60	0.572	-133.6	0.166	1247.4	0.453	1017.3	0.341
187.31	0.581	-51.9	0.170	1069.2	0.437	1203.0	0.359
248.11	0.586	-37.1	0.174	779.6	0.432	1425.7	0.394
330.48	0.597	14.9	0.199	607.0	0.401	1277.2	0.373
438.36	0.606	52.0	0.209	467.8	0.344	1091.6	0.354
548.19	0.614	118.8	0.236	386.1	0.339	913.4	0.344
659.99	0.621	178.2	0.263	215.3	0.285	705.6	0.322

		200.5	0.338	-14.9	0.268	557.0	0.279
		289.6	0.377	-245.1	0.250	393.6	0.250
		334.2	0.405	-52.0	0.257	200.5	0.232
		401.0	0.503	163.3	0.277	52.0	0.218
		467.8	0.530	334.1	0.296	-66.8	0.210
		549.5	0.547	549.4	0.375	-96.5	0.205
		683.3	0.607	742.5	0.431	-44.5	0.210
		861.4	0.627	1054.4	0.462	59.4	0.224
		1099.0	0.632	1588.0	0.506	215.4	0.242
		1410.9	0.649	2086.5	0.547	423.3	0.269
		1752.5	0.660	2569.2	0.603	660.9	0.319
		1448.0	0.653	2791.9	0.611	868.8	0.349
		1039.6	0.640	3096.4	0.630	1210.4	0.383
		675.8	0.622	3304.3	0.637	1648.5	0.437
		564.4	0.603	3593.9	0.668	2153.5	0.500
		453.0	0.590	3876.0	0.675	2651.0	0.538
		378.7	0.514	4069.1	0.693	3163.3	0.561
		259.9	0.454	4255.4	0.704	3876.2	0.588
		200.5	0.371	4284.4	0.823	4388.6	0.609
		148.5	0.347			5175.7	0.641
		122.1	0.264			5680.6	0.742
		81.7	0.252				
		59.4	0.233				
		7.5	0.200				
		-96.5	0.173				
		-37.1	0.172				
		-7.4	0.174				
		7.5	0.182				
		44.6	0.207				
		81.7	0.236				
		148.5	0.258				
		215.4	0.350				

		259.9	0.375				
		289.6	0.403				
		423.3	0.519				
		549.5	0.547				
		601.5	0.605				
		720.3	0.616				
		1017.3	0.632				
		1210.4	0.640				
		1440.6	0.651				
		1641.1	0.658				
		1849.0	0.660				
		2131.2	0.671				
		2443.0	0.682				
		2717.8	0.687				
		2940.6	0.692				
		3148.5	0.700				
		3452.9	0.706				
		3868.8	0.722				
		4053.3	0.724				
		4336.6	0.826				

Table B.2 Experimental data for Figure 3.8 (Toray TGP-H-060) (P_c: capillary pressure (Pa); S: saturation)

10 wt% wetproof		20 wt% wetproof		30 wt% wetproof	
Pc	S	Pc	S	Pc	S
1277.1	0.440	1462.1	0.385	2024.6	0.425
1098.9	0.422	1177.2	0.348	1717.1	0.407
797.3	0.406	952.3	0.273	1529.7	0.401
594.0	0.364	665.2	0.220	1222.3	0.395
460.3	0.335	474.9	0.199	1019.8	0.364
400.9	0.315	284.9	0.194	817.3	0.299
326.7	0.274	82.5	0.180	659.9	0.258
175.5	0.257	-112.5	0.175	404.9	0.231
96.5	0.252	-329.9	0.162	105.0	0.208
-29.7	0.236	-134.9	0.172	-89.9	0.186
-133.7	0.230	71.9	0.187	-269.9	0.163
-200.5	0.224	352.4	0.199	-104.9	0.174
-89.1	0.231	667.3	0.249	-37.5	0.185
-29.7	0.238	962.9	0.292	72.5	0.206
82.2	0.245	1177.2	0.318	262.5	0.229
163.3	0.266	1462.1	0.361	470.7	0.251
267.3	0.272	1169.7	0.311	669.0	0.284
378.7	0.279	989.8	0.300	997.3	0.373
423.2	0.323	674.8	0.233	1214.8	0.386
527.2	0.342	487.4	0.221	1499.7	0.399
653.0	0.359	187.5	0.209	1199.7	0.388
757.4	0.391	15.0	0.197	1049.8	0.377
1061.8	0.446	-276.9	0.187	839.8	0.339
1247.4	0.453	15.0	0.206	742.4	0.318
1069.2	0.437	292.4	0.218	638.1	0.256
779.6	0.432	674.8	0.238	442.4	0.241
607.0	0.401	967.3	0.290	240.0	0.218
467.8	0.344	1462.1	0.382	37.5	0.197
386.1	0.339	1964.5	0.418	-269.9	0.160
215.3	0.285	2462.9	0.470	-37.5	0.174
-14.9	0.268	2991.8	0.497	180.0	0.205
-245.1	0.250	3492.0	0.525	487.4	0.227
-52.0	0.257	4019.0	0.550	989.8	0.367

163.3	0.277	4101.5	0.657	1484.7	0.398
334.1	0.296			1987.1	0.429
549.4	0.375			3049.1	0.451
742.5	0.431			3599.2	0.465
1054.4	0.462			4056.6	0.479
1588.0	0.506			4354.0	0.485
2086.5	0.547			4357.2	0.566
2569.2	0.603				
2791.9	0.611				
3096.4	0.630				
3304.3	0.637				
3593.9	0.668				
3876.0	0.675				
4069.1	0.693				
4255.4	0.704				
4284.4	0.823				

Table B.3 Experimental data for Figure 3.9 (Toray TGP-H-090, 20wt% wetproof) (P_c: capillary pressure (Pa); S: saturation)

Thickness 275 μm		Thickness 225 μm		Thickness 200 μm	
Pc	S	Pc	S	Pc	S
1292.1	0.433	1373.8	0.348	1404.6	0.402
1262.1	0.433	1180.7	0.324	1173.8	0.360
1121.3	0.428	1002.9	0.312	1080.7	0.353
1009.9	0.426	906.0	0.300	956.0	0.330
868.8	0.417	698.0	0.284	708.0	0.304
772.3	0.401	505.0	0.239	505.0	0.269
698.0	0.392	393.6	0.221	393.6	0.241
549.5	0.371	259.9	0.201	259.9	0.211
460.4	0.354	141.1	0.194	141.1	0.204
371.3	0.327	62.9	0.182	52.9	0.192
311.9	0.290	-14.8	0.181	-54.8	0.171
208.0	0.258	-81.7	0.173	-153.3	0.168
170.8	0.253	-163.3	0.168	57.2	0.206
111.4	0.220	-111.4	0.170	237.6	0.235
37.2	0.214	37.2	0.186	418.4	0.266
-37.1	0.209	111.4	0.197	623.8	0.297
-81.7	0.204	237.6	0.215	716.0	0.304
-59.4	0.209	311.9	0.223	917.3	0.361
7.5	0.220	408.4	0.242	1203.0	0.439
118.8	0.230	505.0	0.261	1525.7	0.484
289.6	0.255	623.8	0.287	1267.8	0.423
401.0	0.304	716.0	0.314	1091.6	0.384
527.3	0.370	891.1	0.330	901.7	0.354
646.1	0.398	1017.3	0.341	705.6	0.312
742.6	0.414	1203.0	0.359	457.0	0.289
809.4	0.431	1425.7	0.394	293.6	0.256
957.9	0.447	1277.2	0.373	100.5	0.232
1180.7	0.472	1091.6	0.354	2.1	0.198
1336.7	0.483	913.4	0.344	-166.8	0.190
1537.2	0.506	705.6	0.322	-196.5	0.185
1373.8	0.505	557.0	0.279	-144.5	0.200
1225.3	0.492	393.6	0.250	59.4	0.234
995.1	0.478	200.5	0.232	265.4	0.252

794.6	0.459	52.0	0.218	463.3	0.289
586.7	0.425	-66.8	0.210	660.9	0.309
408.4	0.370	-96.5	0.205	868.8	0.349
178.2	0.305	-44.5	0.210	1110.4	0.393
118.8	0.300	59.4	0.224	1648.5	0.467
-37.1	0.256	215.4	0.242	2103.5	0.520
-45.1	0.250	423.3	0.269	2751.0	0.548
59.4	0.261	660.9	0.319	3263.3	0.561
252.5	0.283	868.8	0.349	3776.2	0.578
401.0	0.337	1210.4	0.383	4288.6	0.589
646.1	0.426	1648.5	0.437	5175.7	0.603
839.1	0.464	2153.5	0.500	5480.6	0.724
1165.9	0.497	2651.0	0.538		
1455.5	0.519	3163.3	0.561		
1871.3	0.552	3876.2	0.588		
2331.7	0.590	4388.6	0.609		
2866.4	0.640	5175.7	0.641		
3378.7	0.662	5680.6	0.742		
3883.7	0.678				
4292.1	0.691				
4559.4	0.700				
4871.3	0.716				
5160.9	0.738				
5584.2	0.744				
5777.2	0.805				

Table B.4 Experimental data for Figure 3.10 (Toray TGP-H-090, 20wt% wetproof) (P_c: capillary pressure (Pa); S: saturation)

Thickness 275 μm		Thickness 225 μm		Thickness 200 μm	
Pc	S	Pc	S	Pc	S
1297.2	0.287	1258.0	0.251	1277.1	0.223
1087.2	0.275	1087.2	0.241	1098.9	0.215
794.8	0.262	894.1	0.226	797.3	0.190
569.8	0.223	619.4	0.182	594.0	0.163
389.9	0.166	411.4	0.164	460.3	0.154
194.9	0.082	-26.7	0.157	400.9	0.150
0.0	0.051	-145.5	0.154	326.7	0.143
-202.5	0.025	-223.7	0.151	96.5	0.139
-67.5	0.046	-49.0	0.154	-29.7	0.136
157.4	0.083	25.3	0.156	-133.7	0.135
359.9	0.159	121.8	0.158	-200.5	0.139
577.3	0.227	337.2	0.170	-29.7	0.142
772.3	0.272	604.5	0.187	163.3	0.154
1094.0	0.285	730.7	0.219	378.7	0.164
1297.2	0.298	916.4	0.243	527.2	0.174
817.3	0.285	1139.1	0.256	757.4	0.202
622.3	0.241	990.6	0.253	1061.8	0.223
419.9	0.179	805.0	0.241	1247.4	0.229
172.9	0.098	626.8	0.209	1069.2	0.222
112.4	0.064	419.0	0.184	779.6	0.206
-195.0	0.029	270.4	0.170	607.0	0.189
75.0	0.058	107.0	0.160	467.8	0.165
374.9	0.139	-86.1	0.151	386.1	0.156
591.7	0.223	-234.6	0.148	215.3	0.148
794.8	0.268	-383.1	0.147	-14.9	0.139
1102.2	0.300	-227.2	0.151	-245.1	0.131
1604.6	0.318	-71.2	0.154	-52.0	0.141
2114.5	0.332	136.7	0.168	163.3	0.150
2631.8	0.350	374.3	0.191	334.1	0.160
3137.8	0.361	582.2	0.225	549.4	0.188
3621.6	0.379	923.8	0.247	742.5	0.208
4183.9	0.401	1361.9	0.272	1054.4	0.226
4171.8	0.470	1866.9	0.284	1588.0	0.235

		2364.4	0.299	2086.5	0.242
		2876.7	0.311	2569.2	0.252
		3589.6	0.342	3096.4	0.262
		4102.0	0.356	3593.9	0.271
		4889.1	0.388	3876.0	0.274
		4899.7	0.515	4069.1	0.281
				4255.4	0.284
				4684.4	0.298
				5001.1	0.312
				5023.3	0.677

Appendix C

Experimental Data of Neutron Imaging

Table C.1 Liquid water thickness and saturation level in through-plane direction (X: position in X-axis (Pixel), ThK_1: liquid water thickness before breakthrough (mm), ThK_2: liquid water thickness after breakthrough (mm))

	Position a		Position b	
X	ThK_1	ThK_2	ThK_1	ThK_2
45	6.40E-02	4.45E-01	6.69E-02	3.28E+00
44	3.90E-01	1.86E+00	9.21E-02	3.50E-01
43	5.99E-02	1.91E+00	1.37E-01	2.57E+00
42	8.14E-02	7.59E-01	1.00E-01	3.39E+00
41	1.13E-01	2.57E-01	5.81E-02	2.00E+00
40	7.78E-02	7.58E-01	1.12E-01	1.74E+00
39	2.43E-01	7.53E-02	9.82E-02	8.61E-01
38	1.96E-01	9.27E-02	2.44E-01	1.16E+00
37	1.01E-01	1.00E+00	1.26E-01	1.00E+00
36	4.55E-01	1.60E+00	4.70E-01	1.60E+00
35	2.04E-01	1.77E-01	7.08E-02	2.91E-01
34	3.20E-02	2.36E-01	7.90E-02	8.19E-01
33	1.82E-01	8.61E-01	1.38E-01	4.33E-01
32	5.97E-02	4.54E-01	9.35E-01	8.74E-01
31	2.39E-01	3.84E-01	4.22E-01	4.16E-01
30	2.50E-01	3.50E-01	4.10E-01	2.61E-01
29	1.42E+00	1.01E+00	6.09E-01	8.85E-01
28	8.42E-01	1.05E+00	5.00E-01	8.13E-02
27	1.05E+00	2.78E-01	4.43E-01	3.76E-01
26	2.30E-01	5.22E-01	1.87E-01	5.56E-01
25	5.96E-01	1.39E+00	1.38E-01	-1.59E-01
24	7.78E-02	1.00E+00	5.70E-01	2.56E-01
23	2.19E-02	1.19E+00	5.28E-01	-3.14E-01
22	1.76E-03	1.13E+00	2.20E+00	1.60E+00
21	1.14E+00	4.65E-01	1.26E+00	1.90E+00
20	1.87E-01	1.37E+00	8.26E-01	4.24E-01
19	1.08E+00	9.18E-01	1.76E-01	-8.48E-01
18	1.06E+00	3.21E-01	9.45E-01	6.10E-01
17	1.87E+00	9.24E-01	6.89E-01	3.00E-01

16	2.49E+00	2.02E+00	1.83E+00	1.17E+00
15	2.53E+00	2.26E+00	2.68E+00	1.27E+00
14	2.83E+00	2.51E+00	2.91E+00	3.02E+00
13	3.51E+00	3.25E+00	3.92E+00	3.53E+00
12	4.12E+00	3.96E+00	4.47E+00	4.26E+00
11	4.30E+00	3.76E+00	5.17E+00	5.28E+00
10	4.01E+00	4.00E+00	5.02E+00	5.18E+00
9	3.41E+00	4.36E+00	5.72E+00	6.01E+00
8	3.97E+00	3.74E+00	5.56E+00	5.75E+00
7	3.90E+00	4.01E+00	5.87E+00	5.68E+00
6	3.77E+00	4.13E+00	5.58E+00	5.84E+00
5	4.42E+00	3.49E+00	6.30E+00	6.08E+00
4	4.24E+00	4.08E+00	6.20E+00	5.46E+00
3	4.32E+00	4.11E+00	5.63E+00	5.12E+00
2	4.53E+00	4.05E+00	5.98E+00	6.54E+00
1	4.29E+00	4.36E+00	5.89E+00	5.97E+00

Table C.2 Liquid water thickness and saturation level in through-plane direction before breakthrough (Y: position in Y-axis (Pixel), ThK: liquid water thickness (mm), S: liquid water saturation level)

	bottom		top	
Y	ThK	S	ThK	S
1	2.59E+00	0.431	7.68E-02	0.013
2	1.97E+00	0.328	2.29E-01	0.038
3	2.36E+00	0.393	3.94E-01	0.066
4	2.17E+00	0.362	1.77E-01	0.030
5	2.67E+00	0.445	5.15E-01	0.086
6	1.96E+00	0.326	3.86E-01	0.064
7	1.75E+00	0.291	9.39E-02	0.016
8	1.50E+00	0.251	9.36E-01	0.156
9	2.00E+00	0.333	1.38E-01	0.023
10	2.43E+00	0.404	2.00E-01	0.033
11	1.62E+00	0.271	8.06E-02	0.013
12	2.73E+00	0.455	4.25E-01	0.071
13	2.15E+00	0.358	7.14E-01	0.119
14	2.71E+00	0.452	9.29E-02	0.015
15	2.06E+00	0.344	6.66E-01	0.111
16	2.47E+00	0.411	7.88E-01	0.131
17	1.37E+00	0.228	5.16E-01	0.086
18	1.43E+00	0.238	2.15E-01	0.036
19	1.40E+00	0.234	1.30E-01	0.022
20	1.36E+00	0.227	4.23E-01	0.071
21	1.34E+00	0.223	5.58E-01	0.093
22	1.46E+00	0.243	4.48E-01	0.075
23	1.12E+00	0.187	2.14E-01	0.036
24	1.21E+00	0.202	5.79E-02	0.010
25	9.36E-01	0.156	1.81E-01	0.030
26	1.48E+00	0.246	1.23E-01	0.020
27	1.30E+00	0.217	4.99E-01	0.083
28	1.39E+00	0.232	1.10E-01	0.018
29	2.21E+00	0.368	5.18E-03	0.001
30	2.04E+00	0.341	1.16E-01	0.019
31	2.94E+00	0.490	1.24E-01	0.021
32	2.12E+00	0.353	4.42E-01	0.074

33	2.51E+00	0.418	3.48E-01	0.058
34	2.36E+00	0.393	2.16E-01	0.036
35	2.91E+00	0.485	1.17E-01	0.020
36	2.62E+00	0.437	4.60E-01	0.077
37	2.36E+00	0.393	7.07E-01	0.118
38	1.82E+00	0.303	2.28E-01	0.038
39	2.48E+00	0.413	2.91E-01	0.049
40	2.63E+00	0.439	2.54E-01	0.042
41	2.81E+00	0.468	1.29E-01	0.021
42	2.29E+00	0.382	4.61E-01	0.077
43	2.42E+00	0.403	3.11E-01	0.052
44	1.58E+00	0.263	4.32E-01	0.072
45	2.25E+00	0.375	7.93E-01	0.132
46	2.47E+00	0.412	6.01E-01	0.100
47	2.34E+00	0.389	6.19E-02	0.010
48	2.87E+00	0.478	2.32E-01	0.039
49	1.78E+00	0.296	3.56E-02	0.006
50	1.80E+00	0.300	1.47E-01	0.024
51	2.14E+00	0.357	3.84E-01	0.064
52	1.64E+00	0.274	7.54E-02	0.013
53	1.45E+00	0.241	5.52E-01	0.092
54	1.26E+00	0.210	2.22E-02	0.004
55	1.15E+00	0.191	9.78E-03	0.002
56	7.93E-01	0.132	9.31E-02	0.016
57	1.08E+00	0.181	9.78E-02	0.016
58	1.06E+00	0.177	2.12E-01	0.035
59	8.82E-01	0.147	4.01E-01	0.067
60	2.74E-01	0.046	1.04E-01	0.017
61	9.98E-01	0.166	2.07E-01	0.035
62	7.22E-01	0.120	1.55E-01	0.026
63	9.57E-01	0.160	1.36E-01	0.023
64	5.45E-01	0.091	2.62E-01	0.044
65	5.61E-01	0.093	4.95E-02	0.008
66	1.08E+00	0.180	1.59E-01	0.027
67	1.20E+00	0.200	3.99E-01	0.067
68	2.04E+00	0.340	1.28E-01	0.021
69	1.29E+00	0.215	2.54E-01	0.042

70	1.89E+00	0.315	1.31E-01	0.022
71	2.34E+00	0.391	4.68E-01	0.078
72	2.15E+00	0.359	2.83E-01	0.047
73	1.74E+00	0.291	4.03E-01	0.067
74	1.59E+00	0.265	2.28E-02	0.004
75	2.15E+00	0.359	3.85E-01	0.064
76	2.09E+00	0.348	1.28E-01	0.021
77	1.23E+00	0.206	7.25E-01	0.121
78	7.29E-01	0.122	7.80E-02	0.013
79	1.35E+00	0.224	1.86E-01	0.031
80	1.50E+00	0.250	2.53E-01	0.042
81	1.21E+00	0.201	4.87E-01	0.081
82	1.01E+00	0.168	4.48E-01	0.075
83	1.71E+00	0.285	3.39E-01	0.057
84	2.03E+00	0.339	1.38E-01	0.023
85	2.27E+00	0.378	1.21E-01	0.020
86	1.82E+00	0.303	4.01E-02	0.007
87	1.47E+00	0.244	1.30E-01	0.022
88	9.10E-01	0.152	2.82E-02	0.005
89	9.54E-01	0.159	2.28E-01	0.038
90	1.11E+00	0.185	1.12E-01	0.019
91	1.42E+00	0.236	5.00E-01	0.083
92	1.00E+00	0.167	3.19E-01	0.053
93	1.40E+00	0.233	3.41E-01	0.057
94	1.32E+00	0.221	8.26E-02	0.014
95	4.75E-01	0.079	3.68E-03	0.001
96	1.11E+00	0.185	1.88E-01	0.031
97	8.87E-01	0.148	3.91E-01	0.065
98	1.32E+00	0.219	3.54E-01	0.059
99	1.11E+00	0.186	3.44E-01	0.057
100	1.65E+00	0.275	3.70E-01	0.062
101	2.12E+00	0.354	1.21E-01	0.020
102	1.57E+00	0.262	6.55E-01	0.109
103	2.02E+00	0.337	1.43E-01	0.024
104	1.70E+00	0.283	2.06E-01	0.034
105	1.94E+00	0.323	1.52E-01	0.025
106	2.33E+00	0.388	4.11E-01	0.068

107	1.83E+00	0.305	3.24E-01	0.054
108	1.83E+00	0.305	3.05E-01	0.051
109	2.20E+00	0.367	2.05E-01	0.034
110	2.31E+00	0.385	5.54E-01	0.092
111	1.95E+00	0.325	1.10E-01	0.018
112	1.97E+00	0.329	3.73E-02	0.006
113	1.82E+00	0.303	2.01E-01	0.034
114	1.61E+00	0.269	3.81E-01	0.063
115	1.87E+00	0.312	7.91E-02	0.013
116	1.80E+00	0.300	5.95E-02	0.010
117	2.47E+00	0.412	2.33E-02	0.004
118	1.54E+00	0.257	4.36E-01	0.073
119	1.82E+00	0.304	6.06E-02	0.010
120	2.41E+00	0.402	1.85E-01	0.031
121	2.81E+00	0.468	1.04E-01	0.017
122	2.54E+00	0.423	1.55E-01	0.026
123	3.26E+00	0.543	3.55E-01	0.059
124	2.62E+00	0.437	2.47E-01	0.041
125	2.50E+00	0.416	1.65E-01	0.027
126	3.00E+00	0.501	2.15E-01	0.036
127	2.71E+00	0.452	6.66E-01	0.111
128	1.61E+00	0.269	5.51E-01	0.092
129	2.15E+00	0.359	8.70E-01	0.145
130	1.88E+00	0.313	1.53E-01	0.025
131	2.05E+00	0.342	7.02E-01	0.117
132	1.76E+00	0.293	2.95E-01	0.049
133	1.45E+00	0.241	3.64E-01	0.061
134	1.58E+00	0.264	3.53E-01	0.059
135	1.70E+00	0.283	2.51E-02	0.004
136	1.18E+00	0.197	2.48E-02	0.004
137	1.15E+00	0.192	2.83E-01	0.047
138	1.24E+00	0.207	1.23E-01	0.020
139	1.57E+00	0.261	1.83E-01	0.030
140	1.25E+00	0.208	5.78E-01	0.096
141	1.20E+00	0.201	6.59E-02	0.011
142	1.32E+00	0.220	2.71E-01	0.045
143	1.09E+00	0.181	1.01E-01	0.017

144	1.27E+00	0.212	8.08E-03	0.001
145	1.19E+00	0.199	2.30E-03	0.000
146	6.89E-01	0.115	1.12E-02	0.002
147	9.77E-01	0.163	4.99E-01	0.083
148	1.48E+00	0.247	7.40E-02	0.012
149	8.66E-01	0.144	4.74E-01	0.079
150	5.22E-01	0.087	3.11E-01	0.052
151	1.42E+00	0.237	3.76E-01	0.063
152	1.53E+00	0.255	4.19E-01	0.070
153	9.44E-01	0.157	7.13E-02	0.012
154	6.38E-01	0.106	1.04E-01	0.017
155	8.59E-01	0.143	3.68E-01	0.061
156	9.31E-01	0.155	1.67E-02	0.003
157	1.35E+00	0.224	2.84E-02	0.005
158	1.50E+00	0.250	3.32E-01	0.055
159	1.74E+00	0.290	1.16E-01	0.019
160	2.27E+00	0.378	2.95E-01	0.049

Table C.3 Liquid water thickness and saturation level in through-plane direction after breakthrough (Y: position in Y-axis (Pixel), ThK: liquid water thickness (mm), S: liquid water saturation level)

	bottom		top	
Y	ThK	S	ThK	S
1	2.71E+00	0.610	1.30E-01	0.029
2	2.49E+00	0.561	4.11E-01	0.093
3	2.07E+00	0.466	3.60E-01	0.081
4	2.33E+00	0.524	3.36E-01	0.076
5	2.42E+00	0.545	4.91E-01	0.111
6	2.72E+00	0.612	2.96E-01	0.067
7	2.52E+00	0.567	6.62E-02	0.015
8	2.24E+00	0.505	6.04E-01	0.136
9	2.00E+00	0.451	2.67E-02	0.006
10	2.78E+00	0.626	2.31E-01	0.052
11	2.31E+00	0.521	1.26E-02	0.003
12	3.02E+00	0.681	7.37E-01	0.166
13	2.72E+00	0.613	8.69E-01	0.196
14	3.04E+00	0.685	2.00E-01	0.045
15	2.52E+00	0.568	5.58E-01	0.126
16	2.37E+00	0.534	5.71E-01	0.129
17	2.22E+00	0.500	4.08E-01	0.092
18	1.80E+00	0.406	9.15E-02	0.021
19	1.58E+00	0.356	3.48E-01	0.078
20	1.60E+00	0.361	3.45E-01	0.078
21	2.10E+00	0.474	3.81E-01	0.086
22	1.53E+00	0.344	2.89E-01	0.065
23	1.73E+00	0.389	3.78E-01	0.085
24	1.36E+00	0.306	7.37E-03	0.002
25	1.37E+00	0.309	2.37E-01	0.053
26	1.36E+00	0.306	1.48E-01	0.033
27	1.40E+00	0.315	2.36E-01	0.053
28	1.65E+00	0.372	4.68E-01	0.105
29	1.70E+00	0.383	5.44E-01	0.122
30	2.63E+00	0.592	8.80E-02	0.020
31	2.74E+00	0.617	1.88E-01	0.042
32	2.49E+00	0.561	2.19E-01	0.049

33	2.50E+00	0.563	4.33E-01	0.097
34	2.62E+00	0.590	7.43E-02	0.017
35	2.97E+00	0.669	3.92E-02	0.009
36	3.28E+00	0.738	3.34E-01	0.075
37	2.93E+00	0.661	4.04E-01	0.091
38	2.38E+00	0.537	1.64E-01	0.037
39	2.70E+00	0.608	4.57E-01	0.103
40	2.60E+00	0.585	2.65E-01	0.060
41	3.25E+00	0.731	4.22E-01	0.095
42	3.14E+00	0.708	4.97E-02	0.011
43	2.70E+00	0.608	5.78E-01	0.130
44	2.34E+00	0.527	1.11E-01	0.025
45	2.72E+00	0.612	8.42E-01	0.190
46	2.66E+00	0.600	5.43E-01	0.122
47	2.59E+00	0.583	3.84E-01	0.087
48	2.61E+00	0.588	3.34E-01	0.075
49	2.11E+00	0.476	1.12E-01	0.025
50	2.44E+00	0.549	4.34E-01	0.098
51	2.33E+00	0.524	3.76E-01	0.085
52	2.19E+00	0.493	3.46E-01	0.078
53	2.03E+00	0.458	1.02E+00	0.231
54	1.74E+00	0.391	9.50E-01	0.214
55	1.75E+00	0.393	1.26E+00	0.284
56	1.41E+00	0.317	7.72E-01	0.174
57	1.36E+00	0.305	1.24E+00	0.279
58	1.67E+00	0.377	1.16E+00	0.262
59	1.23E+00	0.277	1.40E+00	0.316
60	1.48E+00	0.334	1.21E+00	0.274
61	1.33E+00	0.300	1.65E+00	0.371
62	1.63E+00	0.368	1.04E+00	0.235
63	1.66E+00	0.374	8.55E-01	0.193
64	1.18E+00	0.265	1.12E+00	0.252
65	1.35E+00	0.304	1.16E+00	0.261
66	1.79E+00	0.402	8.09E-01	0.182
67	1.25E+00	0.282	1.55E+00	0.350
68	2.47E+00	0.557	2.09E+00	0.470
69	2.49E+00	0.562	1.73E+00	0.391

70	2.55E+00	0.575	1.95E+00	0.440
71	2.90E+00	0.652	1.54E+00	0.346
72	2.66E+00	0.598	1.97E+00	0.443
73	2.23E+00	0.502	1.88E+00	0.423
74	2.20E+00	0.495	1.95E+00	0.440
75	2.28E+00	0.514	1.83E+00	0.413
76	2.64E+00	0.594	1.84E+00	0.413
77	1.73E+00	0.391	1.94E+00	0.436
78	9.05E-01	0.204	1.48E+00	0.334
79	1.78E+00	0.402	1.66E+00	0.374
80	1.92E+00	0.431	1.26E+00	0.284
81	1.59E+00	0.359	1.48E+00	0.334
82	2.07E+00	0.465	4.47E-01	0.101
83	2.03E+00	0.456	1.10E+00	0.247
84	2.64E+00	0.595	5.03E-01	0.113
85	2.70E+00	0.608	8.84E-01	0.199
86	2.18E+00	0.490	9.78E-01	0.220
87	1.76E+00	0.396	4.38E-01	0.099
88	2.37E+00	0.534	8.75E-02	0.020
89	9.56E-01	0.215	1.86E-01	0.042
90	1.18E+00	0.265	5.66E-03	0.001
91	1.32E+00	0.297	6.23E-01	0.140
92	1.14E+00	0.258	5.00E-01	0.113
93	9.93E-01	0.224	2.84E-01	0.064
94	1.52E+00	0.341	2.87E-02	0.006
95	8.79E-01	0.198	5.25E-01	0.118
96	1.10E+00	0.247	3.76E-01	0.085
97	1.10E+00	0.247	9.07E-02	0.020
98	1.58E+00	0.355	4.38E-02	0.010
99	1.82E+00	0.409	2.06E-01	0.046
100	1.86E+00	0.419	2.07E-01	0.047
101	2.25E+00	0.507	1.65E-01	0.037
102	2.70E+00	0.609	6.12E-01	0.138
103	2.24E+00	0.505	1.53E-01	0.035
104	2.18E+00	0.491	3.68E-01	0.083
105	2.64E+00	0.596	9.56E-02	0.022
106	3.10E+00	0.699	4.59E-01	0.103

107	2.13E+00	0.479	5.34E-01	0.120
108	2.83E+00	0.637	1.66E-01	0.037
109	2.21E+00	0.497	1.13E-01	0.025
110	3.10E+00	0.699	3.01E-01	0.068
111	2.18E+00	0.490	3.13E-02	0.007
112	2.05E+00	0.461	8.93E-02	0.020
113	2.08E+00	0.467	5.13E-01	0.116
114	2.29E+00	0.515	4.12E-01	0.093
115	2.05E+00	0.463	4.16E-01	0.094
116	2.58E+00	0.581	3.03E-01	0.068
117	2.95E+00	0.665	3.74E-02	0.008
118	2.47E+00	0.555	1.94E-01	0.044
119	1.60E+00	0.361	2.13E-02	0.005
120	2.35E+00	0.530	2.24E-01	0.051
121	2.94E+00	0.663	2.72E-01	0.061
122	2.65E+00	0.597	6.39E-01	0.144
123	3.04E+00	0.686	6.31E-01	0.142
124	3.61E+00	0.813	5.82E-01	0.131
125	3.15E+00	0.708	1.69E-01	0.038
126	2.61E+00	0.588	1.95E-01	0.044
127	2.75E+00	0.619	3.62E-01	0.082
128	2.54E+00	0.571	1.08E-01	0.024
129	3.14E+00	0.706	5.77E-01	0.130
130	2.28E+00	0.512	2.71E-01	0.061
131	2.61E+00	0.588	4.59E-01	0.103
132	1.80E+00	0.405	2.54E-01	0.057
133	1.28E+00	0.289	5.93E-01	0.134
134	1.45E+00	0.326	3.88E-01	0.087
135	2.11E+00	0.474	1.08E-01	0.024
136	2.09E+00	0.471	1.70E-01	0.038
137	1.88E+00	0.424	4.98E-01	0.112
138	1.91E+00	0.429	3.21E-01	0.072
139	1.80E+00	0.405	3.38E-02	0.008
140	1.47E+00	0.332	3.47E-01	0.078
141	1.60E+00	0.361	1.71E-02	0.004
142	1.46E+00	0.329	1.18E-01	0.026
143	1.23E+00	0.276	1.52E-01	0.034

144	1.55E+00	0.350	8.86E-02	0.020
145	1.27E+00	0.285	5.87E-02	0.013
146	1.28E+00	0.288	1.19E-01	0.027
147	1.39E+00	0.313	3.33E-01	0.075
148	1.79E+00	0.403	2.68E-02	0.006
149	1.53E+00	0.345	3.83E-01	0.086
150	1.01E+00	0.227	4.83E-01	0.109
151	1.50E+00	0.337	2.64E-01	0.060
152	1.92E+00	0.433	6.12E-01	0.138
153	1.35E+00	0.304	1.08E-01	0.024
154	1.00E+00	0.226	1.09E-01	0.025
155	1.89E+00	0.426	1.62E-01	0.036
156	1.40E+00	0.314	9.69E-02	0.022
157	1.56E+00	0.352	9.06E-02	0.020
158	1.66E+00	0.375	1.59E-01	0.036
159	2.64E+00	0.594	3.37E-01	0.076
160	2.60E+00	0.586	3.49E-01	0.078